PREPARATION AND CHARACTERIZATION OF Al-DOPED MIXED TRANSITION METAL FERRITES AND THEIR APPLICATIONS IN WASTEWATER TREATMENT

Thesis Submitted for the Award of the Degree of

DOCTOR OF PHILOSOPHY

in

Chemistry

By

Mehnaz Ayoub

Registration Number:12105384

Supervised by

Dr. Harmanjit Singh Dosanjh (13688)

Department of Chemistry

Professor

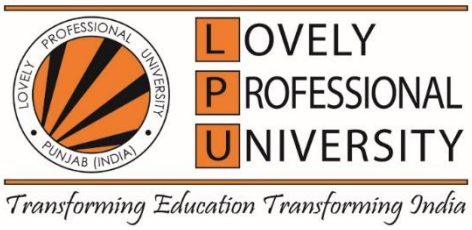

LOVELY PROFESSIONAL UNIVERSITY, PUNJAB
2025

DECLARATION

I, hereby declared that the presented work in the thesis entitled "Preparation and Characterization of Al-doped mixed transition metal ferrites and their application in wastewater treatment" in fulfilment of degree of **Doctor of Philosophy (Ph. D.)** is outcome of research work carried out by me under the supervision of Dr. Harmanjit Singh Dosanjh, working as Professor, in the School of Chemical Engineering and Physical Science of Lovely Professional University, Punjab, India. In keeping with general practice of reporting scientific observations, due acknowledgements have been made whenever work described here has been based on findings of other investigator. This work has not been submitted in part or full to any other University or Institute for the award of any degree.

(Signature of Scholar)

Name of the scholar: Mehnaz Ayoub

Registration No.: 12105384

Department/school: School of Chemical Engineering and Physical Science

Lovely Professional University, Phagwara

Punjab, India (144411)

CERTIFICATE

This is to certify that the work reported in the Ph. D. thesis entitled " Preparation and Characterization of Al-doped mixed transition metal ferrites and their application in wastewater treatment" submitted in fulfillment of the requirement for the award of degree of **Doctor of Philosophy (Ph.D.)** in the School of Chemical Engineering and Physical Science, is a research work carried out by Mehnaz Ayoub (Registration No.) 12105384, is bonafide record of his/her original work carried out under my supervision and that no part of thesis has been submitted for any other degree, diploma or equivalent course.

(Signature of Supervisor)

Name of supervisor: Dr. Harmanjit Singh Dosanjh

Designation: Professor

Department/school: Chemistry

University: Lovely Professional University

ACKNOWLEDGMENT

First and foremost, all the praises and thanks be to Almighty Allah, the most beneficent and the most merciful, for blessing me with immense strength and courage during my research work and in the compilation of this thesis.

"Learning is a continuous process of combining the familiar with the unfamiliar" encapsulates the essence of education as a perpetual journey of integrating what is already known with new and unfamiliar concepts or information. It implies that learning involves linking existing knowledge or experiences with novel ideas to deepen understanding and acquire new skills. Regarding the role of the instructor, it emphasizes the significance of guiding learners to engage with new material, encouraging them to apply their skills and tackle problems in innovative ways. I want to thank my supervisor, **Dr. Harmanjit Singh Dosanjh,** a professor at the School of Chemical Engineering and Physical Science, for all the help, advice, and support he has given me throughout my doctoral studies and research. I am thankful for his constant motivation, patience, enthusiasm, and, most of all, his unwavering support and encouragement in many ways. Furthermore, I would like to express my sincere gratitude to **Dr. Kailash Chandra Juglan**, Head of the School, and also to the members of my Research Advisory Committee, **Dr. Tanmoy** and **Dr. Suman Maji**, who monitored the progress of my work, gave insightful comments, beneficial suggestions, constant encouragement and support throughout my research work.

"Quality of life is in finding the balance between work, family, and friends" encapsulates the essence of a fulfilling life, emphasizing the importance of harmonizing various aspects such as professional endeavors, familial connections, and social relationships. I am indebted to my family, who stood behind me all the time whenever I felt physically or mentally weak. I would also like to say a heartfelt thanks to my lovely family members: my caring father, **Dr. Mohammad Ayoub Wani**; my loving mother, **Mrs**. **Mumtaza Akhtar**; and my elder brother, **Er. Aakil Ayoub**; and my loving sister, **Er. Mehvish Ayoub** for always believing in me and encouraging me to follow my dreams. Mummy and Papa, there is no way to thank you for everything you have done for me. One of the most rewarding aspects of my PhD journey has been the unwavering support of my friends, whose presence added joy and positivity to my experience, and I am deeply grateful for their continuous encouragement, assistance, and optimistic approach in helping me navigate the challenges I faced throughout my research. Additionally, I extend my heartfelt thanks to the technical staff for their unwavering

cooperation and moral support. Their dedication and assistance have played a crucial role in the success of my research work.

Finally, I sincerely thank our university for the invaluable opportunity to pursue a Ph.D. and for the comprehensive support provided throughout my academic journey. The institution's role in offering the resources, facilities, and infrastructure—ranging from laboratories and libraries to technological and academic support—was instrumental in completing my doctoral research. I deeply appreciate the university's contribution to my academic and professional growth and for fostering an environment that allowed me to engage deeply in specialized research and contribute meaningfully to the academic community

(Mehnaz Ayoub)

ABSTRACT

Water contamination has risen due to the dye industry's unrestrained growth and widespread industrialization, as well as the lack of appropriate effluent treatment techniques. Because dyes affect the natural appearance of water even in extremely low quantities, their disposal in natural water systems is a serious global problem. Discharge of industrial effluents i.e. organic (dyes) to water bodies without proper treatments, eventually pollutes water bodies, causing harmful effects on the health of animals and aquatic life. Thus, we must search for potential solutions from the perspectives of ecological safety and environmental conservation. In this regard, Al-doped mixed transition metal ferrites ($Al_xM_{0.7}Mn_{0.3}Fe_{2-x}O_4$, where M = Co, Ni, Cu and Zn, x = 0.1, 0.3, 0.5, 0.7 and 0.9) were prepared using solution combustion technique. This solution combustion method was quite more advantageous than other methods because of its low cost, easiness, more product purity, and the lack of using inorganic and organic solvents. The identity of as-synthesized ferrites was ascertained using various physiochemical methods such as FTIR, XRD, VSM, FESEM, BET, and UV-visible spectroscopy. One of the most promising approaches for wastewater cleanup is the adsorption method, which has several advantages including low secondary contamination, simple accessibility, high efficiency, broad application, and flexibility. The type and nature of the adsorbent affect adsorption efficiency. Much work has gone into creating inexpensive, extremely selective, perceptive, and efficient adsorbents. The as-synthesised ferrite materials were employed as adsorbents for the removal of dyes from their respective aqueous solutions. The adsorption isotherm studies were performed using different models, where Freundlich isotherm provided the best fit for the experimental data in Al-doped Co-Mn, Cu-Mn and Zn-Mn mixed transition metal ferrites. Whereas, the best experimental data fit for Al-doped Ni-Mn mixed transition metal ferrite was obtained from D-R isotherm. Pseudo-first-order (PFO) and pseudo-second-order (PSO) kinetic studies were employed to elucidate the kinetic nature of adsorption process. The kinetics analysis's findings indicated that PSO kinetics, with a higher coefficient of determination values, better fits the data. The thermodynamic nature of adsorption process was confirmed by calculating various thermodynamic parameters including change in enthalpy, change in Gibbs free energy, and change in entropy. These thermodynamic parameters revealed the endothermic and spontaneous nature of adsorption process. Based on these studies, Al-doped mixed transition metal ferrites are categorized as potential option for eliminating dyes from industrial effluents because of its strong adsorption capabilities and advantageous thermodynamic features. Understanding the adsorption processes and possible uses of Al-doped mixed transition metal ferrite in environmental remediation is one way the work advances the area.

List of Content

S. No	Title	Page No.
1	**Chapter 1: (INTRODUCTION)**	1-13
1.1	Introduction	2-3
1.2	Classification of ferrites	3-10
1.2.1	Classification of ferrites based on crystal structure	4-8
1.2.1.1	Spinel ferrite	4-6
1.2.1.2	Hexagonal ferrite	6-7
1.2.1.3	Garnet ferrite	7
1.2.1.4	Ortho ferrite	7-8
1.2.2	Classification of ferrites based on their magnetic properties	8-10
1.2.2.1	Soft ferrites	8-9
1.2.2.2	Hard ferrites	9-10
1.3	Applications of ferrites	10-11
1.4	Advantages of doped ferrites for adsorption	11
	References	12-13
2	**Chapter 2: (REVIEW OF LITERATURE)**	14-49
2.1	Advanced techniques for synthesizing ferrites	15-27
2.1.1	Sol-gel synthesis method	22-23
2.1.2	Coprecipitation synthesis method	23-24
2.1.3	Hydrothermal synthesis method	24-25
2.1.4	Microwave method	25-26
2.1.5	Solid-state method	26-27
2.2	Applications of spinel ferrites in the adsorption field	27-32
2.3	Need for study	32
2.4	Objectives of the research work	33
	References	34-49
3	**Chapter 3: (MATERIALS AND METHODS)**	50-64
3.1	Materials and reagents required	51
3.2	Experimental methods	51-52
3.2.1	Synthesis of Oxalyldihydrazide	51

3.2.2	Preparation of $Al_xM_{0.7}Mn_{0.3}Fe_{2-x}O_4$ (M = Co, Ni, Cu, Zn)	52
3.3	Characterization of Al-doped mixed transition metal ferrites	53-56
3.3.1	Fourier transform infrared (FTIR) analysis	53-54
3.3.2	X-ray powder diffraction (XRD) analysis	54
3.3.3	Field emission scanning electron microscope (FESEM) analysis	54
3.3.4	Vibrating sample magnetometer (VSM) analysis	55
3.3.5	Brunauer-Emmett-Teller (BET) analysis	56
3.4	Batch adsorption studies	56-57
3.4.1	Adsorption thermodynamics	57-58
3.4.2	Adsorption isotherms	58-61
3.4.2.1	Dubinin-Radushkevich (DR) isotherm	59
3.4.2.2	Langmuir adsorption	59-60
3.4.2.3	Freundlich isotherm	60
3.4.2.4	Temkin isotherm	60-61
3.4.3	Models of empirical adsorption kinetics	61-62
3.4.3.1	Pseudo-first-order (PFO) kinetics model	61
3.4.3.2	Pseudo-second-order (PSO) kinetics model	62
	References	63-64
4	**Chapter 4: (RESULTS AND DISCUSSION)**	65-124
4.0	Adsorption of dyes with Al-doped mixed transition metal ferrite	66
4.1	Al-doped Co-Mn ferrite	66-81
4.1.1	Fourier transform infrared spectroscopy (FTIR) analysis	66-67
4.1.2	Powder X-ray diffraction (XRD) analysis	67-69
4.1.3	Field emission scanning electron microscopy (FESEM) analysis	69
4.1.4	Vibrating sample magnetometer (VSM) analysis	69-70
4.1.5	Brunauer-Emmett-Teller (BET) analysis	71
4.1.6	Adsorption study of dyes with Al-doped Co-Mn ferrites	71-75
4.1.7	Study of thermodynamic parameters	75-77
4.1.8	Adsorption isotherms	77-79
4.1.9	Adsorption kinetics	80-81
4.2	Al-doped Ni-Mn ferrite	81-95
4.2.1	Fourier-transform infrared (FTIR) analysis	81-82

4.2.2	X-ray powder diffraction (XRD) analysis	82-83
4.2.3	Field emission scanning electron microscopy (FESEM) analysis	84
4.2.4	Vibrating sample magnetometer (VSM) analysis	84-85
4.2.5	Brunauer–Emmett–Teller (BET) analysis	85-86
4.2.6	Al-doped Ni-Mn mixed ferrites for adsorption of dyes	86-89
4.2.7	Thermodynamic study	90-91
4.2.8	Adsorption isotherms	92-93
4.2.9	Adsorption kinetics	94-95
4.3	Al-doped Cu-Mn ferrite	95-107
4.3.1	Fourier-transform infrared (FTIR) analysis	95-96
4.3.2	X-ray powder diffraction (XRD) analysis	96-97
4.3.3	Field emission scanning electron microscopy (FESEM) analysis	97-98
4.3.4	Vibrating sample magnetometer (VSM) analysis	98-99
4.3.5	Brunauer–Emmett–Teller (BET) analysis	99
4.3.6	Adsorption study of dyes with Al-doped Cu-Mn ferrites	99-102
4.3.7	Thermodynamic study	102-104
4.3.8	Adsorption isotherms	104-105
4.3.9	Adsorption kinetics	106-107
4.4	Al-doped Zn-Mn ferrite	107-123
4.4.1	Fourier-transform infrared (FTIR) analysis	107-108
4.4.2	X-ray powder diffraction (XRD) analysis	108-109
4.4.3	Field emission scanning electron microscopy (FESEM) analysis	110
4.4.4	Vibrating sample magnetometer (VSM) analysis	110-111
4.4.5	Brunauer–Emmett–Teller (BET) analysis	111-112
4.4.6	Adsorption study of dyes with Al-doped Zn-Mn ferrite	112-115
4.4.7	Thermodynamic study	115-117
4.4.8	Adsorption isotherms	117-118
4.4.9	Kinetics study of dye removal	119
4.5	Adsorption mechanism of dyes with Al-doped mixed transition metal ferrite	120-121
	References	122-124
5	**Chapter 5: (SUMMARY AND CONCLUSIONS)**	125-131

5.1	Adsorption of dyes using Al-doped mixed transition metal ferrites	128-130
5.2	Future scope of research	130-131
	List of Publications	132-133
	List of Conferences/Workshops	134

List of Figures

S.No	Fig. No.	Title	Page No.
1.	1.1	Classification of ferrites	4
2.	1.2	Soft and hard ferrites	10
3.	2.1	Schematic illustration for the sol-gel method	23
4.	2.2	Schematic illustration for the co-precipitation method	24
5.	2.3	Schematic illustration for the hydrothermal method	25
6.	2.4	Schematic illustration for the microwave method	26
7.	2.5	Schematic illustration for the solid-state method	27
8.	3.1	Schematic illustration for synthesis of oxalyldihydrazide	51
9.	3.2	Schematic illustration of preparation of Al-doped mixed transition metal ferrite	52
10.	3.3	Schematic illustration for dye adsorption by using of Al-doped mixed transition metal ferrite	57
11.	4.1	FTIR spectra of Al-doped Co-Mn mixed transition metal ferrites	67
12.	4.2	Powder XRD pattern of Al-doped Co-Mn mixed transition metal ferrites	68
13.	4.3	(a) SEM images (b) EDS image of Al-doped mixed transition metal ferrite ($Al_{0.5}Co_{0.7}Mn_{0.3}Fe_{1.5}O_4$)	69
14.	4.4	Hysteresis curves of $Al_xCo_{0.7}Mn_{0.3}Fe_{2-x}O_4$ ferrite at room temperature	70
15.	4.5	BET isotherm of $Al_{0.5}Co_{0.7}Mn_{0.3}Fe_{1.5}O_4$ ferrite	71
16.	4.6	UV-visible absorption spectra for 30 ppm dyes solutions	72
17.	4.7	UV-visible absorption spectra for 50 ppm dyes solutions	73
18.	4.8	UV-visible absorption spectra for 70 ppm dyes solutions	73
19.	4.9	UV-visible absorption spectra for 100 ppm dyes solutions	74
20.	4.10	The adsorption thermodynamic parameters are calculated using a plot of ln K_d vs 1/T.	76
21.	4.11	(a) Langmuir model (b) Freundlich model (c) Temkin model (d) D-R model	79
22.	4.12	Model fitting of (a) PFO and (b) PSO for CR dye adsorption onto ($Al_{0.5}Co_{0.7}Mn_{0.3}Fe_{1.5}O_4$) surface	80

23.	4.13	FTIR spectra of Al-doped Ni-Mn mixed transition metal ferrites	82
24.	4.14	X-ray powder diffraction pattern of Al-doped Ni-Mn mixed transition metal ferrites	83
25.	4.15	(a) SEM image (b) EDS of $Al_{0.5}Ni_{0.7}Mn_{0.3}Fe_{1.5}O_4$ ferrite	84
26.	4.16	Hysteresis curves of $Al_xNi_{0.7}Mn_{0.3}Fe_{2-x}O_4$ ferrites at room temperature	85
27.	4.17	BET isotherm of $Al_{0.5}Ni_{0.7}Mn_{0.3}Fe_{1.5}O_4$ ferrite	86
28.	4.18	UV-visible absorption spectra of dyes solutions at 30 ppm	87
29.	4.19	UV-visible absorption spectra of dyes solutions at 50 ppm	87
30.	4.20	UV-visible absorption spectra of dyes solutions at 70 ppm	88
31.	4.21	UV-visible absorption spectra of dyes solutions at 100 ppm	88
32.	4.22	Adsorption thermodynamic parameters derived from the linear connection between 1/T (Kelvin temperature inverse) and ln K_d	91
33.	4.23	(a) Langmuir model (b) Freundlich model (c) Temkin model (d) D-R model.	93
34.	4.24	Model fitting of (a) PFO and (b) PSO for CR dye adsorption onto ($Al_{0.5}Ni_{0.7}Mn_{0.3}Fe_{1.5}O_4$) surface	94
35.	4.25	FTIR spectra of Al-doped Cu-Mn mixed transition metal ferrites	96
36.	4.26	Powder XRD pattern of Al-doped Cu-Mn mixed transition metal ferrites	97
37.	4.27	(a) SEM image (b) EDS of $Al_{0.5}Cu_{0.7}Mn_{0.3}Fe_{1.5}O_4$ ferrite	98
38.	4.28	Hysteresis curves of $Al_xCu_{0.7}Mn_{0.3}Fe_{2-x}O_4$ ferrite at room temperature	98
39.	4.29	BET isotherm of $Al_{0.5}Cu_{0.7}Mn_{0.3}Fe_{1.5}O_4$ ferrite	99
40.	4.30	Spectra of UV-visible absorption of dyes solutions at 30 ppm	100
41.	4.31	Spectra of UV-visible absorption of dyes solutions at 50 ppm	100
42.	4.32	Spectra of UV-visible absorption of dyes solutions at 70 ppm	101
43.	4.33	Spectra of UV-visible absorption of dyes solutions at 100 ppm	101
44.	4.34	Adsorption thermodynamic parameters obtained from the linear connection between 1/T (inverse of Kelvin temperature) and ln K_d	103
45.	4.35	(a) Langmuir model (b) Freundlich model (c) Temkin model (d) D-R model	105

46.	4.36	Model fitting of (a) PFO and (b) PSO for CR dye adsorption onto ($Al_{0.5}Cu_{0.7}Mn_{0.3}Fe_{1.5}O_4$) surface	106
47.	4.37	FTIR spectra of Al-doped Zn-Mn mixed transition metal ferrites	108
48.	4.38	Powder XRD pattern of Al-doped Zn-Mn mixed transition metal ferrites	109
49.	4.39	(a) SEM image (b) EDS of $Al_{0.5}Zn_{0.7}Mn_{0.3}Fe_{1.5}O_4$ ferrite	110
50.	4.40	$Al_xZn_{0.7}Mn_{0.3}Fe_{2-x}O_4$ ferrite hysteresis curves at room temperature	111
51.	4.41	BET isotherm of $Al_{0.5}Zn_{0.7}Mn_{0.3}Fe_{1.5}O_4$ ferrite	112
52.	4.42	Spectra of UV-visible absorption of dyes solutions at 30 ppm	113
53.	4.43	Spectra of UV-visible absorption of dyes solutions at 50 ppm	113
54.	4.44	Spectra of UV-visible absorption of dyes solutions at 70 ppm	114
55.	4.45	Spectra of UV-visible absorption of dyes solutions at 100 ppm	114
56.	4.46	Plotting ln K_d vs 1/T determines the adsorption thermodynamic parameters	116
57.	4.47	(a) Langmuir model (b) Freundlich model (c) Temkin model (d) D-R model	118
58.	4.48	Model fitting for the adsorption of CR dye onto ($Al_{0.5}Zn_{0.7}Mn_{0.3}Fe_{1.5}O_4$) in pseudo-first order and pseudo-second order analysis	119
59.	4.49	Adsorption mechanism of different dyes on the surface of Al-doped mixed transition metal ferrites	121

List of Tables

S.No.	Table No.	Title	Page No.
1.	2.1	Different methods for synthesizing ferrites having different temperature and size	15-22
2.	2.2	Dye removal efficiency (%) for different ferrite materials.	28-32
3.	4.1	Crystallite size and strain of Al-doped Co-Mn ferrite	69
4.	4.2	Saturation magnetization (M_s), anisotropy constant (K), remanence (M_r), magnetic moment (μ_B), and coercivity (H_c) of $Al_xCo_{0.7}Mn_{0.3}Fe_{2-x}O_4$ ferrite annealed at 650°C for 5 hours	70
5.	4.3	Percentage removal of various dye concentrations using Al-doped Co-Mn ferrites	74-75
6.	4.4	The dye adsorption thermodynamic parameters for Al-doped Co-Mn mixed transition metal ferrite ($Al_{0.5}Co_{0.7}Mn_{0.3}Fe_{1.5}O_4$)	77
7.	4.5	Graphical and general equations illustration of adsorption isotherms	78
8.	4.6	The parameters obtained from the Isotherms-Freundlich, Temkin, Langmuir, and D-R models	79
9.	4.7	Adsorption kinetic model parameters for PFO and PSO analysis	81
10.	4.8	Crystallite size and strain of Al-doped Ni-Mn ferrite	83
11.	4.9	Saturation magnetization (M_s), anisotropy constant (K), remanence (M_r), magnetic moment ($_B$), and coercivity (H_c) of $Al_xNi_{0.7}Mn_{0.3}Fe_{2-x}O_4$ ferrite at room temperature	85
12.	4.10	Percentage removal of various dye concentrations using Al-doped Ni-Mn ferrites	89
13.	4.11	The dye adsorption thermodynamic parameters for Al-doped Ni-Mn mixed transition metal ferrite ($Al_{0.5}Ni_{0.7}Mn_{0.3}Fe_{1.5}O_4$)	91
14.	4.12	Adsorption isotherm parameters for Al-doped Ni-Mn mixed transition metal ferrite	93
15.	4.13	Adsorption kinetic model parameters for PFO and PSO analysis	95
16.	4.14	Crystallite size and strain of Al-doped Cu-Mn ferrite	97

17.	4.15	Saturation magnetization (M_s), magnetic moment (μ_B), anisotropy constant (K), remanence (M_r), and coercivity (H_c) of $Al_xCu_{0.7}Mn_{0.3}Fe_{2-x}O_4$ ferrite annealed at 650°C for 5 hours	99
18.	4.16	Percentage removal of different dye concentrations using Al-doped Cu-Mn ferrites	102
19.	4.17	Thermodynamic parameters for dye adsorption on Al-doped Cu-Mn ferrite	103-104
20.	4.18	Adsorption isotherm parameters for Al-doped Cu-Mn mixed transition metal ferrite	105
21.	4.19	Kinetic parameters of PFO and PSO adsorption kinetic models	107
22.	4.20	Al-doped ($Al_xZn_{0.7}Mn_{0.3}Fe_{2-x}O_4$) ferrites crystalline size and strain	109
23.	4.21	$Al_xZn_{0.7}Mn_{0.3}Fe_{2-x}O_4$ ferrite's magnetic moment (μ_B), saturation magnetization (M_s), anisotropy constant (K), coercivity (H_c) and remanence (M_r) annealed at 650°C for 5 hours	111
24.	4.22	Percentage removal of various dye concentrations using Al-doped Zn-Mn mixed transition metal ferrites	115
25.	4.23	Thermodynamic parameters for dye adsorption on Al-doped Zn-Mn mixed transition metal ferrite ($Al_{0.5}Zn_{0.7}Mn_{0.3}Fe_{1.5}O_4$)	116-117
26.	4.24	Adsorption isotherm parameters for Al-doped Zn-Mn mixed transition metal ferrite	118
27.	4.25	Kinetic parameters of PFO and PSO adsorption kinetic models	120

List of Abbreviations

- AR — Acid red
- ARB — Acid Red B
- ARS — Alizarin Red S
- AYR — Alizarin yellow R
- BOD — Biochemical oxygen demand
- BET — Brunauer-Emmett-Teller
- CFSE — Crystal Field Stabilization Energy
- COD — Chemical oxygen demand
- CV — Crystal Violet
- CR — Congo Red
- D-R — Dubinin-Radushkevich
- DTA — Differential thermal analysis
- EDS — Energy Dispersive Spectroscopy
- EMI — Electromagnetic Interference
- FTIR — Fourier-transform infrared spectroscopy
- FESEM — Field Emission Scanning Electron Microscopy
- MV — Methyl violet
- MO — Methyl Orange
- MB — Methylene Blue
- MG — Methyl green
- MaG — Malachite green
- NBB — Naphthol blue black
- ODH — Oxalyldihydrazide
- XRD — Powder X-ray Diffraction
- PSO — Pseudo-second-order kinetics
- PFO — Pseudo-first-order kinetics
- RhB — Rhodamine B
- RF — Radio Frequency
- SMPS — Switched-mode power supplies
- TEM — Transmission electron microscopy
- TYG — Thiazole Yellow G

- TOD Total oxygen demand
- VSM Vibrating Sample Magnetometer

Chapter 1:
INTRODUCTION

1.1 Introduction

The fascinating history of magnetic oxides, known as ferrites, and their diverse applications spans centuries. The earliest records, dating back to Greek writings before 800 B.C., describe magnetite (Fe_3O_4) as a naturally occurring non-metallic material capable of attracting iron. This magnetite, known as a loadstone, became integral to early navigators' tools, aiding in the discovery of magnetic north. Its significance in scientific exploration was recognized when it became the foundational material for constructing the first compass, a crucial navigational tool (Crangle, 1977). The 17th century marked a pivotal moment in the scientific understanding of magnetism when William Gilbert authored "De Magnete," the pioneering scientific study on this phenomenon. Later, in 1819, Hans Christian Oersted noticed how a magnetic compass needle was affected by an electric current passing via a wire. This discovery laid the groundwork for further investigations into the relationship between electricity and magnetism. Throughout the early 20th century, researchers across the globe delved into the development of magnetic materials. Noteworthy contributions came from Forestier in France, Kato, Takei, and Kawai in Japan during the 1930s, and Snoek at the Philip's Research Laboratories from 1930 to 1940, all actively advancing these materials' understanding and applications. By 1945, Snoek had established foundational principles in ferrite material physics and technology. The theoretical explanation of ferrimagnetism in ferrite materials emerged in 1948 through Neel's theory [1]. In-depth explorations of ferrites were chronicled in the classic text by Smit and Wijn [2], which covered developments until the late 1950s. Furthermore, Sugimoto's scholarly study [3] offered a comprehensive examination of ferrites, from their historical significance until the end of the 20th century, detailing their past advancements, current status, and future potentialities. This rich history highlights ferrites' evolution and ongoing exploration, a testament to their enduring importance in various scientific and technological fields.

Iron oxides, namely Fe_2O_3 and Fe_2O_4, serve as the fundamental constituents forming ferrites, a class of ferromagnetic compounds available in powdered or ceramic forms [4, 5]. These compounds are created by combining iron oxides with other metallic elements like cobalt, nickel, copper, manganese, or zinc. Their inherent magnetic properties and attributes such as high electrical resistivity and chemical stability render ferrites indispensable in numerous technological applications. Among their varied uses, ferrites play a crucial role in dye adsorption research. Their exceptional porosity and expansive surface area make these materials highly suitable for adsorbing dyes from aqueous solutions. This process hinges on the capability of ferrites to attract and retain dye molecules on their surfaces through either

chemical or physical interactions. The distinctive characteristics of ferrites, such as their significant specific surface reactivity and surface area, contribute to the efficient adsorption of dye molecules. The effectiveness of adsorption process relies on various factors including the dye type, temperature, dye concentration, and the specific properties of the ferrite material, encompassing surface area, particle size, and surface chemistry. These variables collectively influence the dye removal efficiency. Overall, the distinctive properties of ferrites position them as promising materials for absorption studies aimed at dye removal, thereby advancing the development of effective and sustainable solutions for water treatment and environmental remediation. Their versatility and efficacy in addressing such challenges underscore their significance in contributing to cleaner and healthier ecosystems.

1.2 Classification of ferrites

At their core, ferrites consist primarily of iron oxide as a foundational component along with various metal oxides. These compounds are categorized into different groups based on their structural and compositional characteristics, leading to diverse classifications within ferrite materials. Classification systems for ferrites are established considering several factors, including their crystal structures, chemical compositions, and magnetic properties. Depending on these criteria, ferrites are grouped into distinct categories delineating their unique properties and applications. The various classifications often highlight specific features such as the arrangement of atoms within their crystal lattice, the types of metals combined with iron oxide, or their magnetic behaviors. For instance, one classification method may differentiate ferrites on their crystal structure, dividing them into spinel ferrites, each possessing its atomic arrangement and magnetic properties. Another classification might focus on the elements alloyed with iron oxide, leading to categories like cobalt ferrites, nickel ferrites, or manganese ferrites, each exhibiting distinct characteristics derived from the added metallic elements. The classification of ferrites is a critical framework for understanding their diverse nature, enabling researchers and engineers to identify and utilize specific types of ferrite materials tailored for variety of applications. This systematic categorization aids in exploring and harnessing the unique properties of different ferrite groups, paving the way for their utilization across a wide array of technological, industrial, and scientific domains.

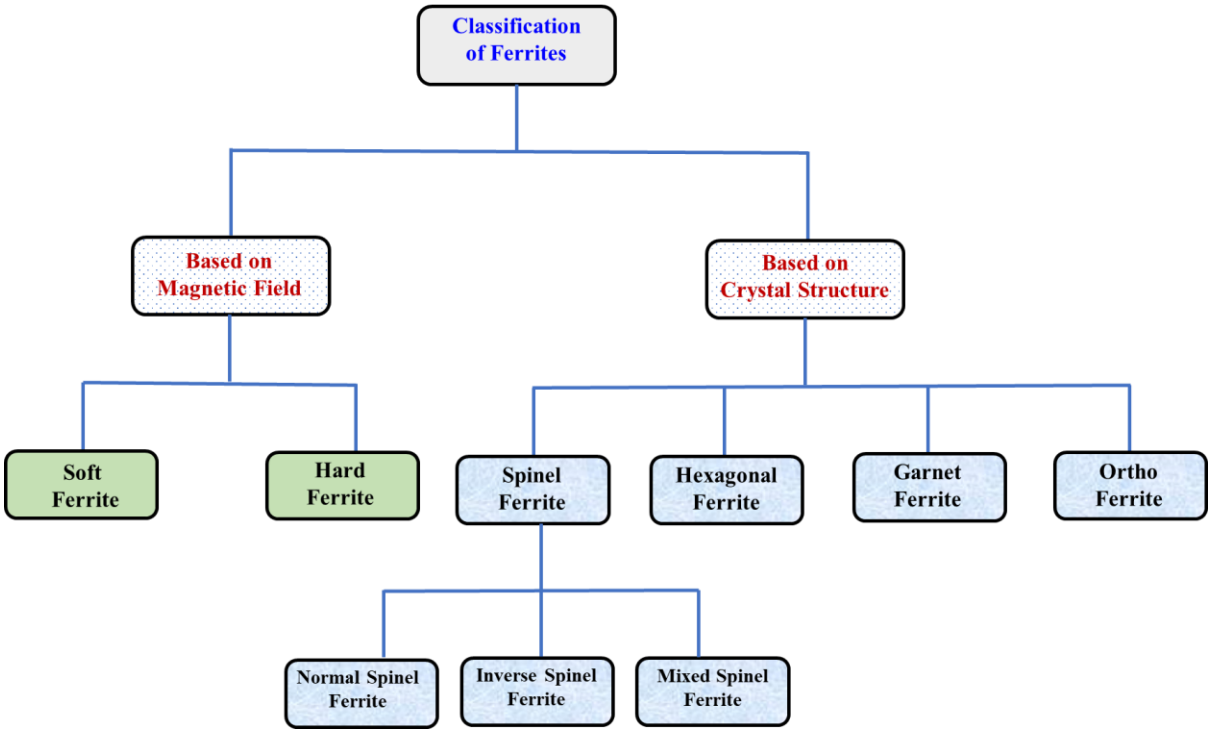

Figure 1.1: Classification of ferrites.

1.2.1 Classification of ferrites based on crystal structure

1.2.1.1 Spinel ferrites

1.2.1.2 Hexagonal ferrites

1.2.1.3 Garnet ferrites

1.2.1.4 Ortho ferrites

1.2.1.1 Spinel ferrite

Spinel ferrites exhibit a chemical formula represented as AB_2O_4, where A represents divalent metal ions occupying tetrahedral sites while B represents trivalent metal ions occupying octahedral sites within spinel crystal lattice. The arrangement of ions in a material is a critical factor in influencing its magnetic characteristics. Due to this arrangement, ferrimagnetism is produced, where the moment from ions' is aligned in antiparallel directions. Moreover, apart from oxygen anions, spinel structures can accommodate other anions like halogens, forming halospinels, or sulfur, creating thiospinels. These variations expand the spectrum of spinel structures, offering unique properties and potential applications, such as ferrospinels that incorporate different anions. The classification of spinel is often based on arrangement within

the crystal lattice, delineating specific types and arrangements with distinct structural features and properties. Based on their arrangement spinel ferrites are classified into three categories:

a) Normal spinel ferrite

b) Inverse spinel ferrite

c) Random spinel ferrite

a) Normal spinel

In the structure of normal spinel ferrite, denoted by $[AB_2O_4]$, the arrangement involves a divalent cation represented as A^{2+} that occupies the tetrahedral voids and a trivalent cation denoted as B^{3+} occupies the octahedral voids within the crystal lattice. This specific arrangement characterizes the normal spinel structure, showcasing the distribution of cations within the voids of the ferrite's crystalline framework. Within this structure, the Crystal Field Stabilization Energy (CFSE) associated with the octahedral voids is consistently greater than that of the tetrahedral voids in typical spinel ferrites. The arrangement of ions in a material is a critical factor in influencing its magnetic characteristics. The unit cell that makes up the spinel structure has 32 oxygen ions, 16 octahedral sites and 8 tetrahedral sites filled with metal cations. Normal spinel ferrites exhibit ferrimagnetism due to the antiparallel alignment of the cations' magnetic moments on different sites. Normal spinel ferrites encompass a range of compositions such as $MnCr_2O_4$, $ZnFe_2O_4$, $CdFe_2O_4$, and $MgAl_2O_4$. Each compound reflects the normal spinel structure, featuring divalent and trivalent cations occupying specific voids in the crystalline lattice. This arrangement influences their behavior in various applications, including magnetic storage, electronics, catalysis, and other technological fields, where these ferrites find extensive use due to their tailored properties and structural characteristics.

b) Inverse spinel

A kind of magnetic material known as inverse spinel ferrite has a spinel crystal structure, but its cation distribution is different from that of regular spinel ferrites. The overall formula for inverse spinel is still AB_2O_4, but the cation arrangement is different. Within an inverse spinel structure, B^{3+} ions are split between the tetrahedral and octahedral sites, whereas the A^{2+} ions occupy the octahedral sites themselves. When compared to normal spinel, this distribution results in a distinct magnetic interaction. The distinct arrangement of cations in these ferrimagnetic ferrites plays a pivotal role in determining their magnetic behavior and various physical properties. These materials find applications in diverse fields such as magnetic

recording media, sensors, microwave devices, and other technological domains due to their tailored properties derived from this specific cation distribution within their crystal structures. Notable examples of ferrimagnetic ferrites showcasing this type of structural arrangement include compounds like $NiFe_2O_4$, $CoFe_2O_4$, Fe_3O_4, and $CuFe_2O_4$. In these examples, the arrangement of ions in different sites define their unique structural and magnetic properties.

c) Random spinel

The term "random spinel" refers to a unique and intermediate structure that does not conform to the typical arrangements found in either normal or inverse spinel structures. Divalent and trivalent metal ions are distributed randomly in this intermediate structure. This random arrangement results in a deviation from the usual segregated distribution of these ions found in normal or inverse spinel structures. For instance, a random spinel composition containing varying proportions of iron might be denoted as $MnFe_2O_4$. This notation illustrates that the composition includes a mixture of manganese (Mn) and iron (Fe) ions, with the iron ions being predominant in the specific ratio specified within the square brackets. Another example of a random spinel structure is seen in $MgFe_2O_4$, where magnesium (Mg) and iron (Fe) ions are distributed randomly across the octahedral and tetrahedral sites within the crystal lattice. This arrangement differs from the strict arrangements seen in normal or inverse spinel structures, where a specific distribution pattern of metal ions is observed. The presence of a random spinel structure introduces variability within the ferrite crystal lattice, affecting its magnetic and physical properties. Understanding these unique arrangements is essential for tailoring the properties of ferrites to suit specific technological applications, as the distribution of metal ions significantly influences their behavior and functionality in various devices and systems.

1.2.1.2 Hexagonal ferrite

The class of magnetic oxides, known as hexagonal ferrites, showcase a distinct crystal structure known as the magnetoplumbite structure, which is derived from the mineral with the same name [6,7]. The general formula defining hexagonal ferrites is $MFe_{12}O_{19}$, where M denotes a divalent ion with a relatively large ionic radius. Divalent ions such as Pb^{2+}, Ba^{2+}, and Sr^{2+} are commonly used as M in hexagonal ferrites, attributing unique characteristics to these materials. The magnetoplumbite structure of hexagonal ferrite is characterized by a specific arrangement within its crystal lattice, demonstrating a hexagonal symmetry. This arrangement contributes to their exceptional magnetic and physical properties, distinguishing them from other ferrite structures. The incorporation of larger divalent ions like Pb^{2+}, Ba^{2+}, or Sr^{2+} into the crystal

structure of hexagonal ferrites significantly influences their magnetic behavior and properties. The larger ionic radii of these divalent ions cause structural distortions and alterations within the crystal lattice, affecting the magnetic interactions and leading to tailored magnetic characteristics in these materials. The choice of divalent ions as the M component in hexagonal ferrites plays a pivotal role in defining their properties, allowing for tunability of magnetic properties, and facilitating their application in various technological domains. Hexagonal ferrites find extensive use in magnetic recording media, microwave devices, and other applications where their unique magnetic properties are beneficial. Understanding the role of divalent ions and the magnetoplumbite structure is crucial in manipulating and utilizing the distinctive magnetic properties of hexagonal ferrites for diverse technological advancements.

1.2.1.3 Garnet ferrite

Garnet ferrites, characterized by the generic formula $A_3B_5O_{12}$, where A represents a trivalent ion, possess a crystal structure resembling the mineral grossularite ($Ca_3Fe_2(SiO_4)_3$). This unique arrangement distinguishes them from other ferrite structures and give rise to their specific properties. Unlike spinel ferrites, which feature a simpler crystal structure, garnet ferrites exhibit a cubic structure that is more intricate. The complexity of their crystal lattice contributes to the distinctive properties observed in garnet ferrites. One notable trait of garnet ferrites is their heightened sensitivity to stress compared to spinel ferrites. This stress sensitivity can impact their physical and magnetic properties, making them responsive to external pressures or mechanical influences. Additionally, garnet ferrites showcase superior dielectric properties compared to other gemstones. This attribute makes them valuable in various applications where specific electrical or electromagnetic characteristics are required, such as in telecommunications, electronics, and sensor technologies. Their unique combination of properties, stemming from their complex crystal structure and stress sensitivity, positions garnet ferrites as valuable materials in specialized fields. They offer distinct advantages, particularly in applications requiring precise dielectric properties or where stress responsiveness is advantageous. Understanding these distinctive features allows for tailored utilization of garnet ferrites in diverse technological and scientific domains.

1.2.1.4 Ortho ferrite

Ortho-ferrites, characterized by the generic formula ABO_3, where B represents a trivalent ion, possess a unique structural arrangement and magnetic behavior distinct from other ferrite structures. When these materials crystallize, they adopt a perovskite structure characterized by

a distorted orthorhombic unit cell, delineating their specific crystal lattice arrangement. Within the ortho-ferrite structure, two particles are anti-ferromagnetically connected, contributing to the material's magnetic properties. This anti-ferromagnetic alignment is a result of the magnetic moments in adjacent particles being oriented in opposite directions, which tends to cancel out the overall magnetic field within the material. However, ortho-ferrites also exhibit weak ferromagnetism, a phenomenon where the magnetic moments in the material exhibit a slight canting or deviation from perfect antiferromagnetic alignment. This weak ferromagnetic behavior arises due to certain structural distortions or imperfections within the crystal lattice, allowing for a small residual magnetic moment despite the predominant anti-ferromagnetic coupling. The canting in the magnetic alignment of ortho-ferrites results in a weak net magnetization and contributes to their unique magnetic properties. This weak ferromagnetism distinguishes ortho-ferrites from other ferrite structures and contributes to their potential applications in various technological fields, such as in magnetic recording, sensors, and other magnetic device applications where precise control of magnetic properties is crucial. Understanding the specific structural arrangements and the interplay between anti-ferromagnetic coupling and weak ferromagnetism is essential for harnessing the tailored magnetic properties of ortho-ferrites for specific technological applications.

1.2.2 Classification of ferrites based on their magnetic properties

Based on their magnetic properties, ferrites are divided into two primary groups as soft ferrites and hard ferrites. These distinctions are crucial in understanding their applications and functionalities within different technological contexts [8]. The two main categories are soft ferrites and hard ferrites.

1.2.2.1 Soft ferrite

1.2.2.2 Hard ferrite

1.2.2.1 Soft ferrites

These ferrites, characterized by their ease of magnetization and demagnetization, possess distinctive magnetic properties crucial for various technological applications [9]. These ferrites exhibit a small hysteresis loop, which indicates a low coercive field, and their magnetic response remains largely unaffected by changes in amplitude of the applied field. The crystal structure of soft ferrites is typically uniform, cubic, and homogeneous, comprising iron oxides and metallic divalent oxides. Notable examples of soft ferrites

include Ni-Zn ferrites ($NiZnFe_2O_4$) and Mn-Zn ferrites ($MnZnFe_2O_4$), both significant for their applications in numerous technological domains [10]. These soft ferrites find extensive use in components like multilayer EMI (Electromagnetic Interference) suppressors, inductors, RF (Radio Frequency) transformers, and switched-mode power supplies (SMPS) owing to their low losses at high frequencies. From an operational perspective, soft ferrites demonstrate magnetism when magnetic field is applied but do not retain it when the field is not applied [11]. They possess several advantages over other electromagnetic materials, including excellent permeability and stability across a wide temperature range. Additionally, their intrinsic high resistivity contributes to reduced eddy current losses over a broad frequency spectrum. Soft ferrites offer several benefits compared to other magnetic materials [12]. Their remarkable features include enhanced permeability, stability across temperature variations, and reduced losses due to eddy currents over a wide frequency range. These advantageous properties make soft ferrites indispensable in various applications requiring efficient magnetic materials that can operate effectively at high frequencies while minimizing energy losses. Understanding and leveraging these unique characteristics of soft ferrites enable their utilization in diverse technological advancements, ensuring optimal performance in a multitude of devices and systems.

1.2.2.2 Hard ferrites

These ferrites, constituted mainly of Fe combined with barium or strontium oxides, form the basis of permanent ferrite magnets, often referred to as "hard ferrites." These magnets are renowned for retaining a high level of remanence even after the process of magnetization. Unlike soft ferrites, hard ferrites exhibit a significant hysteresis loop and possess high coercive strength, which enables them to maintain their magnetic properties over prolonged periods, hence earning the term "permanent magnets." The inherent characteristics of hard ferrites allow them to sustain a strong magnetic field even surpassing the magnetic field strength of pure iron. Consequently, these ceramic magnets are frequently employed in radios and numerous other applications requiring robust and long-lasting magnetic fields. The widespread utilization of hard ferrites stems from their primary advantage: their remarkably low cost. This cost-effectiveness results from their ease of manufacturing and the ready availability of raw materials required for their production. Their robustness in retaining magnetism even under mild demagnetizing forces makes hard ferrites an ideal choice for various applications. They find extensive use as permanent magnets in automobile starting motors, synchronous and brushless motors, loudspeakers, telephone receivers, and a myriad of other devices. The distinct

properties of hard ferrites, such as their durable magnetic characteristics and cost-effectiveness, position them as one of the most extensively employed permanent magnetic materials across diverse industries. Leveraging their robustness and cost-efficient production, these ferrites play a crucial role in powering numerous devices and systems, contributing significantly to various technological advancements.

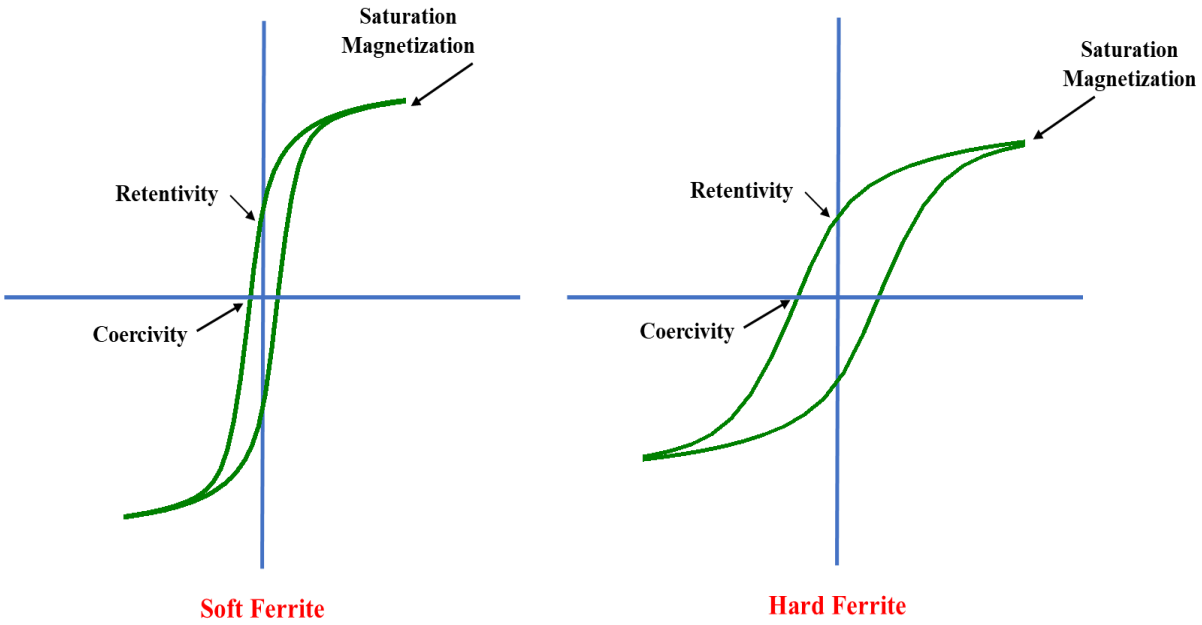

Figure 1.2: Soft and hard ferrites.

1.3 Applications of ferrites

In the recent years, there has been a growing interest in doped ferrites for their application in wastewater treatment. These speciality materials have attracted interest because of their unique capacity to adsorb different types of dyes from water. Their unique properties, such as the capacity to modify the oxidation state of pollutants, a substantial surface area, and exceptional adsorption capabilities, make them highly effective in purifying water contaminated with dyes. Among the array of nanomaterials available, ferrites stand out due to an additional magnetic trait that aids in their separation post-treatment. This magnetic property allows for easier extraction of the ferrite particles from the treated water, streamlining the purification process. This particular study utilizes ferrites for removing dyes from respective aqueous solutions. By harnessing the adsorption capabilities of ferrites, this approach holds promise in providing an efficient and environmentally friendly solution for eliminating dye-based contaminants from

wastewater. The utilization of ferrites in this capacity presents an opportunity to develop a cost-effective and selective adsorbent specifically tailored for wastewater treatment. Overall, the exploration and utilization of doped ferrites in wastewater treatment imply a significant step toward addressing environmental challenges. The potential benefits of employing ferrites lie in their exceptional adsorption capacities, magnetic separation capability, and the prospect of offering a sustainable and economical method for remediation of dye-contaminated water, contributing to the development of more efficient and environmentally conscious wastewater treatment strategies.

1.4 Advantages of doped ferrites for adsorption

Doping into ferrites involves substituting the metal ions in the lattice with other elements, either partially or entirely. The material's electrical conductivity, thermal stability, crystal structure, and magnetic ordering can all be significantly changed by this modification [13]. The doping procedure allows for fine-tuning of these basic properties that are extremely customizable for targeted applications like energy storage, environmental remediation, and target drug delivery improving their performance compared to undoped ferrites [14,15]. However, doping these ferrites with aluminum (Al) offers several advantages that make them highly desirable in various industrial and scientific applications [16]. The physical and chemical characteristics of the ferrite structure are modified by Al-doping, which also increases the ferrite's surface area and porosity, which are critical factors for effective dye adsorption. These structural changes create more active sites on the material's surface, allowing for better interaction with dye molecules in aqueous solutions [17,18]. It influences the electronic structure of ferrites, often increasing their surface charge properties and enhancing their affinity for dye molecules, particularly those with specific charges [19]. This effect is especially beneficial for adsorbing dyes with complex molecular structures or those that require strong electrostatic interactions. The magnetic properties of Al-doped ferrites also facilitate easy separation after adsorption by applying external magnetic field, making the process efficient and cost-effective. In addition, magnetic anisotropy by aluminium doping can lead to improved coercivity and optimized magnetic behavior, which is valuable for both soft and hard magnetic applications. Furthermore, aluminium-doped ferrites are chemically stable and environmentally benign, ensuring their use does not introduce additional pollutants. These materials can operate effectively under a wide range of temperature conditions, making them versatile adsorbents for various industrial and environmental applications.

References

1. Neel L., Magnetic properties of ferrites: ferrimagnetism and antiferromagnetism, Anne de Phys. 3, **1948**, 137-198.
2. Smit J. and Wijn H.P.J., Ferrites, J. Chem. Educ. 37(7), **1960**, 380.
3. Sugimoto M., The Past, Present, and Future of Ferrites, J. Amer. Ceramic. Soc. 82(2), **1999**, 269-280.
4. Bhatnagar A. and Sillanpaa M., Utilization of agro-industrial and municipal waste materials as potential adsorbents for water treatment—a review, Chem. Eng. J., 157(2-3), **2010**, 277-296.
5. Aljeboree A.M., Alshirifi A.N. and Alkaim A.F., Kinetics and equilibrium study for the adsorption of textile dyes on coconut shell activated carbon, Arab. J. Chem., 10(2), **2014,** S3381-S3393.
6. Vinnik D.A., Zhivulin V.E., Trofimov E.A., Starikov A.Y., Zherebtsov D.A., Zaitseva O.V., Gudkova S.A., Taskaev S.V., Klygach D.S., Vakhitov M.G., Sander E.E., Sherstyuk D.P. and A.V. Trukhanov A.V., extremely polysubstituted magnetic material based on magnetoplumbite with a hexagonal structure: synthesis, structure, properties, prospects, Nanomater., 9(4), **2019,** 559**.**
7. Delacotte C., Whitehead G.F.S., Pitcher M.J., Robertson C.M., Sharp P.M., Dyer M.S., Alaria J., Claridge J.B., Darling G.R., Allan G., Winter G., and Rosseinsky M.J., Structure determination and crystal chemistry of large repeat mixed-layer hexaferrite, IUCrJ, 5, **2018**, 681-698.
8. Roy D., Shivakumara C. and Kumar P.S.A., Observation of the exchange spring behavior in the hard soft-ferrite nanocomposite, J. Magn. Mater. 321(5), **2009**, L11-L14.
9. Suarez A., Victoria J., Alcarria A., Torres J., Martinez P.A., Martos J., Soret J., Garcia-Olcina R., and Muetsch S., Characterization of different cable ferrite materials to reduce the electromagnetic noise in the 2-150 kHz frequency range, Mater. (Basel) 11(2), **2018,** 174.
10. Devi E.C. and Singh S.D., Magnetism in Nanostructured Spinel Ferrites with Recent Advances in Processing, Characterization, and Applications, Advan. Nanostruct. Mater., **2022**, 317-342.

11. Lawrence H. and Vlack V., Elements of Materials Science and Engineering, 6th Ed. Addison-Wesley, **1989**, 598.

12. Snelling E.C., Soft ferrites and Applications, 2nd ed. Butterworths, **1988**, 366.

13. Sumaira A., Muhammad A.A., Nasrullah, Muhammad A.R., Abdul S., Muhammad U., Muhammad S.A., Ali J., Muhammad M.U.H. and Abid M., Synthesis and Photocatalytic Performance of Cobalt-Doped Nickel Ferrites for Dye Degradation, Int. J. Curr. Eng. Technol. 11(3), **2024**, 305-312.

14. Saad S., Amor S.B. and Slimane A.B., Preparation of Magnesium Doped Magnetic Nanoferrite and its Clay-Based composite: Application to the Removal of an Anionic Dye from Wastewater, Chem. Afr. 5, **2022**, 589-606

15. Starko I., Tatarchuk T., Naushad M. and Danyluik N., Enhanced Activity of La-Substituted Nickel–Cobalt Ferrites in Congo Red Dye Removal and Hydrogen Peroxide Decomposition, Water Air Soil Pollut. 235, **2024**, 527.

16. Muhammad Y., Atif M., Kinza F., Maddiha R., Muhammad U., Muhammad J.K., Devendra P.R. and Raja W.S., Synthesis, characterization, and photocatalytic activity of aluminum doped spinel ferrite nanoparticles for the photodegradation of Congo red. Reac. Kinet. Mech. Cat. **2024**.

17. Ayoub M. and Dosanjh H.S., Al-doped mixed transition metal ferrites synthesis and application in adsorption of dyes, Chemistry Select. 9(40), **2024**, e202403132

18. Desai H.B., Karki B., Bhatt R.P., Verma R., Kane S.N. and Tanna A.R. Aluminum-Doped Magnesium–Manganese Mixed Nano Ferrites as an Effective Photocatalyst for Methylene Blue. Nano Select. **2024**, e202300199.

19. Khapre M., Shekhawat A., Saravanan D., Pandeyc S. and Jugade R., Mesoporous Fe–Al-doped cellulose for the efficient removal of reactive dyes, Mater. Adv., 3, **2022**, 3278.

CHAPTER 2:
REVIEW OF LITERATURE

2.1 Advanced techniques for synthesizing ferrites

The synthesis of ferrites involves various techniques, each with its unique methodology, advantages, and applications. Current studies have highlighted several methods used for ferrite synthesis, including hydrothermal [1, 2], sol-gel [1, 2, 3], co-precipitation [1, 2], and solid-state methods [1]. Additionally, unconventional methods like aberrant gasoline, micro-emulsion [4, 5], thermal decomposition [1, 6], and electro-spinning techniques [1] are also utilized for this purpose. The specific characteristics of nano ferrites (MFe_2O_4, where M represents elements such as Cu, Co, Zn, Ni, and Al) are dependent on the method of synthesis and the conditions under which they are integrated. Determining the structural characteristics and obtaining properly calibrated ferrites depend on choosing a suitable synthesis technique [7]. Hence, choosing the right method becomes pivotal for assembling structures and obtaining the desired characteristics of ferrites. The synthesis of ferrites can yield variations in particle sizes at different temperatures. A comprehensive array of methods for synthesizing ferrites across different temperature ranges and achieving varied particle sizes is typically outlined in academic studies and research, often presented in a table for easy reference and comparison, as demonstrated in Table 2.1 of the respective study. These methods provide researchers and scientists insights into the diverse approaches available for synthesizing ferrites, enabling them to tailor the process based on the desired properties and applications of the resulting materials.

Table 2.1: Different methods for synthesizing ferrites having different temperatures and size.

Ferrites	**Method**	**Calcination temperature (C)**	**Size (nm)**	**Reference**
Cu, Ni, $ZnFe_2O_4$	Hydrothermal	50°C	-	[8]
$FeOFe_2O_3$	Precipitation	-	-	[9]
$ZnFe_2O_4$	Hydrochemical	100°C	100 µm	[10]
Ni-Zn Fe_2O_4	Hydrothermal	180-240◦C	70 nm	[11]
$CoFe_2O_4$	Coprecipitation	20–80°C	2-14 nm	[12]
$Cr_2Fe_2O_4$	Coprecipitation	50°C	-	[13]
$MnFe_2O_4$	Coprecipitation	95–100°C	40 mm	[14]
$Ni_XZn_{1-X}Fe_2O_4$	Conventional Solid-state reaction	1325°C	0.5 µm	[15]
$Zn_xFe_{3-x}O_4$, $Ni_xFe_{3-x}O_4$	Wet method	500°C	0.1-0.4 µm	[16]

and $Cr_xFe_{3-x}O_4$				
$NiFe_2O_4$	Coprecipitation	900°C	>50 nm	[17]
$SrFe_{12}O_{19}$	Coprecipitation	800-1100°C	12-90.7 nm	[18]
$MnFe_2O_4$	Coprecipitation	60°C	59 nm	[19]
$Fe_{1-y}Ni_yFe_2O_4$ and $Fe_{1-x}Co_xFe_2O_4$(x, y = 0, 0.05, 0.1, 0.2, 0.5)	Coprecipitation	80°C	13.3 ± 3.1 nm	[20]
$Mg_{0.5}Ni_{0.5}Fe_2O_4$	Coprecipitation	110°C	2.7 µm	[21]
$CrFe_2O_4$ and $NiFe_20_4$	Hydrothermal	70-75°C	-	[22]
$NiFe_2O_4$	Hydrothermal	150°C	14 nm	[23]
$MnFe_2O_4$	Sol-gel	80-500°C	2.0 µm	[24]
$MnFe_2O_4$	Solvothermal	260°C	50 nm	[25]
$NiFe_2O_4$	Sol-Gel	200-500°C	5-50 µm	[26]
Zn-Fe_2O_4	Solvothermal	25°C	25.75 nm	[27]
$Ni_{0.5+1.5x}Cu_{0.3}Zn_{0.2}Fe_{2-x}O_4$	Precursor	450°C	16-24 nm	[28]
$CoFe_2O_4$	Hydrothermal	278°C	10-40 nm	[29]
$Ni_{1-x}Cu_xFe_2O_4$	Sol-Gel	1000°C	-	[30]
$CoFe_2O_4$	Coprecipitation	110°C	-	[31]
$MnFe_2O_4$	Coprecipitation	109.85°C	-	[32]
$CuFe_2O_4$	Hydrothermal	200°C	24.6-51.5 nm	[33]
$Zn_{1-x}Co_xFe_2O_4$	Hydrothermal	800°C	27 nm	[34]
$NiFe_2O_4$	Sol-gel	25°C	17 nm	[35]
$ZnFe_2O_4$	Hydrothermal	20-60°C	5-20 nm	[36]
$ZnFe_2O_4$	Coprecipitation	800°C	49 nm	[37]
$ZnFe_2O_4$	Hydrothermal and citrate	550°C	103.79-108.23 nm	[38]
$MgFe_2O_4$	Coprecipitation	500°C	25–35 nm	[39]
$MnFe_2O_4$	Microwave-assisted combustion	-	>100 nm	[40]
MFe_2O_4 (M= Co, Ni, Cu, and Zn)	Sol-gel	400-1000°C	20 nm and 100 nm	[41]

$ZnFe_2O_4$	Microwave-solvothermal	110°C	0.15-0.20 µm	[42]
$CuFe_2O_4$	Hydrothermal	100-200°C	35-45nm	[43]
$ZnFe_2O_4$	Co-precipitation	300-950°C	≥10 nm	[44]
$ZnFe_2O_4$	Solvothermal	45-180°C	15.2 nm	[45]
$ZnFe_2O_4$	Hydrothermal	75°C	16-19 nm	[46]
$NiFe_2O_4$/KAOLINITE	Sol-gel auto-combustion	350-500°C	-	[47]
$MgFe_2O_4$	Co-precipitation	60-100°C	0.5 mm	[48]
$ZnFe_2O_4$	Hydrothermal	121°C	10 nm-15 nm	[49]
NG@$CoFe_2O_4$	Hydrothermal	180°C	100-150 nm	[50]
$CoFe_{1.9}Mo_{0.1}O_4$	Sol-gel	600°C	-	[51]
$NiFe_2O_4$	Co-precipitation	350°C		[52]
$MnFe_2O_4$	Hydrothermal	-	6.11nm	[53]
$ZnFe_2O_4$	Combustion method	37°C	22.13 nm	[54]
$NiFe_2O_4$	Hydrothermal	100°C	10-30 nm	[55]
$Zn_{1-x}Cu_xFe_2O_4$	Hydrothermal	170-120°C	15.57-23.49 nm	[56]
$NiFe_2O_4$	Microwave, Co-precipitation, and pyrolysis	405-763K	6 nm	[57]
$NiFe_2O_4$ Polyaniline	Co-precipitation	300-500°C	-	[58]
$NiRu_xFe_{2-x}O_4$ and $CuRu_xFe_{2-x}O_4$	Sol-gel	-	10 nm-20 nm	[59]
$CoFe_2O_4$	Sol- gel auto combustion	110°C	15-22 nm	[60]
Rice Straw-$CoFe_2O_4$	Sol-gel	550°C	42.9-86.7 nm	[61]
$NiFe_2O_4$	Hydrothermal	190 °C	40-80 nm.	[62]
$CoFe_2O_4$	Coprecipitation	900°C	15-23 nm	[63]

$CuFe_2O_4$, $CoFe_2O_4$, $MnFe_2O_4$ and $ZnFe_2O_4$	Sol – Gel	200-500ºC	484 nm	[64]
$CoFe_2O_4$	Solvothermal	198ºC	0.2 µm	[65]
$NiFe_2O_4$	Sol-gel auto combustion	40ºC	30-40 nm	[66]
$ZnFe_2O_4$	Sol-gel combustion	135ºC	52 nm	[67]
$MnFe_2O_4$	Sol-gel	-	< 50 nm	[68]
Mg_{1-x}-$Zn_xFe_2O_4$	Sol- gel auto combustion	60ºC	1-2 µm	[69]
$MnFe_2O_4$-GO	Solvothermal	35°C	25 nm	[70]
$MgFeCrO_4$	Sol-gel	90°C	17 nm	[71]
$Co_{0.30}Cu_{0.25}Zn_{0.45}Ce_x$ $Fe_{2-x}O_4$	Sol-gel auto-ignition	700°C	77.59-109.27nm.	[72]
$Co_{0.1}Al_{0.03}Fe_{0.17}O_{0.4}$	Sol-gel method	800°C	46.51-36.21nm	[73]
Ag-doped $NiFe_2O_4$	Sol-gel	550°C	-	[74]
$Cu_{1-x}Cd_xFe_2O_4$	Co-precipitation	26.85ºC	-	[75]
$Ni_{0.5}Co_{0.5}Ce_{0.2}Fe_{1.8}O_4$	Sol-gel	1000°C	30.05-70.46 nm	[76]
$MnFe_2O_4$	Co-precipitation	-	11-26 nm	[77]
$Co_xMg_{1-x}Fe_2O_4$	Sol-gel	700ºC	34 nm	[78]
$Cu_{0.5}Mg_{0.5}Fe_2O_4$–TiO_2	Co-precipitation and Sol-gel	80-150ºC	40.09 nm	[79]
$CuFe_2O_4$, $CoFe_2O_4$ and $NiFe_2O_4$	Hydrothermal	550ºC	38.1-17.1nm	[80]
$SnFe_2O_4$	Chemical precipitation	-	2.12 nm	[81]
$Co_{0.5}Cu_{0.5}Sm_xFe_{2-x}O_4$	Citrate combustion	300ºC	~75–45 nm	[82]
Ce-doped $CuFe_2O_4$	Hydrothermal	180ºC	1 µm	[83]
ZnO/$NiFe_2O_4$	Hydrothermal, Sol-gel,	135-250ºC	70 nm, 7-28 nm,	[84]

	Combustion		38 nm	
Cu–$MgFe_2O_4$	Co-precipitation	-	12-44 nm.	[85]
Fe_3O_4/Zeolite NaA	Hydrothermal	~105°C	~96.5 nm	[86]
$CoFe_2O_4$	Chemical	100°C	-	[87]
$Ca_{1-x}Cu_xFe_2O_4$ (x=0.2, 0.4, 0.6, 0.8, 1)	Co-precipitation	650ºC	32-19 nm	[88]
$TiO_2/ZnFe_2O_4$, $ZnFe_{1.98}La_{0.02}O_4$	Sol-gel	350 °C	10–70 nm	[89]
$MgFe_2O_4$	Self-combustion	400 to 800°C.	-	[90]
$NiFe_2O_4$	Co-precipitation	700°C	-	[91]
CTAB-$NiFe_2O_4$	Low-temperature combustion	650ºC	-	[92]
$Mg_{0.5}Zn_{0.5}Fe_2O_4$	Facile rapid combustion	400°C	10-60 nm	[93]
$Co_{0.5}Ni_{0.5}Fe_2O_4$, CNFO	wet-chemical route	750°C	14.3 to 16.3 nm	[94]
$CoFe_2O_4$	Co-precipitation	-	-	[95]
$MgFe_2O_4$	Co-precipitation	600°C	20nm-50nm	[96]
(P3ABA/GO/$CoFe_2O_4$)	Simple and straightforward polymerization	100°C	-	[97]
PANI/ $NiFeCo_{0.5}Zr_{0.5}O_4$	Co-precipitation	-	-	[98]
Ce-doped cobalt/nickel mixed ferrites	Microemulsion	-	44.8 nm	[99]
Chemical mediated Manganese Ferrite/Green Manganese Ferrite	Co-precipitation	-	-	[100]
$Co_xZn_{1-x}Fe_2O_4$	Environmentally friendly approach	45ºC.	5-9 nm	[101]

$Co_{0.5}Ni_{0.5}Fe_2O_4$,	Wet-chemical route	550, 650, and 750°C	14.3 to 16.3 nm	[102]
Reduced graphene oxide cobalt ferrite (RGCF)	Coprecipitation	550°C	16.5 nm	[103]
Pan−MgF−NC	-	-	20 to 40 nm	[104]
$Mg_{0.4}Zn_{(0.6-x)}Ca_xFe_2O_4$	Precursor approach		15–38 nm	[105]
$CoFe_2O_4$/OS,	Co-precipitation	-	-	[106]
NiF-NPs	Thermal heat treatment method	-	28 nm.	[107]
$CoFe_2O_4$, $ZnFe_2O_4$	Hydrothermal	180°C	25 nm and 18.5 nm	[108]
$Ni_{1-x}M_xFe_2O_4$ [Mn, Zn]	Co-precipitation	700°C	200 to 800 nm	[109]
$FeTiO_3$	Sequential hydrothermal	160°C	-	[110]
$CoFe_2O_4$ and $NiFe_2O_4$	Co-precipitation	500°C	16.07 nm and 13.84 nm	[111]
rGO-loaded spinel cobalt ferrite (RGCF)	Coprecipitation	550°C	10 nm	[112]
Zinc ferrite ($ZnFe_2O_4$) and copper ferrite ($CuFe_2O_4$)	Co-precipitation	500°C	10.82 nm and 15.16 nm	[113]
$Co_{0.5}Zn_{0.25}M_{0.25}Fe_2O_4$, M = Ba, Cu, Mn, Ni and Sr	Co-precipitation	500°C	-	[114]
$Co_{1-x}Zn_xFe_2O_4$/PANI	Hydrothermal	-	8.56 nm	[115]
Zinc Ferrite Pine Cone	Solution combustion	-	-	[116]
$CoFe_2O_4$	Sol–gel	650°C	18.75 nm	[117]

Nickel ferrite	thermal heat treatment	-	28 nm.	[118]
$ZnFe_2O_4$ and $ZnFe_2O_4$@SiO_2	Co-precipitation	600 and 800°C	-	[119]
$MnFe_2O_4$	Sol-gel	670°C	19.32 nm	[120]
$Ni_{0.5}Zn_{0.5}Fe_2O_4$	Co-precipitation	90°C	15 – 25 nm	[121]
$Ni_{0.5}Co_{0.5}La_xFe_{2-x}O_4$ (x = 0; 0.01; 0.025; 0.05)	Sol–gel auto-combustion	80°C.	1 to 6 μm	[122]
Ni-FNPs, Mn-FNPs, Co-FNPs, Cu-FNPs, and Zn-FNPs	Auto combustion, hydrothermal, hydrothermal, combustion, Sol–gel	80–85°C, 180°C, 180°C, 80°C, and 130°C	-	[123]
$Cu_xNi_{1-x}Tb_yFe_{2-y}O_4$	Co-precipitation	550°C	-	[124]
$ZnFe_2O_4$	Combustion	-	43.72 and 29.38 nm	[125]
$CaFe_2O_4$	Sol-gel	873K	24.34 nm	[126]
MFe_2O_4 (M = Cu, Ni, Zn, and Cd)	sol–gel self-combustion	90°C	19.22–29.07 nm	[127]
Ni and Mn co-doped $ZnFe_2O_4$	Co-precipitation	-	21 nm to 28 nm	[128]
$ZnFe_2O_4$-PANI	-	600°C	17.67 nm	[129]
$Ni_{0.5}Zn_{0.5-x}Cu_xFe_2O_4$	Polyol	-	~4–6 nm	[130]
$Zn_{0.5}Mg_{0.5}Fe_2O_4$	Sol-gel and solvothermal	90°C and 400°C	14.7 nm and 17.4 nm	[131]
$Zn_{0.5}Ni_{0.3}Cu_{0.2}Fe_{2-x}Gd_xO_4$	Self-ignition sol–gel	750°C	-	[132]
$CuFe_2O_4$	Sol–gel	723k	18.64 nm	[133]
MgF-Cs-Ze, NiF-Cs-Ze, MgF@NiF-Cs-Ze	Auto combustion	80°C	-	[134]

$Bi_{1-x}Bent_xFe_{1-y}Co_yO_3$ (x = 0.00 – 0.03, y = 0.00 – 0.15)	Solvothermal	-	-	[135]
Mn-Zn ($Mn_{0.3}Zn_{0.7}Fe_2O_4$)	Solution combustion	650°C	-	[136]
$CoFe_{2-x}Al_xO_4$	Sol-gel auto combustion	800°C	-	[137]
$CuFe_2O_4$	Combustion	-	26.37 and 17.65 nm	[138]
$Zn_{(1-2x)}Ag_xCr_xFe_2O_4$, (where x = 0.0 to 0.25)	Co-precipitation	80°C	7–15 nm	[139]
$MgFe_2O_4$ and $MgFe_2O_4$/bentonite	Self-combustion	180°C	27 nm	[140]
$(CoFe_2O_4)_{1-x}/(Mg_{0.9}Ni_{0.1}O)_x$	Co-precipitation	100°C	40.9 nm.	[141]

2.1.1 Sol-gel synthesis method

The bottom-up method is a notable example of the sol-gel technique, also known as wet chemical synthesis or chemical decomposition. This technique involves the utilization of metal alkoxide solutions [M $(ROH)_n$] and is widely employed for sol-gel synthesis. The process encompasses several sequential stages including condensation, hydrolysis, polymerization [142], gelation, drying, and densification [143], to create a gel at room temperature. The sol-gel synthesis beings with creating a solution of chemical compounds in which ligands encapsulate metals and metalloids, such as the nitrates of compound metals. During hydrolysis, the hydroxyl ion binds with the metal ion (M). The completion of hydrolysis depends on factors such as the water content and the presence of catalysts, where all groups might get replaced by OH or hydrolysis, where ‘M’ remains slightly hydrolyzed. The thickening reaction releases water molecules, facilitating the formation of larger metal molecules through polymerization. Once this molecule reaches macroscopic proportions and is present throughout the solution, the material is referred to as a "gel" [144]. Compared to the solid-state approach, the sol-gel process yields homogenous single-phase ceramics without requiring grinding procedures, eliminates the potential of contamination from external sources, and ensures the purity of the material. The sol-gel method's ability to produce well-defined and homogenous materials

without additional contamination makes it a preferred technique for fabricating ceramics and other materials with tailored properties for various technological applications.

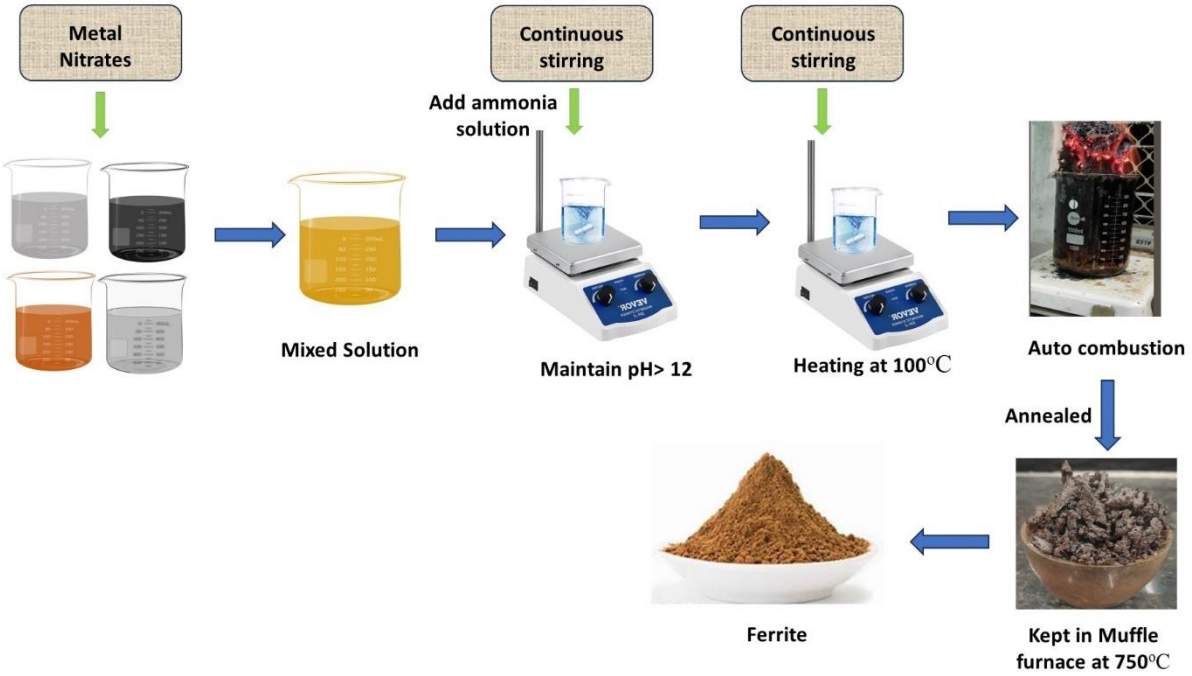

Figure 2.1: Schematic illustration for the sol-gel method.

2.1.2 Coprecipitation synthesis method

This technique is widely used for its cost-effectiveness, easiness, and efficiency in producing materials with uniform particle sizes, making it a favored method for various applications [145]. This method involves mixing reactants, usually chlorides or nitrates, into a clear aqueous solution. The pH of the solution is adjusted using a base, typically hydroxides, to induce precipitation and form a homogeneous precipitate. This precipitate essentially constitutes a mixed combination of reactants in the form of ferrite metals at the atomic scale. The control of solution pH is important for producing high-quality materials using this technique, as it plays a pivotal role in determining the specific types of nano-ferrite spinel formed during the process. Once the reaction occurs, the solid precipitate is collected and subjected to a cleaning process. The residue is then heated to a medium-to-high boiling point to dry the final product and convert it into hydroxides. The conversion of hydroxides into crystalline oxides is a critical step in this process, as it determines the ultimate composition and properties of the ferrite materials being synthesized. This controlled conversion process is essential for achieving the desired characteristics and functionalities of the nano-ferrites. Overall, the co-precipitation technique provides an efficient and streamlined method for producing ferrite materials with

tailored properties. Its simplicity, along with the ability to control parameters such as pH during the precipitation and conversion processes, makes it a highly favored approach in material synthesis, particularly for generating uniform and high-quality ferrite nanoparticles suitable for various applications.

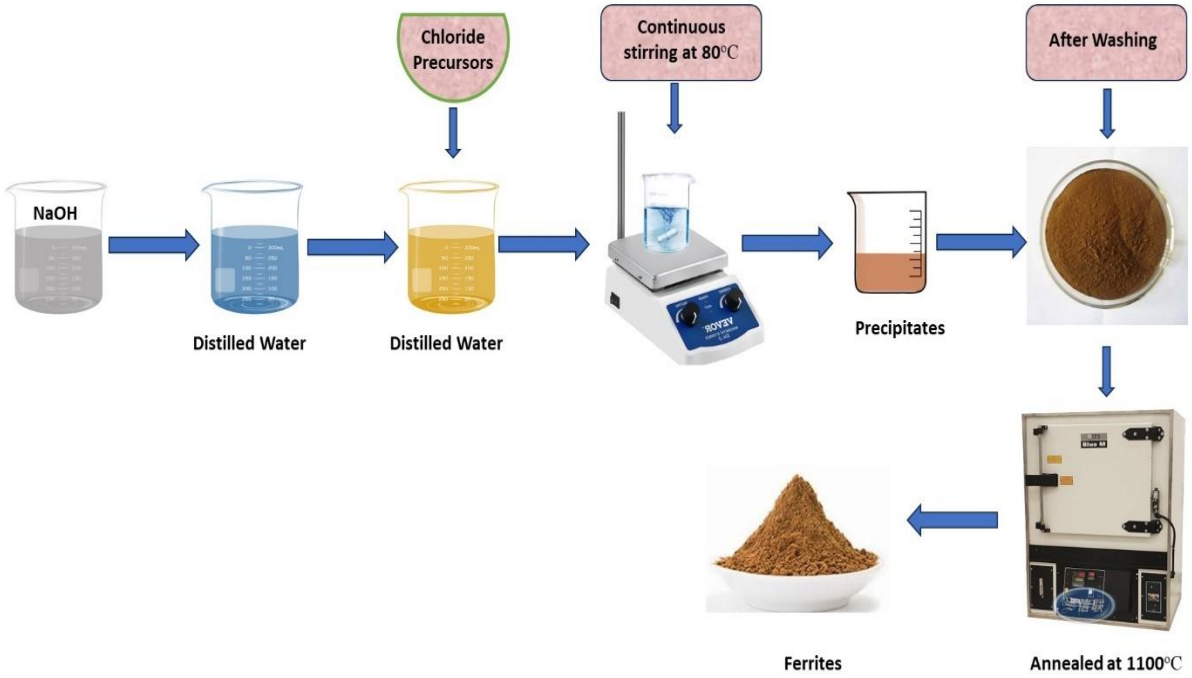

Figure 2.2: Schematic illustration for the co-precipitation method.

2.1.3 Hydrothermal synthesis method

The hydrothermal method is a promising synthesis technique for the large-scale production of materials. This method involves subjecting substances to high pressure and temperature conditions in an aqueous solvent environment, enabling the dissolution and subsequent recrystallization of materials that are typically difficult to handle or modify under normal conditions [146]. One of the key advantages of the hydrothermal method is its ability to generate materials with high purity and homogeneity that results in materials with well-defined crystal symmetry and structures. Additionally, this method can produce metastable compounds with unique properties that might not be achievable through conventional synthesis routes. Several distinct advantages are associated with the hydrothermal method. It enables rapid reactions, significantly reducing the time required for material formation. Moreover, this technique operates with relatively low energy requirements, contributing to its efficiency in large-scale production. The hydrothermal method also tends to yield materials with a narrow

particle size distribution, ensuring uniformity in the synthesized products. Another notable advantage is its capacity to facilitate the formation of crystals with low solubility or to induce polymorphic modifications, which is particularly valuable in generating materials that might be challenging to synthesize using other conventional methods. Overall, the hydrothermal method offers numerous benefits for large-scale material production. This method's ability to yield materials having unique properties, more purity, crystal symmetry, and controlled particle sizes makes it an attractive technique for synthesizing a wide range of materials, especially those that exhibit complex structures or challenging to fabricate using traditional synthetic methods.

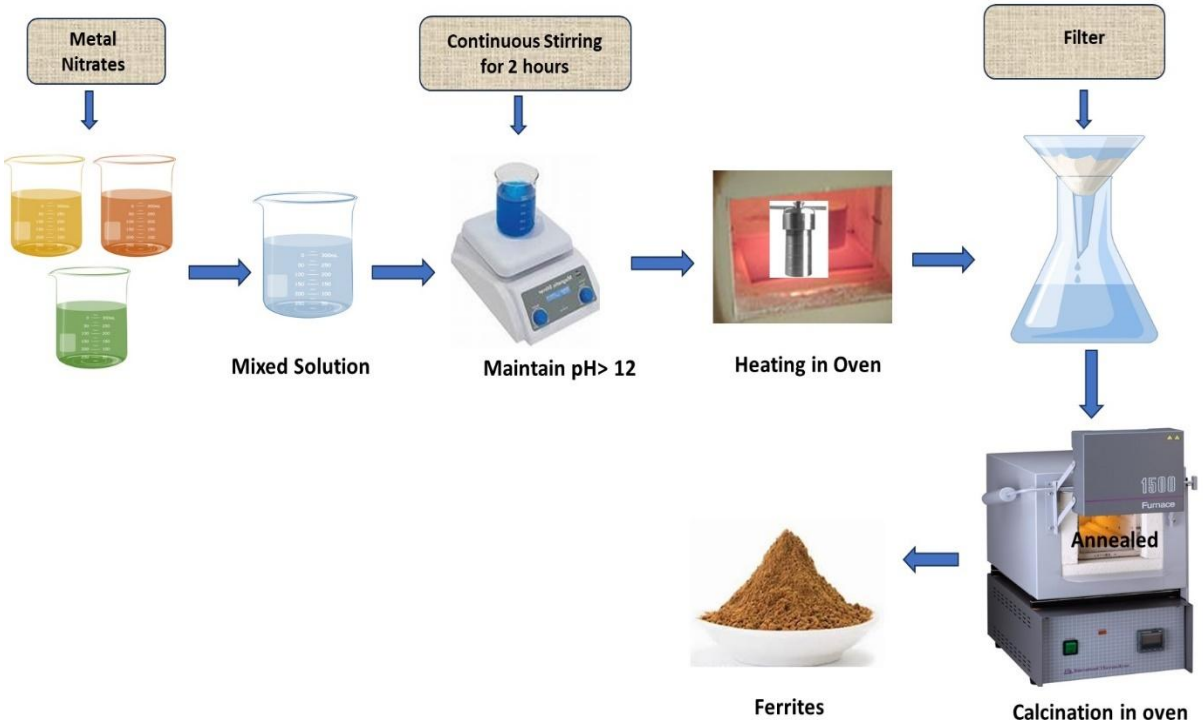

Figure 2.3: Schematic illustration for the hydrothermal method.

2.1.4 Microwave method

The prepared ferrite may be significantly affected by the heating method, whether a conventional or microwave oven, as well as the duration of the heating process. Compared to thermal heating, microwave radiation can enhance chemical processes. In reaction mixtures with polar compounds, absorbed microwave radiations result in heating the interior of the mixture. Heat is then transported from the interior to the limits (the vessel wall). This process, known as conductive-convective heat transfer is the continuous cycle in which heat is

transferred from the boundaries back into the interior. Typically, these acts quicken the reactions and enhance the overall outcome.

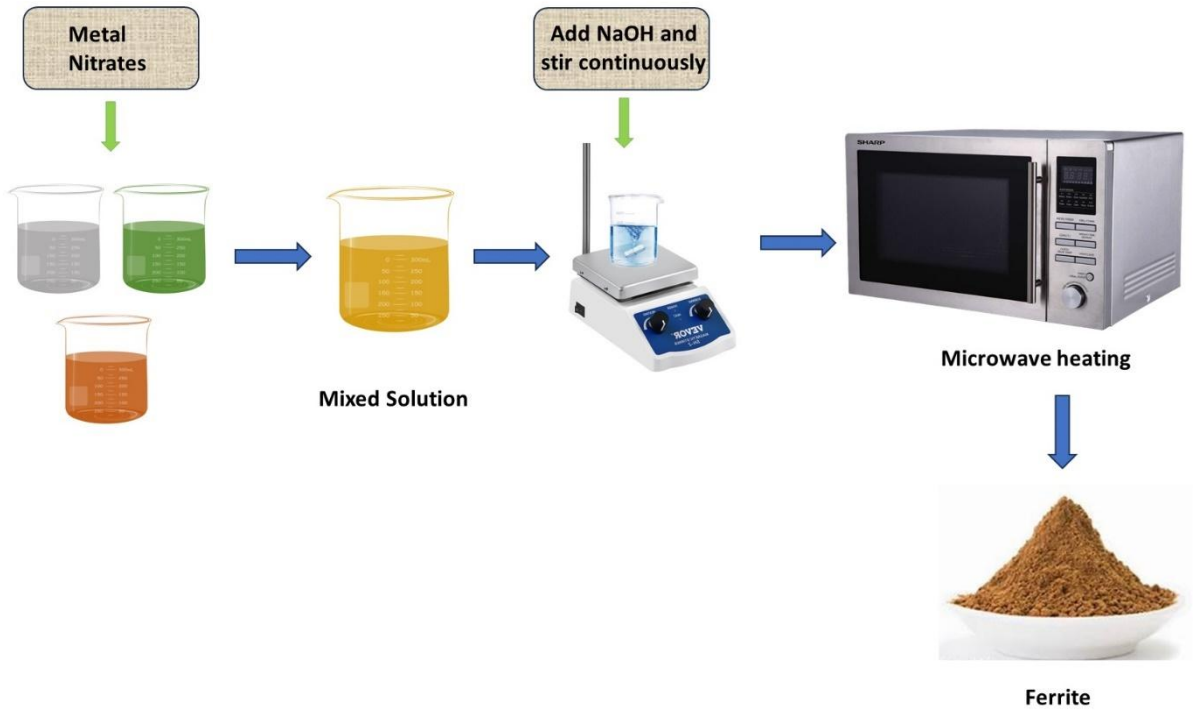

Figure 2.4: Schematic illustration for the microwave method.

2.1.5 Solid-state method

This method describes interactions that occur without involvement of solvent mediums or controlled vapour-phase interactions. Solvothermal techniques are frequently viewed as a component of the solid-state arsenal since these reactions typically include extreme states such as high pressure or high temperature. When other techniques failed, solid-state techniques were eventually used to create bulk crystals, refractory ceramics, and glasses [147-150]. The solid-state approach is regarded as one of the quickest ways to synthesize a variety of materials. To produce the desired products, this procedure enables the precise proportional combination of high-purity oxide components. Both dry and wet milling medium are used to blend these materials for prolonged periods of time [151, 152].

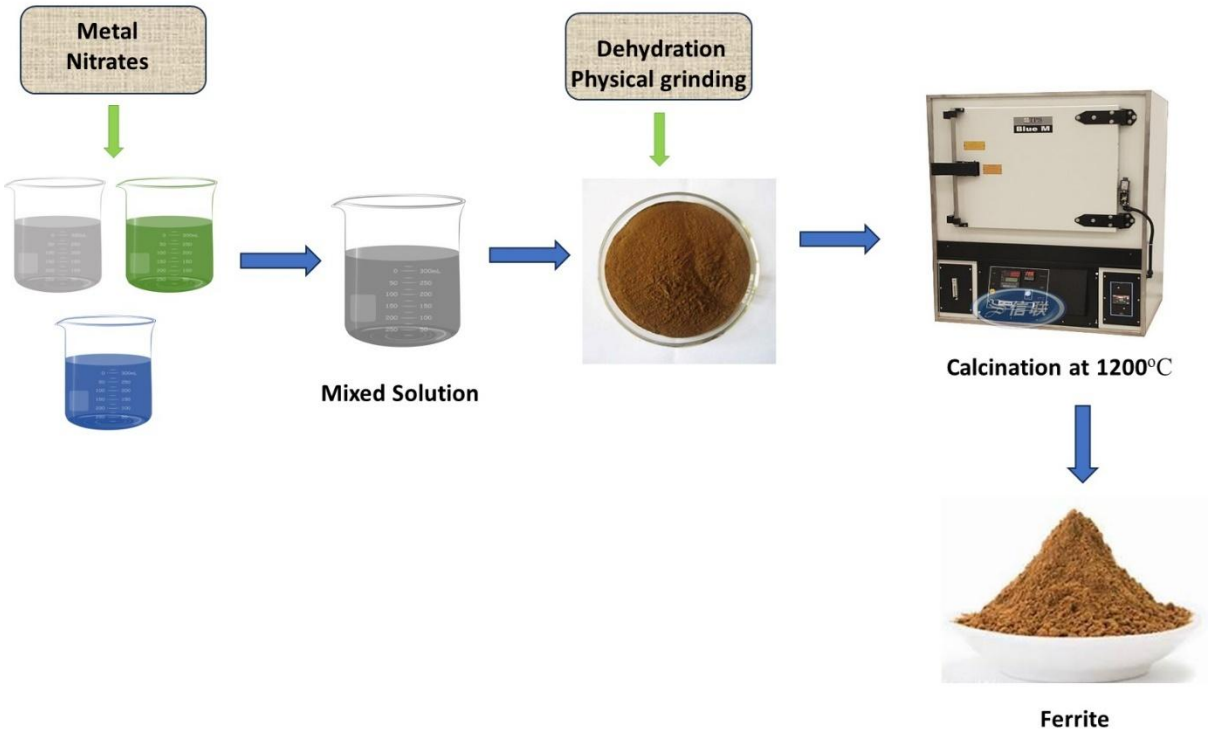

Figure 2.5: Schematic illustration for the solid-state method.

2.2 Applications of spinel ferrites in the adsorption field

Literature studies have demonstrated the widespread applications of ferrites and their composites across diverse fields including medical, aeronautical, electrical engineering, magnetization technologies, and adsorption methodologies [144, 153-157]. In recent times, the use of ferrites specifically in the domain of adsorption has shown significant interest among researchers, with their composite materials exhibiting substantial promise in wastewater treatment applications. In general, polluted water contains various contaminants from sewage and industrial wastes, encompassing a range of substances such as organic pollutants, heavy metals, dyes, inorganic chemicals. Research investigations have indicated that the usage of ferrites in removal of impurities present in wastewater is highly effective. The application of ferrites in the purification of water has attracted attention due to their exceptional adsorption properties, demonstrating a remarkable capability to remove diverse impurities and contaminants from affected water sources. These ferrites and their composite materials exhibit a high potential in efficiently extracting pollutants from wastewater, contributing to the remediation of environmental pollution caused by various industrial and domestic sources. Ongoing research and exploration of ferrites, particularly spinel ferrites, highlight the promising potential of these materials for addressing the challenges associated with water

pollution. Their effectiveness in adsorption processes implies a significant advancement in developing more efficient and sustainable solutions for the purifying polluted water resources, supporting environmental conservation efforts. As per literature survey, removal efficiency (%) for different ferrite materials is shown below (Table 2.2).

Table 2.2: Dye removal efficiency (%) for different ferrite materials.

Ferrites	**Dyes**	**Removal efficiency (%)**	**References**
$MnFe_2O_4$	Azo dye Acid Red B	86	[14]
$MnFe_2O_4$	COD	73.5	[19]
$MnFe_2O_4$	MB	99.5	[24]
$MnFe_2O_4$	CR	87	[25]
$NiFe_2O_4$	MB, Fuchsine Red and MV	97	[26]
$MnFe_2O_4$	Tetracycline	91.12	[32]
$CuFe_2O_4$	MB	95.9	[33]
$Zn_{1-x}Co_xFe_2O_4$	MB	95.4	[34]
$NiFe_2O_4$	Reactive Blue 5	90	[35]
$ZnFe_2O_4$	MO and RhB	96	[36]
MFe_2O_4 (M= Co, Ni, Cu, and Zn)	Remazol Black 5	97	[41]
$ZnFe_2O_4$	Procion Red	85	[44]
$ZnFe_2O_4$	Azo dye and Acid Blue 113	92 and 98	[45]
$ZnFe_2O_4$	Remazol Brilliant yellow and cationic safranine-O	90	[46]
$NiFe_2O_4$/KAOLINITE	MO	95.8	[47]
$ZnFe_2O_4$	Reactive Yellow 86	94	[49]
$CoFe_{1.9}Mo_{0.1}O_4$	MB	95	[51]
$NiFe_2O_4$	MO	99	[52]
$ZnFe_2O_4$	MB, Rose Bengal, Evans Blue and Indigo Carmine	98, 99, 82 and 87	[54]
$Zn_{1-x}Cu_xFe_2O_4$	MB	83	[56]

$NiFe_2O_4$	Acid red dye B	99	[57]
$NiFe_2O_4$ Polyaniline	MB	80	[58]
$NiRu_xFe_{2-x}O_4$ & $CuRu_xFe_{2-x}O_4$	Remazol deep red, Ciprofloxacin	89	[59]
$NiFe_2O_4$	RhB	72.80	[62]
$CoFe_2O_4$	TDS, BOD, COD, and chromium	90.83, 52.72, 48.07 and 23.75	[63]
$CuFe_2O_4$, $CoFe_2O_4$, $MnFe_2O_4$ & $ZnFe_2O_4$	Acid orange 7 and Diclofenac (Azo dye)	96.8 and 67.7	[64]
$CoFe_2O_4$	Indigo carmine dye	98	[65]
$MnFe_2O_4$	Ciprofloxacin and Carbamazepine	80.25	[68]
$Mg_{1-x}Zn_xFe2O4$	CR	33.3- 99.9	[69]
$MnFe_2O_4$ /GO	Pb^{2+} and neutral red (NR)	98.8 and 94	[70]
$MgFeCrO_4$	Direct Black 122	96	[71]
$Co_{0.1}Al_{0.03}Fe_{0.17}O_{0.4}$	MB	93	[73]
$Cu_{0.5}Mg_{0.5}Fe_2O_4$–TiO_2	RhB	6.8	[79]
$CuFe_2O_4$, $CoFe_2O_4$ and $NiFe_2O_4$	MB	79	[80]
$Co_{0.5}Cu_{0.5}S_{mx}Fe_{2-x}O_4$	RhB	94.36	[82]
Ce-doped $CuFe_2O_4$	RhB	88	[83]
$ZnO/NiFe_2O_4$	CR	94	[84]
Cu–$MgFe_2O_4$	MB	97	[85]
Fe_3O_4/Zeolite NaA	MB	~96.8	[86]
$CoFe_2O_4$	Indigo carmine dye	98	[87]
$Ca_{1-x}Cu_xFe_2O_4$	MB	96	[88]

$TiO_2/ZnFe_2O_4$, $ZnFe_{1.98}La_{0.02}O_4$	MB	97	[89]
$MgFe_2O_4$	MB	82-87	[90]
Ce-doped cobalt/nickel mixed ferrites	CR	73.4	[99]
Chemical mediated Manganese Ferrite/Green Manganese Ferrite	Metanil Yellow	80.2, 99.12	[100]
$Co_xZn_{1-x}Fe_2O_4$	CR	89	[101]
Pan−MgF−NC	BG	90.13	[104]
$Mg0.4Zn_{(0.6-x)}CaxFe_2O_4$	RhB	99.5	[105]
$CoFe_2O_4$, $ZnFe_2O_4$	CV	97	[108]
$(Ni_{1-x}M_xFe_2O_4$, [Mn, Zn]	MB	80	[109]
$FeTiO_3$	CV, MG, and MB	99.21, 93.24 and 98.31	[110]
$CoFe_2O_4$ and $NiFe_2O_4$	TYG and AYR	98 and 96	[111]
$Co_{1-x}Zn_xFe_2O_4$/PANI	Reactive Orange-16, Reactive Blue, Reactive Yellow-145, and Disperse Red-1	98	[115]
$CoFe_2O_4$	indigo carmine	82.98	[117]

$ZnFe_2O_4$ and $ZnFe_2O_4@SiO_2$	MB	95, 93	[119]
$MnFe_2O_4$	safranine T	80.94	[120]
$Ni_{0.5}Zn_{0.5}Fe_2O_4$	MaG and MG	95	[121]
$Ni_{0.5}Co_{0.5}La_xFe_{2-x}O_4$ (x = 0; 0.01; 0.025; 0.05)	CR	90	[122]
$Cu_xNi_{1-x}Tb_yFe_{2-y}O_4$	CR, CV and DS	91 ,77 and 81	[124]
$ZnFe_2O_4$	RhB	92.67	[125]
$CaFe_2O_4$	CR	95.74	[126]
Ni and Mn co-doped $ZnFe_2O_4$	MG	94.6	[128]
$ZnFe_2O_4$-PANI	CV	85	[129]
$Ni_{0.5}Zn_{0.5-x}Cu_xFe_2O_4$;	ARS	100	[130]
$Zn_{0.5}Mg_{0.5}Fe_2O_4$	MaG	89.2	[131]
$Zn_{0.5}Ni_{0.3}Cu_{0.2}Fe_{2-x}Gd_xO_4$ (x = 0, 0.025, 0.05, 0.075, 0.1)	RhB	99.84	[132]
$CuFe_2O_4$	CR	94.95	[133]

MgF-Cs-Ze, NiF-Cs-Ze, and MgF@NiF-Cs-Ze	AR	99.2	[134]
$Bi_{1-x}Bent_xFe_{1-y}Co_yO_3$ (x = 0.00 – 0.03, y = 0.00 – 0.15)	MO	92	[135]
$CoFe_{2-x}Al_xO_4$	NBB	95, 95.3, 93.04, 77 and 91	[137]
$Zn_{(1-2x)}Ag_xCr_xFe_2O_4$, (where x = 0.0 to 0.25)	MaG	97	[139]

2.3 Need for study

Presently, the demand for clean water is increasing day by day across the world. Research studies reveal that the adsorption process has a high potential for wastewater treatment with effective results. Different types of adsorbents have been used to purify contaminated water, and among them ferrites have emerged as a fast-developing and promising area for wastewater treatment. A perusal of the literature review suggests that among various synthesis methods, combustion is one of the simple, less time-consuming, with simple design and economical methods for the synthesis of metal ferrites. The use of both individual and doped ferrites has proved these magnetic materials as excellent alternative adsorbents with high adsorption capacities. Therefore, there is a further need to explore doped-mixed transition metal ferrite for removing dyes from wastewater. Very little work has been reported on the doped ferrites, therefore, further exploration is required in this area. The current research study aims for synthesizing doped mixed transition metal ferrites for adsorption of different dyes from aqueous solutions. For this, the objective of the current study is to synthesize series of doped transition metal ferrites with varied compositions. The next step of this research work is to study the adsorption behavior of these ferrites for removal of dyes from aqueous solutions. The use of Al-doped mixed transition metal ferrite is a new field of research in adsorption that is both cost-effective and environment friendly.

2.4 Objectives of the research work

Based on literature survey and owing to remarkable adsorption properties of ferrites, to fill this research gap, following objectives are proposed:

1. Preparation of Al-doped mixed spinel ferrites, $Al_xM_{0.7}Mn_{0.3}Fe_{2-x}O_4$, (Where M = Co, Ni, Cu, Zn) by solution combustion method.
2. Physicochemical and structural properties characterization by using various techniques.
3. Applications of as-synthesized ferrite materials for adsorption of different dyes from their aqueous solutions.

References

1. Thomas D., Erika A.L. and Oana C., Recent Advances in Synthesis and Applications of MFe_2O_4 (M = Co, Cu, Mn, Ni, Zn) Nanoparticles, Nanomater., 11(6), **2021**, 1560.
2. Ajitanshu V., Kishor K., Sunil D. and Aman K., A comprehensive study on structure, properties, synthesis and characterization of ferrites, AIMS Mater. Sci., 7(6), **2020**, 800-835.
3. Pullar R.C., Hexagonal ferrites: a review of the synthesis, properties and applications of hexaferrite ceramics. Prog. Mater. Sci., 57(7), **2012**, 1191-1334.
4. Amal S., Hind H., Rachid E., Mohamed A., Samir Q. and Noureddine B., Spinel ferrites nanoparticles: Synthesis methods and application in heterogeneous Fenton oxidation of organic pollutants – A review, Appl. Surf. Sci. Adv., 6, **2021**, 100145.
5. Manju B.G. and Raji P., Synthesis and magnetic properties of nano-sized $Cu_{0.5}Ni_{0.5}Fe_2O_4$ via citrate and aloe vera: A comparative study, Ceram. Int., 44(7), **2018**, 7329–7333.
6. Malik M.A., Wani M.Y. and Hashim M.A., Microemulsion method: A novel route to synthesize organic and inorganic nanomaterials: 1st Nano Update, Arab. J. Chem., 5(4), **2012**, 397-417.
7. Zheng X., Yu S.H., Sun R., Yang W.H. and Du R., Microstructure and properties of ferrite/organic nanocomposite prepared with microemulsion method, Mater. Sci. Forum., 722, **2012**, 31-38.
8. Demirel B., Yenigün O. and Bekbolet M., Removal of Cu, Ni and Zn from wastewaters by the ferrite process, Environ. Technol., 20(9), 1**999**, 963-970.
9. Navratil J.D., Wastewater treatment technology based on iron oxides, Nat. Microporous Mater. Environ. Technol., 362, **1999**, 417-424.
10. Prieto F., Barrado E., Medina J. and Lopez-Gomez F.A., Characterisation of zinc bearing-ferrites obtained as by-products of hydrochemical waste-water purification processes, J. Alloys Compd., 325(1-2), **2001**, 269-275.
11. Xiang L., Yin Y.P. and Jin Y., Hydrothermal formation of Ni-Zn ferrite from heavy metal co-precipitates, J. Mater. Sci., 37, **2002**, 349-352.

12. Kim Y.I, Kim D. and Lee C.S., Synthesis and characterization of $CoFe_2O_4$ magnetic nanoparticles prepared by temperature-controlled coprecipitation method, Physica B: Condens. Matter., 337(1-4), **2003**, 42-51.

13. Mehmet E. and Fikret T., Chromium removal from aqueous solution by the ferrite process, J. Hazard. Mater., 109(1-3), **2004,** 71-77.

14. Rongcheng W. and Jiuhui Q., Removal of water-soluble azo dye by the magnetic material $MnFe_2O_4$, J. Chem. Technol. Biotechnol., 80(1), **2005**, 20-27.

15. Hwang Y., Microwave absorbing properties of NiZn-ferrite synthesized from waste iron oxide catalyst, Mater. Lett., 60(27), **2006**, 3277-3280.

16. Yang J., Peng J., Liu K., Guo R., Xu D. and Jia J., Synthesis of ferrites obtained from heavy metal solutions using wet method, J. Hazard. Mater., 143(1-2), **2007,** 379-385.

17. Dehghan R., Seyyed Ebrahimi S.A. and Badiei A., Investigation of the effective parameters on the synthesis of Ni-ferrite nanocrystalline powders by coprecipitation method, J. Non-Cryst. Solids, 354(47-51)**, 2008**, 5186-5188.

18. Hessien M.M., Rashad M.M. and El-Barawy K., Controlling the composition and magnetic properties of strontium hexaferrite synthesized by co-precipitation method, J. Magn. Magn. Mater., 320(3-4), **2008,** 336-343.

19. Lv S., Chen X., Ye Y., Yin S., Cheng J. and Xia M., Rice hull/$MnFe_2O_4$ composite: Preparation, characterization and its rapid microwave-assisted COD removal for organic wastewater, J. Hazard. Mater., 171(1-3), **2009**, 634-639.

20. Phu N.D., Phong P.C., Chau N., Luong N.H., Hoang L.H. and Hai N.H., Arsenic removal from water by magnetic $Fe_{1-x}Co_xFe_2O_4$ and $Fe_{1-y}Ni_yFe_2O_4$ nanoparticles, J. Exp. Nanosci., 4(3), **2009**, 253-258.

21. Hankare P.P., Jadhav S.D., Sankpal U.B., Chavan S.S., Waghmare K.J. and Chougule B.K., Synthesis, characterization and effect of sintering temperature on magnetic properties of MgNi ferrite prepared by co-precipitation method, J. Alloys Compd., 475(1-2), **2009**, 926-929.

22. Sung X., Wang S., Lu J. and Zhang G., Removal of Heavy Metals by the Ferrite Process, Conference on Environ. Pollut. Public Health, **2010**, 1030-1032.

23. Koseoglu Y., Superparamagnetic $NiFe_2O_4$ Nanoparticles to Remove Arsenic From Drinking Water, Proceedings of 10th Second International Symposium on Sustainable, **2010**, 439-447.

24. Hou X., Feng J., Ren Y., Fan Z. and Zhang M., Synthesis and adsorption properties of spongelike porous $MnFe_2O_4$, Colloids and Surfaces A: Physicochem. Eng. Aspects, 363(1-3), **2010,** 1-7.

25. Wang Y.Q., Cheng R.M., Wen Z. and Zheo L.J., Synthesis and Characterization of Single-Crystalline $MnFe_2O_4$ Ferrite Nanocrystals and Their Possible Application in Water Treatment, Eur. J. Inorg. Chem., 2011(19), **2011**, 2942-2947.

26. Xiangyu H., Jing F., Xiaohan L., Yueming R., Zhuangjun F., Tong W., Jian M. and Milin Z., Synthesis of 3D porous ferromagnetic $NiFe_2O_4$ and using as novel adsorbent to treat wastewater, J. Colloid Interface Sci., 362(2), **2011**, 477-485.

27. Rahimi R., Kerdari H., Rabbani M. and Shafiee M., Synthesis, characterization and adsorbing properties of hollow Zn-Fe_2O_4 nanospheres on the removal of Congo red from aqueous solution, Desalin., 280(1-3), **2011**, 412-418.

28. Raghavender A.T., Shirsath S.E. and Kumar K.V., Synthesis and study of nanocrystalline Ni–Cu–Zn ferrites prepared by oxalate-based precursor method, J. Alloys Compd., 509(25), **2011,** 7004-7008.

29. Li N., Zheng M., Chang X., Ji G., Lu H., Xue L., Pan L. and Cao J., Preparation of magnetic $CoFe_2O_4$-functionalized graphene sheets via a facile hydrothermal method and their adsorption properties, J. Solid-State Chem., 184(4), **2011**, 953–958.

30. Kumar G.R., Kumar K.V. and Venudhar Y.C., Synthesis, structural and magnetic properties of copper substituted Nickel Ferrites by Sol-gel method, Mater. Sci. and Applic., 3(2), **2012,** 87-91.

31. Becker F.L., Rodríguez D. and Schwab M., Magnetic removal of cobalt from wastewater by ferrite co-precipitation, procedia Mater. Sci., 1, **2012,** 644-650.

32. Shao L., Ren Z., Zhang G. and Chen L., Facile synthesis, characterization of a $MnFe_2O_4$/activated carbon magnetic composite and its effectiveness in tetracycline removal, Mater. Chem. Phys., 135(1), **2012**, 16-24.

33. Rashad M.M., Mohamed R.M., Ibrahim M.A., Ismail L.F.M. and Abdel-Aal E.A., Magnetic and catalytic properties of cubic copper ferrite nanopowders synthesized from secondary resources, Adv. Powder Technol., 23(3), **2012**, 315-323.

34. Fan G., Tong J. and Li F., Visible-light-induced photocatalyst based on cobalt-doped zinc ferrite nanocrystals, Ind. Eng. Chem. Res., 51(42), **2012**, 13639-13647.

35. Khosravi I. and Eftekhar M., Characterization and evaluation catalytic efficiency of $NiFe_2O_4$ nano spinel in the removal of reactive dye from aqueous solution, Powder Technol., 250, **2013**, 147-153.

36. Meidanchi A. and Akhavan O., Superparamagnetic zinc ferrite spinel–graphene nanostructures for fast wastewater purification, Carbon, 69, **2014**, 230-238.

37. Yattinahalli S.S., Mathad S.N. and Kapatkar S.B., Structural studies of zinc ferrite synthesized at low temperature, the int. reviewer, 1(1), **2014**, 5-8.

38. Zhang F., Wei C., Hu Y. and Wu H., Zinc ferrite catalysts for ozonation of aqueous organic contaminants: phenol and bio-treated coking wastewater, Sep. Purif. Technol., 15(2), **2015,** 625-635.

39. Srivastava V., Sharma Y.C. and Sillanpaa M., Application of nano-magnesium ferrite (n-$MgFe_2O_4$) for the removal of Co^{2+} ions from synthetic wastewater: Kinetic, equilibrium and thermodynamic studies. Appl. Surf. Sci., 338**, 2015**, 42-54.

40. Sezgin N., Yalcin A. and Koseoglu Y., $MnFe_2O_4$ nano spinels as potential sorbent for adsorption of chromium from industrial wastewater, Desalination Water Treat., 57(35), **2016**, 16495-16506.

41. Samoila P., Cojocaru C., Cretescu I., Stan C.D., Nica V., Sacarescu L. and Harabagiu V., Nanosized spinel ferrites synthesized by sol-gel autocombustion for optimized removal of azo dye from aqueous solution. J. Nanomat., 16, **2015**, 237.

42. Anchieta C.G., Severo E.C., Rigo C., Mazutti M.A., Kuhn R.C., Muller E.I., Flores E.M.M., Moreira R.F.P.M. and Foletto E.L., Rapid and facile preparation of zinc ferrite ($ZnFe_2O_4$) oxide by microwave-solvothermal technique and its catalytic activity in heterogeneous photo-Fenton reaction, Mater. Chem. Phys., 160, **2015**, 141-147.

43. Atia T.A., Altimaria P., Moscardini E., Pettiti I., Toro L. and Pagnanelli F., Synthesis and characterization of copper ferrite magnetic nanoparticles by hydrothermal route, Chem. Eng. Transcations, 47, **2016**, 151-156.

44. Mandal S., Natarajan S., Tamilselvi A. and Mayadevi S., Photocatalytic and antimicrobial activities of zinc ferrite nanoparticles synthesized through soft chemical route: a magnetically recyclable catalyst for water/wastewater treatment. J. Env. Chem. Eng., 4(3), **2016**, 2706-2712.

45. Gu W., Xie Q., Qi C., Zhao L. and Wu, D., Phosphate removal using zinc ferrite synthesized through a facile solvothermal technique. Powder Technol., 301, **2016,** 723-729.

46. Dhiman M., Sharma R., Kumar V. and Singhal S., Morphology controlled hydrothermal synthesis and photocatalytic properties of $ZnFe_2O_4$ nanostructures. Ceram. Int., 42(11), **2016**, 12594-12605.

47. Cojocaru S., Borhan B., Mykhailovych V., Cucu-Man S., Melniciuc-Puica N., Calton O.F., Hulea V., Cazacu M., Palamaru M.N. and Iordan A.R., Nanosized $NiFe_2O_4$/KAOLINITE Composite as adsorbent for organic dyes, Academia Romana, Rev. Roum. Chim., 62(8-9), **2017**, 687-698.

48. Jung K-W., Lee S. and Lee Y.J., Synthesis of novel magnesium ferrite ($MgFe_2O_4$)/biochar magnetic composites and its adsorption behavior for phosphate in aqueous solutions, Bioresour. Technol., 245, **2017**, 751-759.

49. Suppuraj P., Thirunarayanan G., Swaminathan M. and Muthuvel I., Facile synthesis of spinel nanocrystalline $ZnFe_2O_4$: enhanced photocatalytic and microbial applications, Mater. Sci. App. Chem., 34(1), **2017**, 5-11.

50. Singh R., Kumar M., Tashi L., Khajuria H. and Sheikh H.N., Hydrothermal synthesis of nitrogen-doped graphene supported cobalt ferrite ($NG@CoFe_2O_4$) as photocatalyst for the methylene blue dye degradation, Nanochem Res., 3(2), **2018**, 149-159.

51. Amar I.A., Sharif A., Alkhayali M.M., Jabji M.A., Altohami F., Qadir A. and Ahwidi M.M., Adsorptive removal of methylene blue dye from aqueous solutions using $CoFe_{1.9}Mo_{0.1}O_4$ magnetic nanoparticles, Iran. J,Energy Environ., 9 (4), **2018,** 247-254.

52. Ayazi Z., Khoshhesab Z.M. and Amani-Ghadim A., Synthesis of nickel ferrite nanoparticles as an efficient magnetic sorbent for removal of an azo-dye: Response surface methodology and neural network modelling, Nanochem Res., 3(1), **2018**, 109-123.

53. Jung K-W., Lee S.Y. and Lee Y.J., Facile one-pot hydrothermal synthesis of cubic spinel-type manganese ferrite/biochar composites for environmental remediation of heavy metals from aqueous solutions, Bioresour. Technol., 261, **2018**, 1-9.

54. Patil S.B., Naik H.S.B., Nagaraju G., Viswanath R., Rashmi S.K. and Kumar M.V., Sugarcane juice mediated eco-friendly synthesis of visible light active zinc ferrite nanoparticles: Application to degradation of mixed dyes and antibacterial activities. Mater. Chem. Phys., 212, **2018,** 351-362.

55. Shen M., Fu L., Tang J., Liu M., Song Y., Tian F., Zhao Z., Zhang Z. and Dionysiou D.D., Microwave hydrothermal-assisted preparation of novel spinel-$NiFe_2O_4$/natural mineral composites as microwave catalysts for degradation of aquatic organic pollutants, J. Hazard. Mater., 350, **2018**, 1-9.

56. Camacho-Gonzalez M.A. Quezada-Cruz M., Ceron-Montes G.I., Ramirez-Ayala M.F., Hernandez-Cruz L.E. and Garrido-Hernandez A., Synthesis and characterization of magnetic zinc-copper ferrites: antibacterial activity, photodegradation study and heavy metals removal evaluation, Mater. Chem. Phys., 236, **2019**, 121808.

57. Selima S.S., Khairy M., Bayoumy W.A., Mousa M.A., Influence of preparation method on structural, optical, magnetic, and adsorption properties of nano-$NiFe_2O_4$, Environ. Sci. Pollut. Res., 26, **2019**, 21484-21494.

58. Singh N.B., Agrawal S. and Rachna K.M., Methylene blue dye removal from water by nickel ferrite polyaniline nanocomposite, J. Sci. Ind. Res., 78(2), **2019,** 118-121.

59. Singh S., Kaur P., Barsal S. and Singhal S., Enhanced photocatalytic performance of Ru-doped spinel nano ferrites for treating recalcitrant organic pollutants in wastewater, J. Sol-Gel Sci. Technol., 92, **2019**, 760-774.

60. Bhagwat V.R., Humbe A.V., More S.D. and Jadhav K.M., Sol-gel auto combustion synthesis and characterizations of cobalt ferrite nanoparticles: Different fuels approach, Mater. Sci. Eng. B, 248, **2019**, 114388.

61. Alia A.E., Salema W.M., Younes S.M. and Elabdeen A.Z., Ferrite Nanocomposite (Rice Straw-$CoFe_2O_4$) as New Chemical Modified for Treatment of Heavy Metal from Waste Water, Hydrol. Curr. Res., 10(1), **2019,** 1000311.

62. Qu J., Che T., Shi L., Lu Q. and Qi S., A novel magnetic silica supported spinel ferrites $NiFe_2O_4$ catalyst for heterogeneous Fenton-like oxidation of rhodamine B, Chin. Chem. Lett., 30(6), **2019**, 1198-1203.

63. Albalah M.A., Alsabah Y.A. and Mustafa D.E., Characteristics of co-precipitation synthesized cobalt nano ferrites potential in industrial wastewater treatment, SN App. Sci., 2, **2020,** 804.

64. Xian G., Kong S., Li Q., Zhang G., Zhou N., Du H. and Niu L., Synthesis of spinel ferrite MFe_2O_4 (M = Co, Cu, Mn, and Zn) for persulfate activation to remove aqueous organics: effects of M-Site metal and synthetic method, Front. Chem., 8, **2020**, 177.

65. Rodríguez-Chueca J., Barahona-Garciaa E., Blanco-Gutiérrez V., Isidoro-Garcíab L. and Dos Santos-García A.J., Magnetic $CoFe_2O_4$ ferrite for peroxymonosulfate activation for disinfection of wastewater, Chem. Eng. J., 398, **2020**, 125606.

66. Verma B. and Balomajumder C., Synthesis of magnetic nickel ferrites nanocomposites: An advanced remediation of electroplating wastewater, J. Taiwan Inst. Chem. Eng., 112, **2020**, 106-115.

67. Rashdan S.A. and Hazeem L.J., Synthesis of spinel ferrites nanoparticles and investigating their effect on the growth of microalgae Picochlorum species, Arab J. Basic Appl. Sci., 27(1), **2020**, 134-141.

68. Hermosilla D., Han C., Nadagouda M., Machala L., Gasco A., Campo P. and Dionysioi D.D., Environmentally friendly synthesized and magnetically recoverable designed ferrite photo-catalysts for wastewater treatment applications, J. Hazard. Mater., 381, **2020**, 121200.

69. Tatarchuk T., Myslin M., Mironyuk I., Bououdina M., Pedziwiatr A.T., Gargula R., Bogacz B.F. and Kurzydlo P., Synthesis, morphology, crystallite size and adsorption properties of nanostructured Mg-Zn ferrites with enhanced porous structure, J. Alloys Compd., 819, **2020,** 152945.

70. Soletti L.S., Ferreira M.E.C., Kassada A.T., Abreu Filho B.A., Bergamasco R. and Yamaguchi N.U., Manganese ferrite graphene nanocomposite synthesis and the investigation of its antibacterial properties for water treatment purposes, Rev. Ambient. Agua, 15(4), **2020**, e2515.

71. Moradnia F., Fardood S.T., Ramazani A. and Gupta V.K., Green synthesis of recyclable MgFeCrO4 spinel nanoparticles for rapid photodegradation of direct black 122 dye, J. Photochem. Photobiol. A., 392, **2020**, 112433.

72. Qamar S., Akhtar M.N., Batoo K.M. and Raslan E.H., Structural and magnetic features of Ce doped Co-Cu-Zn spinel nano ferrite prepared using the sol-gel self-ignition method. Ceram. Int., 46(10), **2020**, 14481-14487.

73. Abbas N., Rubab N., Sadiq N., Manzoor S., Khan M.I., Garcia J.F., Aragoa I.B., Tariq M., Akhtar Z. and Yasmin G., Aluminium-Doped cobalt ferrite as an efficient photocatalyst for the abatement of methylene blue, Water, 12(8), **2020**, 2285.

74. Zhao J., Cao J., Zhao Y., Zhang T., Zheng D. and Li C., Catalytic ozonation treatment of papermaking wastewater by Ag-doped $NiFe_2O_4$: Performance and mechanism, J. Envir. Sci., 97, **2020**, 75-84.

75. Ghasemi R., Echeverria J., Perez-Landazabal J.I., Beato-Lopez J.J., Naseri M. and Gómez-Polo C., Effect of Cu substitution on the magnetic and magnetic induction heating response of $CdFe_2O_4$ spinel ferrite, J. Magn. Magn. Mater., 499, **2020**, 166201.

76. Qamar S., Akhtar M.N., Aleem, W., Rehman Z., Khan A.H., Ahmad A. Batoo K.M. and Aamir M., Graphene anchored Ce doped spinel ferrites for practical and technological applications, Ceram. Int., 46(6), **2020**, 7081-7088.

77. Ramu A.G., Salla S., Chandrasekaran S., Silambarasan P., Gopi S., Seo S-Y., Yun K. and Choi D., A facile synthesis of metal ferrites and their catalytic removal of toxic nitro-organic pollutants, Environ. Pollut., 270, **2020,** 116063.

78. Dojcinovic M.P., Vasiljevic Z.Z., Pavlovic V.P., Barisic D., Pajic D., Tadic N.B. and Nikolic, Mixed Mg-Co spinel ferrites: Structure, morphology, magnetic and photocatalytic properties, J. Alloys Compd., 855(1), **2020**, 157429

79. Tran C.V., La D.D., Hoai P.N.T., Ninh H.D., Hong P.N.T., Vu T.H.T., Nadda A.K., Nguyen X.C., Nguyen D.D. and Ngo H.H., New TiO_2-doped Cu–Mg spinel-ferrite-based

photocatalyst for degrading highly toxic rhodamine B dye in wastewater, J. Hazard. Mater., 420**, 2021**, 126636.

80. Katubi K.M.M., Alsaiari N.S., Alzahrani F.M., Siddeeg S.M. and Tahoon M.A., Synthesis of Manganese Ferrite/Graphene Oxide Magnetic Nanocomposite for Pollutants Removal from Water, Processes, 9(4), **2021**, 589.

81. Singh S., Chaudhary P., Srivastava R., Tripathi R.K., Kumar R. and Yadav B.C., Improved growth of nano tin ferrites with their decoration on carbon foam for wastewater treatment, Environ. Nanotechnol. Monit. Manage., 16, **2021**, 100546.

82. Abdo M.A. and El-Daly A.A., Sm-substituted copper-cobalt ferrite nanoparticles: Preparation and assessment of structural, magnetic and photocatalytic properties for wastewater treatment applications, J. Alloys Compd., 883, **2021**, 160796.

83. Keerthana S.P., Yuvakkumar R., Ravi G., Pavithra S., Thambidurai M., Dang C., and Velauthapillai D., Pure and Ce-doped spinel $CuFe_2O_4$ photocatalysts for efficient rhodamine B degradation, Environ. Res., 200, **2021**, 111528.

84. Mapossa A.B., Mhike W., Adalima J.L. and Tichapondwa S., Removal of organic dyes from water and wastewater using magnetic ferrite-based titanium oxide and zinc oxide nanocomposites, Catal., 11(12), **2021**, 1543.

85. George M., Ajeesha T.L., Manikandan A., Anantharaman A., Jansi R.S., Kumar E.R., Slimani Y., Almessiere M.A. and Baykal A., Evaluation of Cu–$MgFe_2O_4$ spinel nanoparticles for photocatalytic and antimicrobial activates, J. Phys. Chem. Solids, 153**, 2021**, 110010.

86. Tran N.B.T., Duong N.B. and Le N.L., Synthesis and Characterization of Magnetic Fe_3O_4/Zeolite NaA Nanocomposite for the Adsorption Removal of Methylene Blue Potential in Wastewater Treatment, J. Chem., 2021, **2021**, 14.

87. Raghavendra N., Nagaswarupa H.P., Shekhar T.R.S., Mylarappa M., Surendra B.S., Prashantha S.C., Basavaraju N., Kumar C.R.R. and Kumar M.R.A., Electrochemical sensor studies and optical analysis of developed clay-based $CoFe_2O_4$ ferrite NPs, Sens. Int., 2, **2021**, 100083.

88. Ajeesha T.L., Manikandan A., Anantharaman A., Jansi S., Durka M., Almessiere M.A., Slimani Y., Baykal A., Asiri A.M., Kasmery H.A., Khan A., Khan A.A.P., Madhu P., and

George M., Structural investigation of Cu doped calcium ferrite ($Ca_{1-x}Cu_xFe_2O_4$; x = 0, 0.2, 0.4,0.6, 0.8, 1) nanomaterials prepared by co-precipitation method, J. Mater. Researchnol., 18, **2022**, 705-719.

89. Coromelcl C., Neamtu M., Ignat M., Samoila P., Zaltarior M.F. and Palamaru M., Ultrasound-assisted thesis of hetero structured $TiO_2/ZnFe_2O4$ and $TiO_2/ZnFe_{1.98}La_{0.02}O_4$ systems as tunable photocatalysts for efficient organic pollutants removal, Ceram. Int., 48(4), **2022**, 4829-4840.

90. Ivanets A., Prozorovich V., Roshchina M., Sychova O., Srivastava V. and Sillanpaa M., Methylene blue adsorption on magnesium ferrite: Optimization study, kinetics and reusability, Mater. Today Commun., 31, **2022**, 103594.

91. Shah P., Joshi K., Shah M., Unnarkat A. and Patel F.J., Photocatalytic dye degradation using nickel ferrite spinel and its nanocomposite, Environ. Sci. Pollut. Res., 29, **2022**, 78255-78264.

92. Jasrotia R., Singh J., Mittal S. and Singh H., Synthesis of CTAB modified ferrite composite for the efficient removal of brilliant green dye Int. J. Environ. An. Ch., **2022**. https://doi.org/10.1080/03067319.2022.2098485.

93. Xu S., Liu D., Liu A., Sun F., Pan S. and Ouyang H., Adsorption performances and electrochemical characteristics of methyl blue onto magnesium-zinc ferrites, Mater. Res. Express. 9, **2022**, 015002.

94. Kousar T., Aadil M., Zulfiqar S., Somaily H.H., Hassan W., Sabeeh H. and Mohamood F., Temperature controlled synthesis of Co-Ni mixed ferrite nanostructure for the mineralization of azo dye: a novel and facile approach, J. Alloys Compd., 923, **2022**, 166224.

95. Jayalakshmi R., Jeyanthi J. and Sidhaarth K.R.A., Versatile application of cobalt ferrite nanoparticles for the removal of heavy metals and dyes from aqueous solution, Environ. Nanotechnol. Monit. Manag., 17, **2022**, 100659.

96. El-Khawaga A.M., Farrag A.A., Elsayed M.A., El-sayyad G.S. and El-Batal A.I., Promising antimicrobial and azo dye removal activities of citric acid-functionalized magnesium ferrite nanoparticles, J. Clust. Sci., 33, **2022**, 197-213.

97. Babakir B.A.M., Abd Ali L.I. and Ismail H.K., Rapid removal of anionic organic dye from contaminated water using a poly (3-aminobenzoic acid/graphene oxide/cobalt ferrite) nanocomposite low-cost adsorbent via adsorption techniques, Arab. J. Chem., 15(12), **2022**, 104318.

98. Aamir M., Aleen W., Akhtar M.N., Din A.A., Yasmeen G. and Ashiq M.N., Synthesis and characterizations of Co-Zr doped Ni ferrite/PANI nanocomposites for photocatalytic methyl orange dye degradation, Physica B: Condens. Matter., 624, **2022**, 413392.

99. Kousar T., Aadil M., Zulfiqar S., Warsi M.F., Ejaz S.R., Elnaggar A.Y., Fallatah A.M., El-Bahy S.M. and Mohamood F., Wet-chemical synthesis of nanostructured Ce-doped mixed metal ferrites for the effective removal of azo dyes from industrial discharges, Ceram. Int., 48(8), **2022**,11858-11868.

100. Sivashankar R., Sivasubramanian V., Kishore K.A., Sathya A.B., Thirunavukkarasu A., Nithya R. and Deepanraj B., Metanil Yellow dye adsorption using green and chemical mediated synthesized manganese ferrite: An insight into equilibrium, kinetics and thermodynamics. Chemosphere, 307(4), **2022**, 136218.

101. Tarachuk T., Danyliuk N., Kotsyubynsky V., Shumskaya A., Kaniukov E., Ghfar A.A., Naushad M. and Shyichuk A., Eco-friendly synthesis of cobalt-zinc ferrites using quince extract for adsorption and catalytic applications: An approach towards environmental remediation, Chemosphere, 294, **2022**, 133565.

102. Tehmina K., Muhammad A., Sonia Z., Somaily H.H., Warda H., Humera S., Farzana M., Temperature controlled synthesis of Co-Ni mixed ferrite nanostructure for the mineralization of azo dye: A novel and facile approach, J. Alloys Compds., 923, **2022,** 166224.

103. Iqbal Z., Tanweer M.S. and Alam M., Reduced Graphene Oxide-Modified Spinel Cobalt Ferrite Nanocomposite: Synthesis, Characterization, and Its Superior Adsorption Performance for Dyes and Heavy Metals, ACS Omega, 8(7), **2023**, 6126-7243.

104. Das S., Pal A. and Debnath A., Polyaniline-Coated magnesium ferrite nanocomposite: synthesis, characterization, fabrication cost analysis and dye sorption behavior with scale-up design, ChemistrySelect, 8(29), **2023**, e202300928.

105. Kumari S., Dhanda N., Thakur A., Gupta V., Singh S., Kumar R., Hameed S. and Thakur P., Nano Ca–Mg–Zn ferrites as tuneable photocatalyst for UV light-induced

degradation of rhodamine B dye and antimicrobial behavior for water purification, Ceram. Int., 49(8), **2023**, 12469-12480.

106. Sharma A., Rasheed S., Mangla D., Choudhry A., Shukla S. and Chaudhry S.A., Cobalt Ferrite Incorporated Ocimum sanctum Nanocomposite Matrix as an Interface for Adsorption of Organic Dyes: A Sustainable Alternative, ChemistrySelect, 8(5), **2023**, e202203709.
107. Debnath S. and Das R., Strong adsorption of CV dye by Ni ferrite nanoparticles for wastewater purification: Fits well the pseudo-second-order kinetic and Freundlich isotherm model, Ceram. Int., 49(10), **2023**, 16199-16215.
108. Tariq A., Gull M., Shaikh A.J., Hussain S., Hussain R., Haq S. and Waseem M., Grafting the ferrites of cobalt and zinc on MWCNTs for adsorption of crystal violet, Internat. Environ. Sci. Technol., 20, **2023**, 12465-12480.
109. Kumari S., Sharma R., Thakur N. and Kumari A., Removal of organic and inorganic effluents from wastewater by using degradation and adsorption properties of transition metal-doped nickel ferrite, Environ. Sci. Pollut. Res., 31, **2023**, 46526-46545.
110. Koochakzadeh F., Norouzbeigi R. and Shayesteh H., Statistically optimized sequential hydrothermal route for FeTiO3 surface modification: evaluation of hazardous cationic dyes adsorptive removal, Environ. Sci. Pollut. Res., 30, **2023**, 19167-19181.
111. Patil D.J. and Behera S.N. Synthesis and characterization of nanoparticles of cobalt and nickel ferrites for elimination of hazardous organic dyes from industrial wastewater. Environ. Sci. Pollut. Res., 30, **2023**, 53323-53338.
112. Zafar I., Mohd S.T. and Masood A., Reduced Graphene Oxide-Modified Spinel Cobalt Ferrite Nanocomposite: Synthesis, Characterization, and Its Superior Adsorption Performance for Dyes and Heavy Metals**,** ACS Omega, 8(7), **2023,** 6376-6390.
113. Patil D.J. and Behera S.N. Synthesizing nanoparticles of zinc and copper ferrites and examining their potential to remove various organic dyes through comparative studies of kinetics, isotherms, and thermodynamics, Environ. Monit. Assess., 195, **2023,** 591.
114. Irshad I., Munir R., Albasher G., Muneer A., Yaseen M., Zahid M., Nadeem R., Jahan N., Jilani M.I. and Noreen S. Synthesis of metal-doped nano-ferrites $Co_{0.5}Zn_{0.25}M_{0.25}Fe_2O_4$ by co-precipitation method and application as adsorbent and photocatalyst for removal of direct orange-108 acid dye: equilibrium, kinetic and thermodynamic studies, J. Dispers. Sci. Technol., **2023**, 1-20.

115. Bashar M.A., Molla M.T.H., Chandra D., Malitha M.D., Islam M.S., Rahman M.S. and Ahsan M.S., Hydrothermal synthesis of cobalt substitute zinc-ferrite (Co1-xZn x Fe2O4) nanodot, functionalised by polyaniline with enhanced photocatalytic activity under visible light irradiation, Heliyon, 9(4), **2023,** e15381.

116. Rimzim, Singh J., Mittal S. and Singh H., Robust removal of cationic dyes by zinc ferrite composites in single and ternary dye systems, Inorg. Chem. Commun., 153, **2023**, 110756.

117. Al-Wasidi A.S. and Abdelrahman E.A., Simple synthesis and characterization of cobalt ferrite nanoparticles for the successful adsorption of indigo carmine dye from aqueous media, Inorg., 11(12), **2023**, 453.

118. Simi D. and Ratan D., Strong adsorption of CV dye by Ni ferrite nanoparticles for wastewater purification: Fits well the pseudo-second-order kinetic and Freundlich isotherm model, Ceramics Internat., 49 (10), **2023**, 16199-16215.

119. Hashem A.A., Abd El-Wahab R.M., Selim M.M.A. and Badawy A.A. Nanozinc ferrites@silica as efficient adsorbent for dye removal from wastewater: synthesis and adsorption studies, Int. J. Environ. Sci. Technol., 21, **2024**, 9157-9173.

120. Alhalili Z. and Abdelrahman E.A., Facile synthesis and characterization of manganese ferrite nanoparticles for the successful removal of safranine T dye from aqueous solutions, Inorg., 12(1), **2024**, 30.

121. Harzali H. and Azizi M., Investigating the adsorption of Malachite green and Methyl green onto synthesized $Ni_{0.5}Zn_{0.5}Fe_2O_4$ spinel ferrites, J. Environ. Chem. Eng., 12(5), **2024**, 113413.

122. Starko I., Tatarchuk T., Naushad M. and Danyliuk N., Enhanced activity of La-substituted Nickel–Cobalt ferrites in congo red dye removal and hydrogen peroxide decomposition, Water Air Soil Pollut., 235, **2024**, 527.

123. Ashraf S., Munir R., Sayed M., Muneer A., Yaseen M., Zahid M., Mushtaq N. and Noreen S., Synthesis and applications of green waste-mediated nickel, manganese, cobalt, copper, and zinc green ferrites for wastewater remediation, Biomass Conv. Bioref., **2024**. https://doi.org/10.1007/s13399-024-05664-5.

124. Shafa S.T., Basha B., Alrowaili Z.A., Imran M., Sohail M., Al-Buriahi M.S., Shahid M. and Warsi M.F., Synthesis and characterization of Cu and Tb substituted $NiFe_2O_4$@MXene nanocomposite as a new photocatalyst for removal of organic dyes and drugs from industrial wastewater, Results Phys., 63, **2024**, 107844.

125. Al-Wasidi A.S. and AlReshaidan S., Enhanced removal of Rhodamine b dye from aqueous media via adsorption on facilely synthesized zinc ferrite nanoparticles, Inorg., 12(7), **2024**, 191.

126. Al-Kadhi N.S., Al-Senani G.M., Algethami F.K., Shah R.K., Saad F.A., Munshi A.M., Rehman K.U., Khezami L. and Abdelrahman E.A., Calcium ferrite nanoparticles: a simple synthesis approach for the effective disposal of congo red dye from aqueous environments. Inorg., 12(3), **2024**, 69.

127. Sharma, M., Sharma, G., Tyagi, N., Siddiqui A.M. and Khanuja M., Advanced photocatalytic degradation of textile dyes and removal of heavy metal ions from MFe_2O_4 using photo-Fenton mechanism. J. Mater. Sci: Mater. Electron. 35, **2024**, 497.

128. Bibi F., Ahmed A., Ajajy Y., Dawood A.A.A.S., Usman M., Alodhayb A., Mohammad S., Ahmad Z., Kalsoom A. and Iqbal S., Fabrication of Ni and Mn co-doped $ZnFe_2O_4$ spinel ferrites and their nanocomposites with rGO as an efficient photocatalyst for the remediation of organic dyes, Polyhedron, 250, **2024**, 116826.

129. Singh A., Tomar R. and Singh N.B., Efficient removal of crystal violet dye from water using zinc ferrite-polyaniline nanocomposites, Environ. Monit. Assess., 196, **2024**, 569.

130. Mogharbel R., Tahar L.B., Huili H. and Grindi B., Ultrasmall Cu-Substituted NiZn ferrite nanoparticles: efficiency for the removal of the alizarin red S dye and reusability, Arab. J. Sci. Eng., 49, **2024,** 311-337.

131. Fernandes R.J.C., Cardoso B.D., Rodrigues A.R.O., Pires A., Pereira A.M., Araújo J.P., Pereira L. and Coutinho P.J.G., Zinc/Magnesium ferrite nanoparticles functionalized with silver for optimized photocatalytic removal of malachite green. Materials, 17(13), **2024,** 3158.

132. Jadhav S.A., Somvanshi S.B., Gawali S.S., Zakde K. and Jadhav K.M., Rare earth-doped mixed Ni–Cu–Zn ferrites as an effective photocatalytic agent for active degradation of Rhodamine B dye, J. Rare Earths, 42(3), **2024**, 488-496.

133. Parimelazhagan V., Chinta A., Shetty G.G., Maddasani S., Tseng W-L., Ethiraj J., Ayyakannu S.G. and Kumar A.S.K., Process optimization and equilibrium, thermodynamic, and kinetic modeling of toxic congo red dye adsorption from aqueous solutions using a copper ferrite nanocomposite adsorbent. Molecules, 29(2), **2024,** 418.

134. Alzahrani H.K. and Katowah D.F., Chitosan and ferrite nanoparticles modified zeolite (ZSM-5) as adsorbent for the removal of acid red dye from water, Int. J. Polym. Sci., 2024, **2024**, 15.

135. Jamshaid M., Khan H.M., Nazir M.A., Wattoo M.A., Shahzad K., Malik M. and Rehman A.U., A novel bentonite–cobalt doped bismuth ferrite nanoparticles with boosted visible light induced photodegradation of methyl orange: synthesis, characterization and analysis of physiochemical changes. Int. J. Environ. Anal. Chem., 104(5), **2022**, 1186-1201.

136. Beri I., Ayoub M., Fatima N., Dosanjh H.S., Mn-Zn spinel ferrite synthesis by solution combustion method and applications in adsorption of dyes, BIO Web Conf., 86, **2024**.

137. Kumar H., Giri A. and Rai A., Photocatalytic degradation of naphthol blue black dye using undoped and Al-doped cobalt ferrite nanoparticles, Kuwait J. Sci., 51(2), **2024**, 100208.

138. Al-Wasidi A.S., Shah R.K., Abdelrahman E.A. and Mabrouk E-S.M. Facile Synthesis of $CuFe_2O_4$ Nanoparticles for Efficient Removal of Acid Blue 113 and Malachite Green Dyes from Aqueous Media, Inorg., 12(6), **2024**, 143.

139. El-Shater R.E., Abdel-Galeil M.M., Gemeay, A.H., Salama E.S., Kumar R. and Mangood A.H., Synthesis and structural, magnetic, and catalytic characteristics Ag-Cr doped Zn nanoferrite series for dye degradation utilizing advanced oxidation processes, J. Mater. Sci: Mater. Electron., 35, **2024**, 271.

140. Ben amor S. and Ameur S., A facile self-combustion synthesis and characterization of a novel $MgFe_2O_4$ and $MgFe_2O_4$/Bentonite magnetic nanocomposite and their effectiveness in the removal of methyl orange from aqueous solution, SSRN, **2024**.

141. Sharrouf M., Awad R. and Habanjar K., Alteration of magnetic behavior of $(Mg_{0.9}Ni_{0.1}O)_x/(CoFe_2O_4)_{1-x}$ nanocomposites, J. Nanopart. Res., 26, **2024,** 96.

142. Bremer M., Fischer S. Langbein H. Topelmann W. and Scheler H., Investigation on the formation of manganese zinc ferrites by thermal decomposition of solid solution oxalates, Thermochim. Acta., 209, **1992**, 323-330.

143. Byrappa K. and Adschiri T., Hydrothermal technology for nanotechnology, Prog. Cryst. Growth Charact. Mater., 53(2), **2007**, 117-166.

144. Kharisov B.I., Dias H.V.R. and Kharissova O.V., Mini-review: ferrite nanoparticles in the catalysis, Arab. J. Chem., 12(7), **2019,** 1234-1246.

145. Casbeer E., Sharma V.K. and Li X.Z., Synthesis and photocatalytic activity of ferrites under visible light: a review, Sep. Purif. Technol., 87, **2012**, 1-14.

146. Bhatnagar A. and Sillanpaa M., Utilization of agro-industrial and municipal waste materials as potential adsorbents for water treatment—a review, Chem. Eng. J., 157(2-3), **2010**, 277-296.

147. Shaikj S.F., Ubaidullah M., Mane R.S. and Al-Enizi A.M., Types, Synthesis methods and applications of ferrites, Spinel Ferrite Nanostructures for Energy Storage Devices, **2020**, 51-82.

148. Shirsath S.E., Wang D., Jadhav S.S., Mane M.L. and Li S., Ferrites obtained by sol-gel method, Handbook of sol-gel science and technology, **2018**.

149. Zhang L. and Wu Y., Sol-Gel synthesized magnetic $MnFe_2O_4$ spinel ferrite nanoparticles as novel catalyst for oxidative degradation of methyl orange, J. Nanomater., 1, **2013**, 1-6.

150. Gomez C.A.P., Meneses C.A.B. and Matute A., Structural parameters and cation distributions in solid state synthesized Ni-Zn ferrites, Mater. Sci. Eng. B, 236–237, **2018**, 48-55.

151. Kumar G.P., Raghavendra V. and Babu C.H.P., Synthesis, structural studies on Ni-Zn ferrite by solid state reaction method, Chem. Sci. Trans., 5(4), **2016**.

152. Sharma P., Diwan P.K. and Pandey O.P., Impact of environment on the kinetics involved in the solid-state synthesis of bismuth ferrite, Mater. Chem. Phys., 233, **2019**, 171-179.

153. Rajasulochana P. and Preethy V., Comparison on Efficiency of Various Techniques in Treatment of Waste and Sewage Water – a Comprehensive Review, Resour.-Effic. Technol., 2(4), **2016**, 175-184.

154. Mohapatra M., and Anand S., Synthesis and applications of nano-structured iron oxides/hydroxides–a review, Int. Engin. Sci. Technol., 2(8), **2010**, 127-146.

155. Lazarevic Z.Z., Jovalekic C., Milutinovic A., Romcevic M.J., and Romcevic N.Z., Preparation and characterization of nano ferrites, Acta Phys. Pol. A, 121(3), **2012**, 682-686.

156. Faraji M., Yamini Y., and Rezaee M., Magnetic nanoparticles: synthesis, stabilization, functionalization, characterization, and applications, J. Iran. Chem. Soc., 7(1), **2010,** 1-37.

157. Vinnik D.A., Gudkova S.A., Zhivulin V.E. and Trofimov E.A., Ferrite-based solid solutions: structure types, preparation, properties, and potential applications, Inorg. Mater., 57, **2021**, 1109-1118.

Chapter 3:

MATERIALS AND METHODS

3.1 Materials and reagents required

The aluminium-doped mixed transition metal ferrites $Al_xM_{0.7}Mn_{0.3}Fe_{2-x}O_4$ (x = 0.1,0.3, 0.5, 0.7, 0.9 and M= Co, Ni, Cu, and Zn) were synthesized using the solution combustion method. All the materials and reagents used for the synthesis of ferrites are of the Analytical grade: aluminium sulphate octadecahydrate $\{Al_2(SO_4)_3 \cdot 18H_2O\}$, cobalt nitrate hexahydrate $\{Co(NO_3)_2 \cdot 6H_2O\}$, nickel nitrate hexahydrate $\{Ni(NO_3)_2 \cdot 6H_2O\}$, copper nitrate trihydrate $\{Cu(NO_3)_2 \cdot 6H_2O\}$, zinc nitrate hexahydrate $\{Zn(NO_3)_2 \cdot 6H_2O\}$, manganese nitrate tetrahydrate $\{Mn(NO_3)_2.4H_2O\}$, ferric nitrate nonahydrate $\{Fe(NO_3)_3 \cdot 9H_2O\}$, hydrazine hydrate ($N_2H_4.H_2O$), diethyl Oxalate $(COOCH_2CH_3)_2$, methylene blue ($C_{16}H_{18}ClN_3S$), crystal violet ($C_{25}N_3H_3OCl$), methyl orange ($C_{14}H_{14}N_3NaO_3S$) and congo red ($C_{32}H_{22}N_6Na_2O_6S_2$).

3.2 Experimental methods

3.2.1 Synthesis of oxalyldihydrazide

The compound oxalyldihydrazide (ODH) is known for its notable gas production and strong reducing capabilities. A specific procedure was followed for the synthesis of ODH, which was employed as a fuel for this solution combustion synthesis. In this reaction two moles of hydrazine hydrate were gradually mixed with one mole of diethyl oxalate in small amounts. This addition was carried out dropwise, while maintaining the reaction mixture at a temperature of 4°C using an ice bath. This precaution was necessary because the reaction is highly exothermic, generating considerable heat. Due to the extreme heat generated, the reaction mixture had to be continuously cooled in the ice bath to prevent uncontrolled reactions or hazardous situations. Upon the completion of the reaction, white-coloured precipitates identified as ODH, were formed. These precipitates were then carefully dried using a water bath heated to a specific temperature range of 70-78°C.

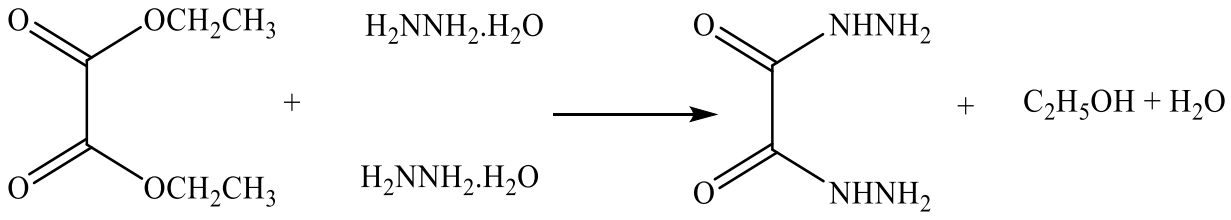

Figure 3.1: Schematic illustration for synthesis of oxalyldihydrazide.

3.2.2 Preparation of $Al_xM_{0.7}Mn_{0.3}Fe_{2-x}O_4$ (M = Co, Ni, Cu, Zn)

The synthesis process for Al-doped transition metal ferrites, denoted by the formula $Al_xM_{0.7}Mn_{0.3}Fe_{2-x}O_4$ (where x = 0.1, 0.3, 0.5, 0.7, and 0.9; M = Co, Ni, Cu, and Zn), involved several sequential steps. Firstly, stoichiometric quantities of the respective metal salts were taken in minimum amount of water and mixed afterwards. Oxalyldihydrazide (ODH) was slowly added into this mixture, while maintaining continuous stirring to ensure uniform mixing. Subsequently, this mixture was concentrated on a water bath held at a controlled temperature of 70-72°C for 2 hours. This step lowered the content of water in the mixture, concentrating the reactants and facilitating the subsequent heat treatment. The concentrated mixture was then gradually heated, with a heating rate of 5^0C per minute, in a muffle furnace with a stepwise increase in temperature up to 650°C. This gradual temperature increase was crucial to prevent sudden thermal shocks that could affect the reaction and product formation. Finally, brown coloured powder product was obtained. This powder represented the doped transition metal ferrite at the specified concentrations. The synthesis process was repeated for the other designated concentrations of Al-doped mixed transition metal ferrites, ensuring that the steps of concentration, mixing, and thermal treatment were followed consistently when preparing the different compositions.

Figure 3.2: Schematic illustration of preparation of Al-doped mixed transition metal ferrite.

3.3 Characterization of Al-doped mixed transition metal ferrites

The characterization of the surface and morphological behavior of Al-doped mixed transition metal ferrites involved the use of various techniques to understand the physical and structural properties of these materials at a microscopic and macroscopic level. Several analytical methods and instruments were employed in this characterization process including FTIR, SEM, XRD, BET, and VSM. These techniques were effectively used to comprehensively understand the surface morphology, structural composition, crystallographic nature, elemental composition, physical and chemical properties, and specific surface area of the Al-doped mixed transition metal ferrites. This detailed characterization is crucial for evaluating the suitability of these materials for specific applications in various fields. FTIR analysis was conducted by emplying Perkin Elmer spectrum 2 spectrometer, which was aimed to identify the presence of metal-oxygen bonds and arrangement of various ions between different sites. XRD analysis was carried out by using Bruker D8 Advance, employing CuKα radiation, with a wavelength of 1.542 Angstroms, to estimate the crystallite size and phase purity. FESEM (JEOL JSM-7610F plus EDS) instrument was employed to observe surface morphology and element composition. Magnetic properties of ferrite samples were assessed using VSM (Microisense EZ9iVSM, USA) in the +20 kOe to -20 kOe range at ambient temperature. Additionally, the pore radius, pore volume and specific surface area were analyzed by using BET (Autosorb-1(iQ)). A UV-visible spectrophotometer was employed to study adsorption properties for ferrites for various dyes in aqueous solutions. Absorbance was measured in the 200 to 800 nm range using UV-1900i (Shimadzu Corp.81798) spectrophotometer.

3.3.1 Fourier transform infrared (FTIR) analysis

The identification of Al-doped mixed transition metal ferrites involved the use of FTIR spectrometer, operating within the 4000-400 cm^{-1} range. FTIR spectroscopy is based on the principle that various inorganic and organic molecules exhibit characteristic absorption patterns of Infrared wavelengths in the electromagnetic spectrum. Certain wavelengths of infrared light are absorbed by the molecular bonds, generating a spectrum, and the absorbance peaks at specific wavelengths (expressed as wave numbers in cm^{-1}) correspond to the vibrations of different chemical bonds present in the molecules. The frequency range examined in FTIR spectroscopy, typically from 4000 to 400 cm^{-1}, corresponds to different types of molecular vibrations, such as stretching and bending of chemical bonds. By analyzing this spectral range, it is possible to identify and study specific functional groups within the Al-doped mixed

transition metal ferrites. Distinct peaks observed within the specified range in the FTIR spectrum correspond to different metal-oxygen bonds present in the ferrites. Identification and analysis of absorption bands provide valuable information about metal-oxygen bonds present in the material. This data aids in understanding the bonding, surface chemistry and composition of the Al-doped mixed transition metal ferrites, which is important for comprehending their properties for possible applications in different fields.

3.3.2 X-ray powder diffraction (XRD) analysis

This technique is used to determine the crystallite size and crystalline structure of materials. Monochromatic X-rays interfere constructively to produce X-ray radiation. A cathode ray tube produces these X-rays, which are then utilized to filter, collect, and direct the radiation toward the sample to create monochromatic radiation. The XRD analysis of Al-doped mixed transition metal ferrites were investigated using an X-ray powder diffractometer. Using the Debye–Scherrer Equation (1), the crystallite size of aluminium-doped mixed transition metal ferrite was determined from the strongest and sharpest peak (311) of the X-ray diffraction patterns [1].

$$D_{(hkl)} = \frac{K\lambda}{\beta cos\theta} \qquad (1)$$

The values of D, β, K, θ and λ represent the mean crystallite size (nm), line broadening at half maximum intensity (rad), a dimensionless form factor, Bragg's diffraction angle (rad) and

X-ray wavelength (nm) respectively.

3.3.3 Field emission scanning electron microscope (FESEM)

This technique is a powerful tool used to capture highly detailed images of surfaces, particularly at the nanoscale level. It employs electron beams to scan and visualize the topography of materials, providing remarkably high-resolution images that offer a three-dimensional perspective of the surface features. FESEM plays a pivotal role in examining the surface morphology. Ferrites due to their incredibly small size, often possess unique and complex surface structures that can greatly impact their properties and behavior. FESEM imaging allows to explore these surface characteristics with precision, revealing intricate details of nanoparticles arrangements, shapes, sizes, and the distribution of particles across the surface.

3.3.4 Vibrating sample magnetometer (VSM)

The VSM is a valuable instrument for comprehending and quantifying essential magnetic properties, offering critical insights for various technological applications and material advancements. It is a crucial tool employed in identifying and measuring magnetic characteristics in materials, notably properties such coercivity (H_c), saturation magnetization (M_s), and remanent magnetization (M_r). Coercivity is an essential characteristic that shows a ferromagnetic material's capacity to deal with an external magnetic field without losing its magnetism. Ferromagnetic materials exhibiting high coercivity are labelled as 'hard,' while those with low coercivity are labelled as 'soft.' Soft ferrites have extensive applications in components like transformer cores, inductors, and devices operating in the microwave spectrum. Remanent magnetization denotes the residual magnetic value retained by a ferromagnetic substance even after the induced magnetic field has been eliminated. On the application of applied magnetic field, when the magnetic moment vectors of all constituent particles or domains within a material align perfectly, the state achieved is known as saturation magnetization. This condition signifies that the material has reached its maximum magnetization. In this state, magnetic domains or atomic moments are fully aligned, resulting in the highest possible magnetic strength for that specific material. The experimental magnetic moment (μ_B), thus obtained through equation (2), serves as a crucial parameter in characterizing the material's magnetic properties and behavior, contributing significantly to the study and application of magnetic materials in several scientific and technological domains [2]. Here M_w, M_s are molecular weight and saturation magnetization respectively, and value 5585 corresponds to magnetic factor.

$$\mu_B = M_w M_s / 5585 \qquad (2)$$

The anisotropy constant (K) is a critical parameter used to describe the energy associated with the preferred direction of magnetization within a material. It signifies the material's tendency to align its magnetic moments in a particular direction. The evaluation of this constant, K, is essential for understanding how a material responds to an external magnetic field and how it retains its magnetic properties.

$$H_c = 0.96K / M_s \qquad (3)$$

3.3.5 Brunauer-Emmett-Teller (BET) analysis

The BET method was utilized to observe crucial characteristics such as pore volume, specific surface area and pore size distribution of the Al-doped mixed transition metal ferrites. This method is fundamental for evaluating the surface properties and porosity of materials by employing the physical adsorption of gas molecules onto a solid surface. The BET theory, formulated by Brunauer, Emmett, and Teller, provides the theoretical foundation for measuring a material's specific surface area. It involves adsorption of gas particles onto the material surface at various pressures and temperatures. The amount of gas adsorbed at different pressures is used to determine surface area, providing insights into the material's porosity and surface characteristics. In this case, the Al-doped mixed transition metal ferrites were analyzed using the BET method with the Autosorb-1(iQ) instrument. This equipment is specifically designed for porosity and surface area analysis. This information is vital for understanding the material's performance and suitability for various applications, such as catalysis, adsorption, or other surface-dependent processes.

3.4 Batch adsorption studies

This study investigates the potential of as-synthesized Al-doped mixed transition metal ferrites as an adsorbent for removing dyes, methylene blue (MB), crystal violet (CV), congo red (CR), and methyl orange (MO), from their aqueous solutions. In adsorption studies, the dyes (MO, CR, CV, and MB) ppm solutions were prepared by dissolving different grams of dye powder in distilled water and employing it as a pollutant in a batch adsorption experiment. The experiment was conducted by using a 250 ml of Erlenmeyer flask and the orbital shaker with flask shaking speed at 110 rpm for a predetermined time interval. The samples were then removed from orbital shaker and ferrites were separated by using a bar magnet. Remaining solutions were then employed for residual concentration measurements. At adsorption equilibrium, the remaining dye concentration was measured with UV-Vis spectrophotometer. Equations (4), (5), and (6) were used to calculate percentage removal efficiency [3].

$$\text{Removal } (\%) = \frac{(C_0 - C_e)}{C_0} \times 100 \tag{4}$$

$$q_e = \frac{(C_0 - C_e)V}{m} \tag{5}$$

$$q_t = \frac{(C_0 - C_t)V}{m} \qquad (6)$$

Here q_t refers to amount of dye uptake at given time 't' (mg/g) and q_e refers to the amount of dye at equilibrium condition (mg/g). The initial (mg/L), equilibrium (mg/L), and time t (mg/L) adsorbate concentrations are represented by the symbols C_o, C_e, and C_t, respectively.

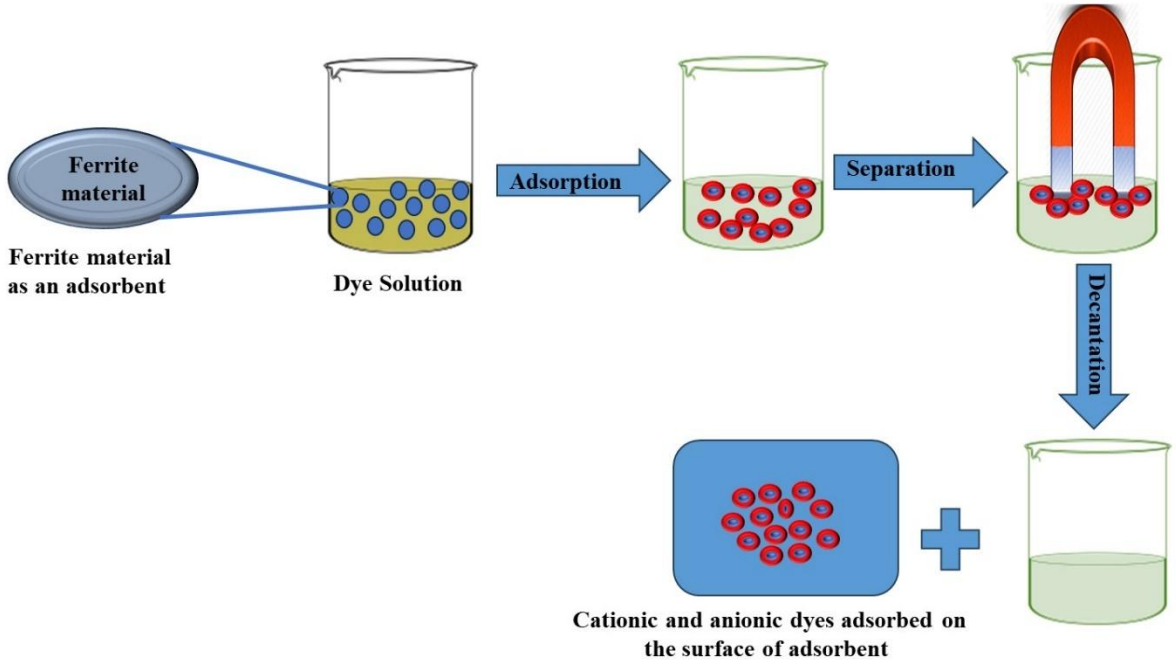

Figure 3.3: Schematic illustration for dye adsorption by using of Al-doped mixed transition metal ferrite.

3.4.1 Adsorption thermodynamics

Adsorption thermodynamics explores the energy changes that occur during the adsorption process. The primary aim is to understand the energetic aspects of the adsorption process by using several thermodynamic parameters, which help to characterize and evaluate adsorption phenomenon. Three fundamental thermodynamic parameters are typically employed in the analysis of adsorption processes: enthalpy of adsorption (ΔH^o), entropy of adsorption (ΔS^o), and Gibbs free energy change (ΔG^o), which are calculated by using various thermodynamic equations, referenced as [4, 5]. Equations (7-10) provide a mathematical framework for calculating and analyzing the nature of the adsorption process based on the aforementioned thermodynamic parameters. The Van't Hoff equation is one of the essential equations used in this context. It allows for the determination of the equilibrium constant (K_d) and Gibbs free

energy change (ΔG^o) associated with the adsorption process. This equation provides insights into whether the adsorption is non-spontaneous or spontaneous, and the extent to which the system tends to reach equilibrium. Mathematically, the Van't Hoff equation (equation 10) gives the relation between equilibrium constant (K_d) and temperature through the Gibbs free energy change (ΔG), enabling researchers to assess the temperature dependence of the adsorption equilibrium and gain a deeper comprehension of the process of adsorption based on thermodynamic considerations [6].

$$\Delta G^o = -RT \ln K_d \qquad (7)$$

The general equation to calculate the adsorption equilibrium constant is represented as [7].

$$K_d = \frac{(C_0 - C_e)}{C_0} \qquad (8)$$

For the adsorption process, the entropy (ΔS^o) and enthalpy (ΔH^o) values were determined using Gibb's Helmholtz equation: (8).

$$\Delta G^o = \Delta H^o - T\Delta S^o \qquad (9)$$

Equating (7) and (9), we get,

$$\ln k_d = \frac{\Delta S^O}{R} - \frac{\Delta H^O}{RT} \qquad (10)$$

here K_d is distribution equilibrium constant and T is the absolute temperature. The adsorption thermodynamic parameters are calculated from a slope and intercept of linear plot between ln K and 1/T.

3.4.2 Adsorption isotherms

Different adsorption isotherms are essential tools for exploring and comprehending the adsorption characteristics of an adsorbent material. These isotherms are instrumental in representing the equilibrium achieved during the adsorption process within a system. Among the array of available isotherms, several are commonly employed to determine and explain the adsorption mechanisms. The Dubinin-Radushkevich, Langmuir, Temkin and Freundlich isotherms are widely used to understand the nature of adsorption. Each of these isotherms offers a distinct approach or model to describe and interpret the adsorption behavior of the adsorbent material under specific conditions. By applying these isotherms, researchers gain valuable insights into the adsorption process, allowing them to assess the

interaction of the adsorbent and adsorbate, and derive parameters that help characterize the adsorption equilibrium comprehensively [8-11].

3.4.2.1 Dubinin-Radushkevich (D-R) isotherm

The D-R Isotherm, referenced in [8], operates under the assumption that, at relatively low pressures (expressed as P/Ps), the thermodynamic potential correlates to the quantity of vapor adsorbed by the adsorbent material. This isotherm model is particularly focused on describing adsorption phenomena under these specific conditions of low-pressure. The adsorption process depends on the adsorbate's interaction with the adsorbent surface at lower-pressure, indicating a relationship between the thermodynamic potential and the adsorbate molecules captured by the material. In essence, the D-R Isotherm provides a theoretical framework for understanding how adsorbate molecules adhere to the surface of the adsorbent at low pressures, highlighting the significance of this interaction in the overall adsorption process.

$$A = RT \ln \frac{P}{P_s} \qquad (11)$$

Here, 'A' is differential molar work (kJ/mol), 'P_s' is the temperature-saturated pressure and 'P' is adsorbate partial pressure.

The D-R isotherm can be stated linearly as

$$\ln Q_e = lnQ_m - \beta\varepsilon^2 \qquad (12)$$

Q_e, Q_m, β and Ɛ are adsorption capacity, maximum quantity of adsorption, isotherm constant and adsorption potential respectively.

3.4.2.2 Langmuir adsorption isotherm

This isotherm is an essential model that explains the link between the quantity of adsorbate adsorbed onto the surface and the concentration or partial pressure of the adsorbate in the surrounding environment. According to this model, the adsorption process follows a specific pattern: initially, a monolayer is formed onto uniform and homogenous adsorbent surface. This monolayer signifies the maximum adsorption capacity under the prevailing conditions. The key principle of the Langmuir model is that once this monolayer is formed, no further adsorption occurs. In other words, at equilibrium, where the adsorption and desorption rates are balanced, no additional adsorbate molecules can attach to the already occupied sites. This assumption implies that the adsorption process reaches a saturation point, beyond which no more adsorption takes place. This theoretical framework of the Langmuir adsorption isotherm offers

a simplified representation of adsorption phenomena on surfaces with uniform sites available. The Langmuir equation mathematically describes this model, facilitating a better understanding of adsorption behavior under specific conditions [8].

$$\frac{1}{\mathrm{Qe}} = \frac{1}{Q} + \frac{1}{bQC_e} \qquad (13)$$

Where Q_e is the amount of adsorbate, Q is the capacity for adsorption in mg/g, C_e is the dye's equilibrium concentration and 'b' is the adsorption energy.

3.4.2.3 Freundlich isotherm

The Freundlich isotherm model suggests a heterogeneous surface having different adsorption sites with varying adsorption potentials. In the context of the Freundlich isotherm, each site on the adsorbent's surface exhibits unique properties, implying that the adsorption process is not limited to uniform sites or a single layer. Instead, the adsorbent surface is composed of diverse sites with different affinities for adsorbate molecules. With increase in solute concentration in the liquid phase, the adsorption onto the surface also intensifies, though at a diminishing rate. The Freundlich equation reflects this relationship mathematically, which is applicable to heterogeneous surfaces, indicating that the ability of an adsorbent to absorb nonlinearly with changes in the concentration of the solute in the liquid phase. This model is valuable for understanding adsorption phenomena on surfaces with a wide range of adsorption sites and provides insights into the behavior of adsorbent materials [8].

$$\log Q_e = \log \mathrm{K_f} + \frac{1}{\mathrm{n}} \log \mathrm{C_e} \qquad (14)$$

Here 'K_f' and 'n' indicate the non-linearity/linearity between the adsorption rates and the material's solution concentration.

3.4.2.4 Temkin isotherm

The connection between the heat of adsorption and the surface coverage of an adsorbate on the adsorbent is described by the Temkin adsorption isotherm. In this isotherm, it is suggested that the heat of sorption, which refers to the energy released or absorbed when an adsorbate molecule adheres to the surface of the adsorbent, experiences a linear reduction with increasing coverage of the surface by the adsorbate molecules. This reduction occurs because of the evolving relationship between the adsorbate and adsorbent surface as more sites become occupied by the adsorbate molecules. According to the Temkin model, the heat of adsorption should drop linearly as the adsorbate molecules build up on the surface of adsorbent and the

adsorbent-adsorbate interaction progressively changes. This decline in the heat of adsorption signifies that the adsorption process becomes less energetically favourable as more surface sites become covered by adsorbate molecules. Mathematically, the Temkin isotherm equation represents this relationship between the surface coverage and heat of adsorption, providing a way to quantitatively describe how the heat of adsorption diminishes linearly with the increasing coverage of the adsorbent surface by adsorbate molecules. This model aids in understanding the energetics and contributes to characterizing the interactions between the adsorbent and adsorbate under varying surface coverages [8].

The formula for the Temkin adsorption isotherm is:

$$Q_e = \frac{RT}{b} \ln A + \frac{RT}{b} \ln C_e \qquad (15)$$

Here b is Temkin constant and A is maximum binding energy.

3.4.3 Models of empirical adsorption kinetics

Adsorption behavior is time-dependent, and studying the adsorption kinetics is important for examining the nature of adsorption. Adsorption kinetic behavior of selected dye was explored by employing Lagergren pseudo-first-order (PFO) and Lagergren pseudo-second-order (PSO) kinetic models. The influence of contact time was ascertained by fitting these kinetic models to the data obtained from adsorption experiments, and the best-fit kinetic model was identified [11].

3.4.3.1 Pseudo-first-order (PFO) kinetics model

Derived from the chemical reaction model, the pseudo-first-order (PFO) model {Equation (16)} proposed by Lagergren in 1898 is one of the most widely used empirical adsorption kinetics models. A pseudo-first order reaction states that when one relative reactant is supplied in large excess, its concentration stays constant. The film diffusion is the rate-limiting step and the adsorption rate will vary inversely with film thickness, particle size, and distribution coefficient. The word "physisorption" (physical exchange) was created because the rate-limiting factor in this type of reaction is diffusion, rather than dependence on the concentration of both reactants. Results of fitting have been used to explore the physical interpretations of the PFO model.

$$\ln (q_e - q_t) = \ln q_e - k_1 t \qquad (16)$$

Here q_e and q_t are the quantities of pollutants adsorbed (mg/g) on the adsorbent at equilibrium and at time t, and k_1 is the rate constant for PFO kinetics (in minutes).

3.4.3.2 Pseudo-second-order (PSO) kinetics model

The best match between the results of experiments and chemical behavior is demonstrated by the pseudo-second-order (PSO), indicating its significance in the rate-controlling stage. The term "chemisorption" refers to the chemical rate-controlling mechanism of the process. In this mechanism, the sorption kinetics should be compatible with two opposing reversible second-order processes at larger ratios of adsorbate-to-adsorbent and a second-order reversible process at smaller ratios, which becomes first-order at very small ratios.

$$\frac{t}{q_t} = \frac{1}{k_2 q_e^2} + \frac{t}{q_e} \qquad (17)$$

In this case, q_e and q_t refer to the quantities of adsorbate per gram of adsorbent (mg/g) at equilibrium condition and at time t, and k_2 refers to the rate constant for PSO kinetics (mg/min).

References

1. Mahajan H., Kumar S., Sharma A., Mohammed I., Thakur M., Kaur A. and Srivastava A.K., Effect of sintering temperature on structural, morphological, magnetic, and electrochemical properties of $Mn_{0.3}Co_{0.2}Zn_{0.5}Fe_2O_4$ Ferrite, J Sol-Gel Sci. Technol., 105, **2023**, 388-404.
2. Mulud F.H., Dahham N.A. and Waheed I.F., Synthesis and characterization of copper ferrite nanopart IOP Conf. series: Mater. Sci. Eng., 928, **2020**, 072125.
3. Senol Z.M., Ertap H., Fermine Y. and El-Messaoudi N., Adsorptive removal of synthetic dye from its aqueous solution by using chitosan-bentonite composite: DFT and experimental studies, Polymer Bulletin, 81, **2024**, 12795-12817.
4. Saleh T.A., Kinetic models and thermodynamics of adsorption processes: classification, Interface Sci. Technol., 34, **2022**, 65-97.
5. Tran H.N., Lima E.C., Juang R.S., Bollinger J.C. and Chao H.P., Thermodynamic parameters of liquid–phase adsorption process calculated from different equilibrium constants related to adsorption isotherms: A comparison study, J. Environ. Chem. Eng., 9(6), **2021**, 106674.
6. Essebaai H., Ismi I., Lebkiri A., Marzak S., and Rifi E.H. Kinetic and Thermodynamic Study of Adsorption of Copper (II) Ion on Moroccan Clay, Mediterr. J. Chem., 9(2), **2019**, 102-115.
7. Kumar M., Dosanjh H.S. and Singh H., Magnetic zinc ferrite-alginic biopolymer composite:as an alternative adsorbent for the removal of dyes in single and ternary dye system, J. Inorg. Organomet. Polym. Mater., 28, **2018**, 1688-1705.
8. Nwabanne J.T., Adsorption and Kinetic Modeling of Heavy Metals Uptake from Waste Water Effluents, A Ph.D. Dissertation in Chemical Engineering Department, NnamdiAzikiwe University Awka, **2010**.
9. Abuh M.A., Akpomie G.K., Nwagbara N.K., Abia-Bassey N., Ape D. and Ayabie B.U., Kinetic rate equations application on the removal of copper (II) and zinc (II) by unmodified lignocellulosic fibrous layer of palm tree trunk-single component system studies, Int. J. Basic Appl. Sci., 1(4), **2013**, 800-809.
10. Ramachandran P., Vairamuthu R. and Ponnusamy S., Adsorption isotherms, kinetics, thermodynamics and desorption studies of reactive orange16 on activated carbon derived from ananascomosus (L) carbon, ARPN J. Eng. Appl. Sci., 6(11), **2011**, 15-26.

11. Tsibranska I. and Hristova E., Comparison of different kinetic models for adsorption of heavy metals onto activated carbon from apricot stones relation, Bulgarian Chem. Commun.,43(3), **2011**, 370-377.

CHAPTER 4:
RESULTS AND DISCUSSION

Based on the findings of initial investigations, Al-doped mixed transition metal ferrites were chosen for comprehensive adsorption experiments using various dyes. Consequently, the findings are examined in detail, with each section having subsections for characterization, adsorption, thermodynamic, and kinetic studies.

4.0. Adsorption of dyes with Al-doped mixed transition metal ferrite

Different adsorbents chosen for the dyes (CV, MO, CR, and MB) adsorption from aqueous solutions include Al-doped Co-Mn metal ferrite, Al-doped Ni-Mn metal ferrite, Al-doped Cu-Mn metal ferrite, and Al-doped Zn-Mn metal ferrite. The subsequent sections fully discuss the characterization and adsorption experiments on these specific metal ferrites using as-synthesized materials.

4.1. Al-doped Co-Mn ferrite

4.1.1 Fourier transform infrared spectroscopy (FTIR) analysis

FTIR spectra of various Al-doped mixed transition metal ferrites, with the wavenumber range from 4000 cm^{-1} to 400 cm^{-1}, is shown in figure 4.1. The inherent stretching vibrations of the oxygen bonds with cations from metals give rise to two distinctive absorption bands in the FTIR spectra of spinel ferrites. The metal-oxygen absorption band found in the region of 300-450 cm^{-1} corresponds to Fe^{3+}-O and Co^{2+}-O bonds (M_{oct}-O) [1], and in the region of 500-650 cm^{-1} corresponds to the Mn^{2+}-O bond (M_{tet}-O). Due to technological limitations of measurement instruments, the band associated with the 300-450 cm^{-1} range is not displayed. However, the stretching of the Al^{3+}-O bond can be seen at around ~1400–1100 cm^{-1} [2]. For a given metal ion, based on the mass and the strength of its interaction with oxygen, absorption occurs at varying frequencies. Despite inherent difficulties in identifying certain bonds within the observed spectra, the FTIR analysis of these ferrites gives important insights into their molecular structure, namely the bonding arrangements between oxygen atoms and metal cations.

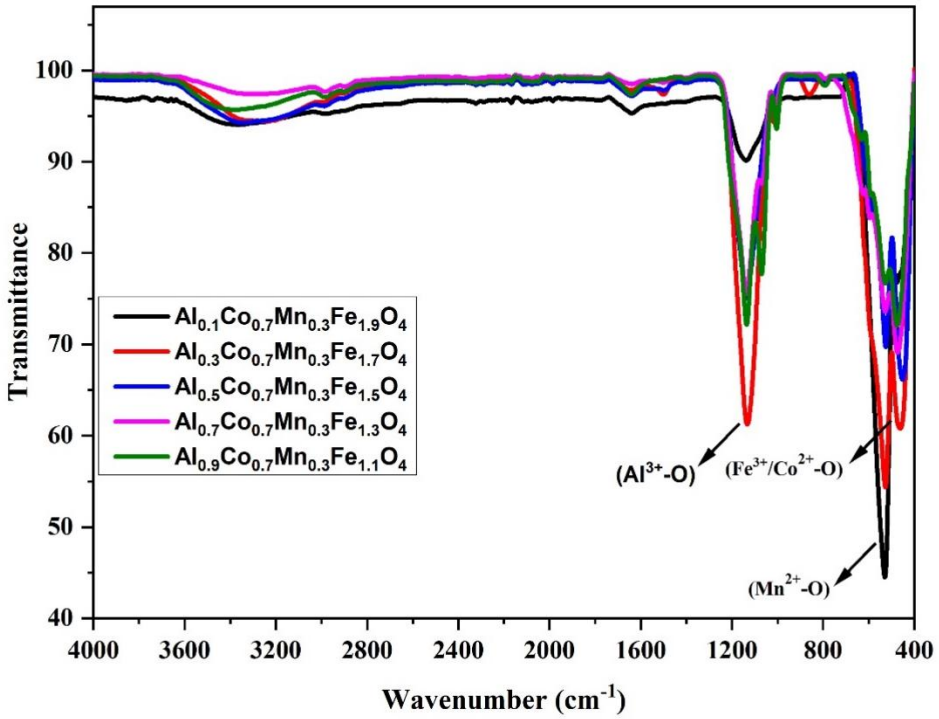

Figure 4.1: FTIR spectra of Al-doped Co-Mn mixed transition metal ferrites.

4.1.2 Powder X-ray diffraction (XRD) analysis

Figure 4.2 displays the XRD analysis of Al-doped mixed transition metal ferrite $Al_xCo_{0.7}Mn_{0.3}Fe_{2-x}O_4$ (where, x = 0.1, 0.3, 0.5, 0.7, and 0.9). The indicator peaks of Al-doped mixed transition metal ferrites demonstrate the single-phase characteristics of cubic spinel crystal structure having a Fd-3m space group at (111), (220), (300), (311), (400), (331), (422), (511), (440) with diffraction plane angles of 18.36°, 30.0°, 33.20°, 35.7°, 43.3°, 49.57°, 54.21°, 57.29° and 63.18° respectivfely. The nearly identical diffraction peaks of cobalt composite reveal that materials are crystalline and have high phase purity. The crystallite size 'D' of Al-doped mixed transition metal ferrite was calculated using Debye Scherrer equation (1) from the strongest and sharpest peak (311) of XRD pattern [3].

$$D_{(hkl)} = \frac{K\lambda}{\beta cos\theta} \qquad (1)$$

'K' is a dimensionless shape factor, '*D'* is the mean crystallite dimension (nm), 'λ' refers to the wavelength of X-ray (nm), 'β' is line broadening at half the maximum intensity (rad), and 'θ' is Bragg's diffraction angle (rad). The diffraction line broadens due to the strain and crystallite size contribution, as stated by Williamson and Hall (W-H). This methodology offers a more straightforward method that differentiates between strain- and size-induced broadening of peak

by computing the width of peak against function of 2θ. The strain-induced widening brought on by distortions and crystal imperfection was calculated using following formula.

$$\varepsilon = \frac{\beta}{4tan\theta} \qquad (2)$$

Equations (1) and (2) demonstrated that strain varies as tan θ and that the width of the peak varies as $\frac{1}{cos\theta}$. At this point, the material's strain and crystallite size contributions may be multiplied to describe the total peak broadening.

$$\beta_{(hkl)} = \beta_{(D)} + \beta_{(\varepsilon)} \qquad (3)$$

where $\beta_{(\varepsilon)}$ represents strain-induced widening, $\beta_{(D)}$ represents crystallite size, and $\beta_{(hkl)}$ represents the breadth of the half-maximum intensity. Table 4.1 illustrates how the size of the crystallites and the material's internal stress/strain affect the line width of the spectra. Two useful methods for calculating these effects are the Williamson-Hall analysis and the Scherrer equation. Broader peaks are produced by smaller crystallites, and strain produces broadening those changes with diffraction angle.

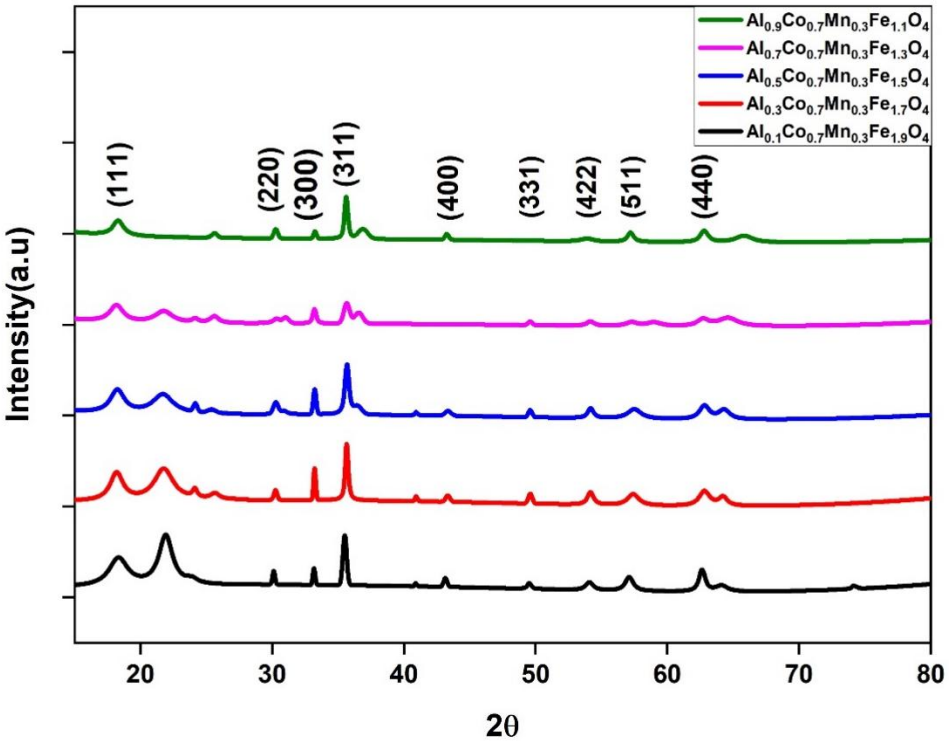

Figure 4.2: Powder XRD pattern of Al-doped Co-Mn mixed transition metal ferrites.

Table 4.1: Crystallite size and strain of Al-doped Co-Mn ferrite.

Ferrite ($Al_xCo_{0.7}Mn_{0.3}Fe_{2-x}O_4$)	D (nm)	$\delta \times 10^{-3}$ (nm^{-2})	$\in \times 10^{-3}$
X=0.1	1.506	440.63	68.07
X=0.3	2.868	121.53	35.68
X=0.5	4.532	48.68	22.53
X=0.7	5.589	32.00	18.34
X=0.9	8.393	14.19	12.21

4.1.3 Field emission scanning electron microscopy (FESEM) analysis

The surface morphology and fundamental physical properties of materials have been studied via FESEM, which is essential for understanding a substance's optimal particle shape distribution. Figure 4.3 (a) shows the ferrite sample's nano-granular structure. The elemental proportions of the EDS spectra, which are displayed in Figure 4.3(b), closely match the atomic percentage (at%) and weight percentage (wt%) of each element, namely O, Fe, Co, Al, and Mn.

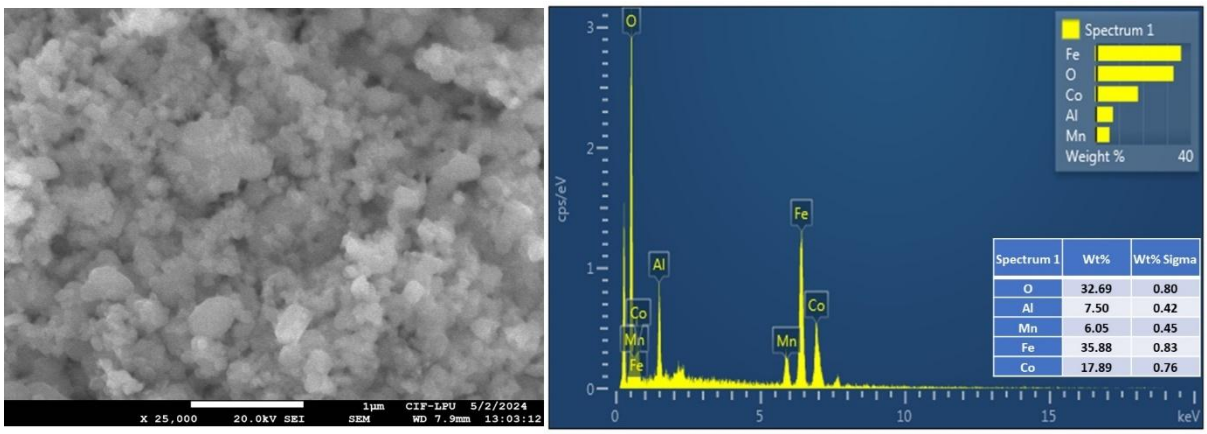

Figure 4.3: (a) SEM image (b) EDS image of Al-doped mixed transition metal ferrite ($Al_{0.5}Co_{0.7}Mn_{0.3}Fe_{1.5}O_4$).

4.1.4 Vibrating sample magnetometer (VSM) analysis

The hysteresis curves of Al-doped mixed transition metal ferrites, $Al_xCo_{0.7}Mn_{0.3}Fe_{2-x}O_4$, annealed at 650°C, are shown in figure 4.4. The analysis shows a soft superparamagnetic behavior in the as-synthesized samples. The net magnetization of the spinel lattice mostly determines the soft ferrite's saturation magnetization (M_s) value. Table 4.2 displays magnetic properties of these ferrite materials. For the $Al_xCo_{0.7}Mn_{0.3}Fe_{2-x}O_4$ ferrite, with varying value of

'x', the saturation magnetization (M_s) values were 39.04 , 13.86 , 14.64 , 9.77, and 12.92 emu/g respectively. The experimental magnetic moment (μ_B) was estimated as follows [4]

$$\mu_B = \frac{MmMs}{5585} \quad (4)$$

Using the following equation, the anisotropy constant (K) was determined [5]

$$H_c = \frac{0.96K}{Ms} \quad (5)$$

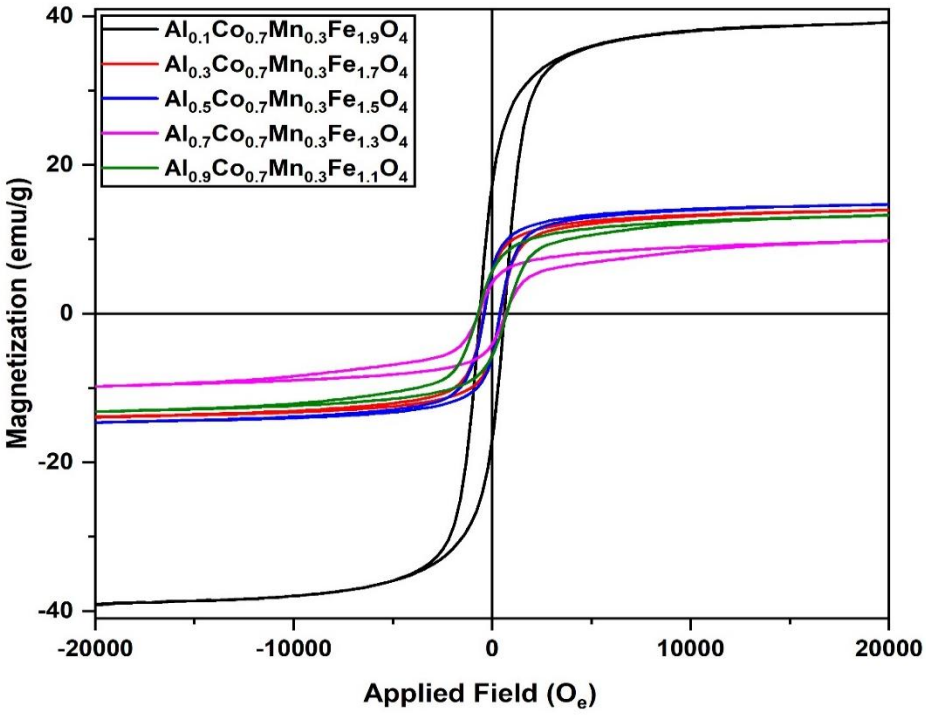

Figure 4.4: Hysteresis curves of $Al_xCo_{0.7}Mn_{0.3}Fe_{2-x}O_4$ ferrite at room temperature.

Table 4.2: Saturation magnetization (M_s), anisotropy constant (K), remanence (M_r), magnetic moment (μ_B), and coercivity (H_c) of $Al_xCo_{0.7}Mn_{0.3}Fe_{2-x}O_4$ ferrite annealed at 650°C for 5 hours.

Ferrite ($Al_xCo_{0.7}Mn_{0.3}Fe_{2-x}O_4$)	**M_S (emu.g^{-1})**	**M_r (emu.g^{-1})**	**H_c (O_e)**	**M_r/ M_S**	**μ_B**	**K×10^{-3} (emu.O_e g^{-1})**
X = 0.1	39.04	18.07	652.6	0.46	1.61	26.54
X = 0.3	13.86	5.76	558.0	0.41	0.56	8.06
X = 0.5	14.64	4.70	217.5	0.32	0.57	3.31
X = 0.7	9.77	3.97	671.5	0.40	0.37	6.83
X = 0.9	12.92	5.09	785.0	0.39	0.47	10.56

4.1.5 Brunauer-Emmett-Teller (BET) analysis

The Al-doped mixed transition metal ferrite's porosity and specific surface area were assessed using nitrogen adsorption-desorption techniques. (Figure 4.5). The surface area, pore volume and pore radius of Al-doped mixed transition metal ferrite are 12.779 m^2/g, 0.291 cc/g and 1542.53 Å respectively. The surface area has a significant impact on the observed activity trend.

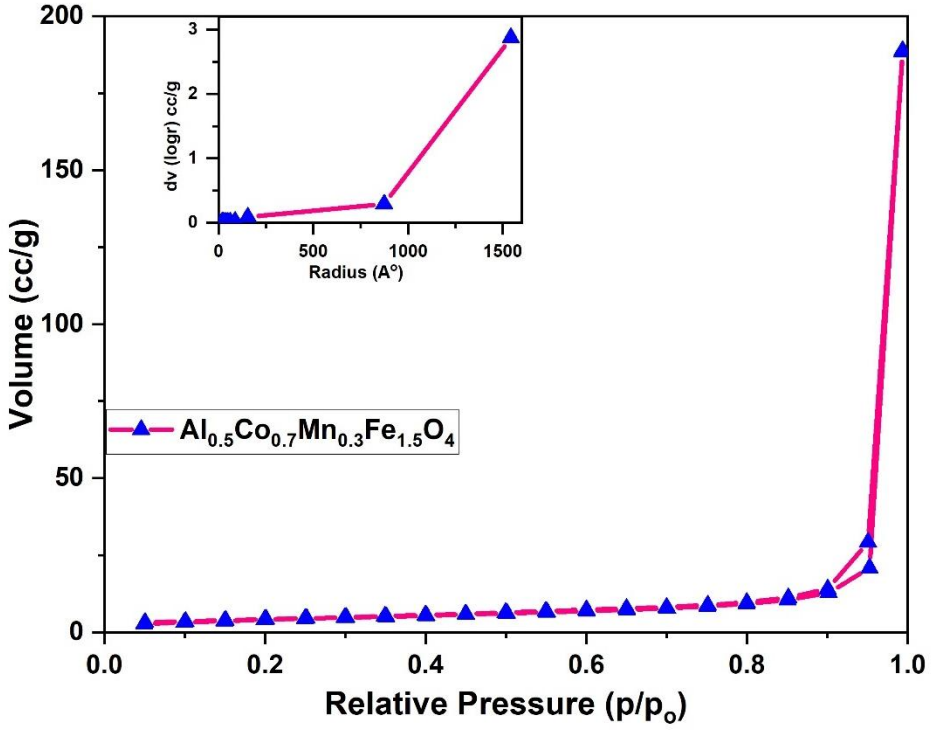

Figure 4.5: BET isotherm of $Al_{0.5}Co_{0.7}Mn_{0.3}Fe_{1.5}O_4$ ferrite.

4.1.6 Adsorption study of dyes with Al-doped Co-Mn ferrites

This study investigates the potential of using as-synthesized Al-doped mixed transition metal ferrites as an adsorbent for removing dyes from their aqueous solutions. The different concentration solutions of the dyes (CV, MO, CR, and MB) were prepared and employed as a pollutant in batch adsorption experiments. The experiment was carried out using a 250 ml Erlenmeyer flask, where the prepared solutions were put in the orbital shaker incubator and shaken at 110 rpm for one hour. Afterward, the ferrite samples were removed and separated using a bar magnet. After ferrite separation, residual (CR, CV, MO, MB,) concentration measurements were performed. The amount of leftover dye at adsorption equilibrium was calculated by using the UV-visible spectrophotometer. Equations (6), (7), and (8) were used to calculate the effectiveness in dye removal (%), Here q_e and q_t are dye quantity adsorbed at equilibrium and at time t in mg/g respectively [6].

$$\text{Removal}\ (\%) = \frac{(C_0 - C_e)}{C_0} \times 100 \tag{6}$$

$$q_e = \frac{(C_0 - C_e)V}{m} \tag{7}$$

$$q_t = \frac{(C_0 - C_t)V}{m} \tag{8}$$

Where C_o refers to initial adsorbate concentrations (in mg/L), C_e refers to equilibrium adsorbate concentrations (in mg/L), C_t refers to time t adsorbate concentrations (in mg/L). 'V' and 'm' stand for the sample's volume in liters and mass of adsorbent in grams respectively.

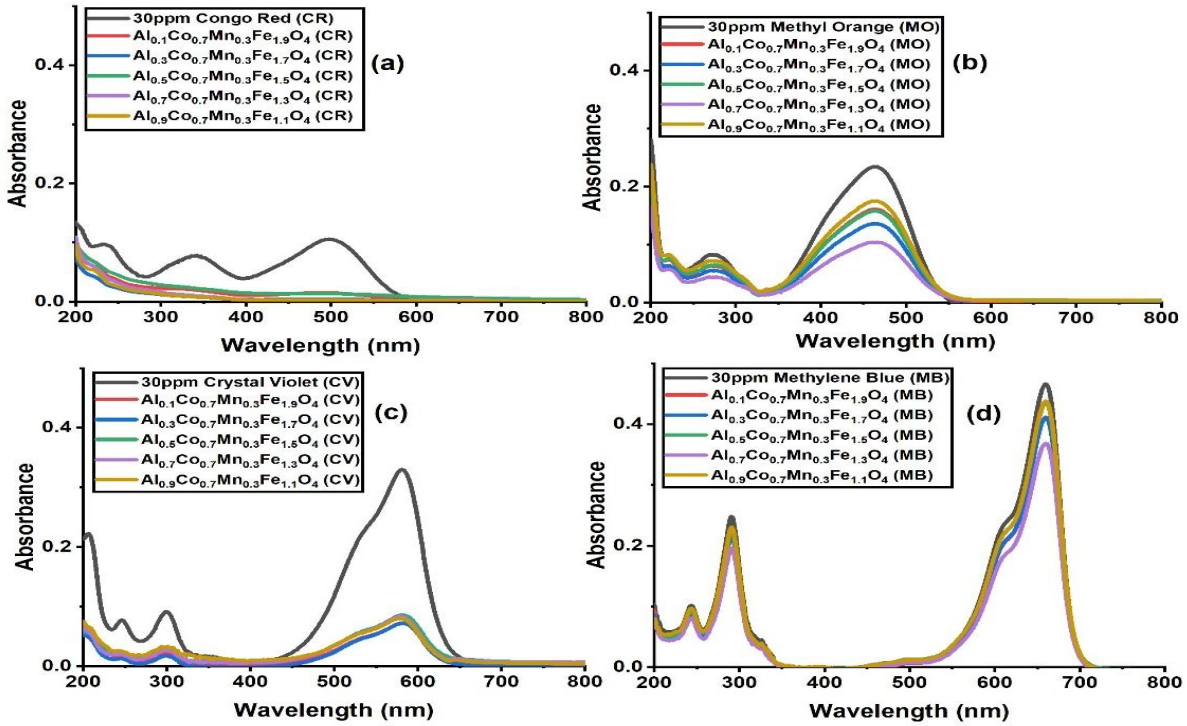

Figure 4.6: UV-visible absorption spectra for 30 ppm dyes solutions.

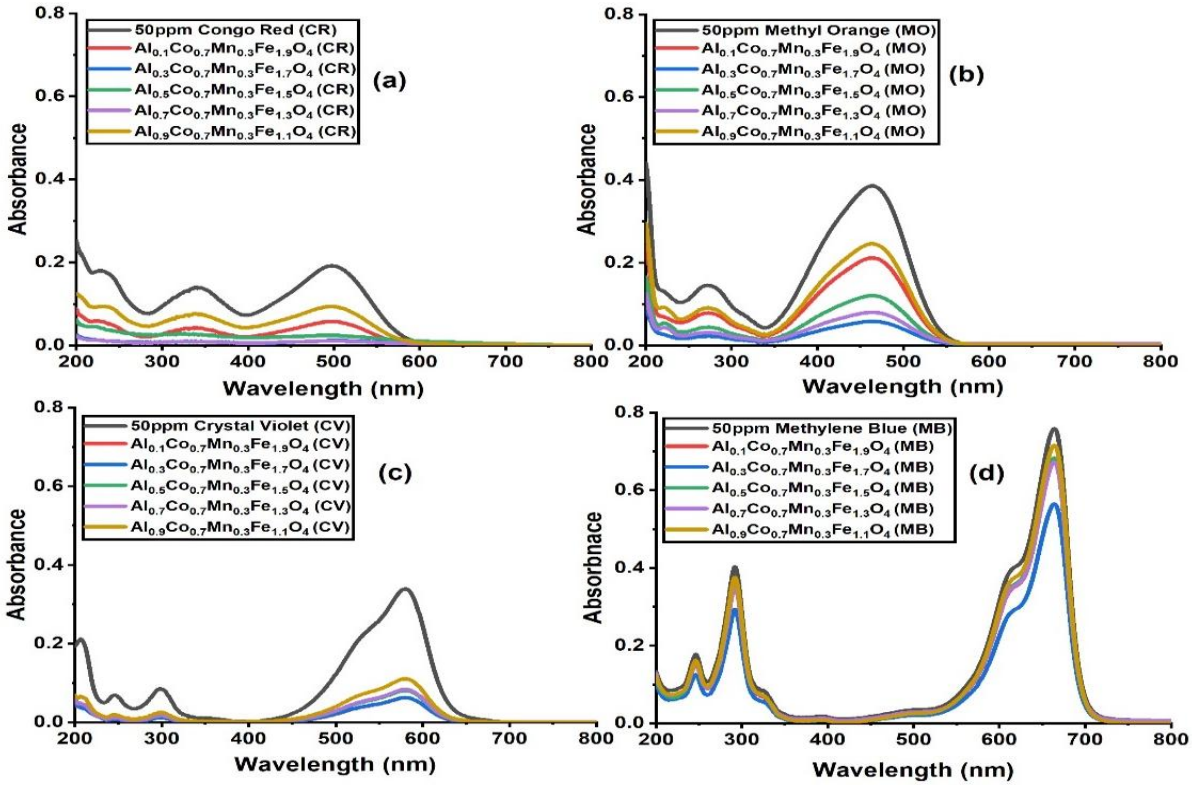

Figure 4.7: UV-visible absorption spectra for 50 ppm dyes solutions.

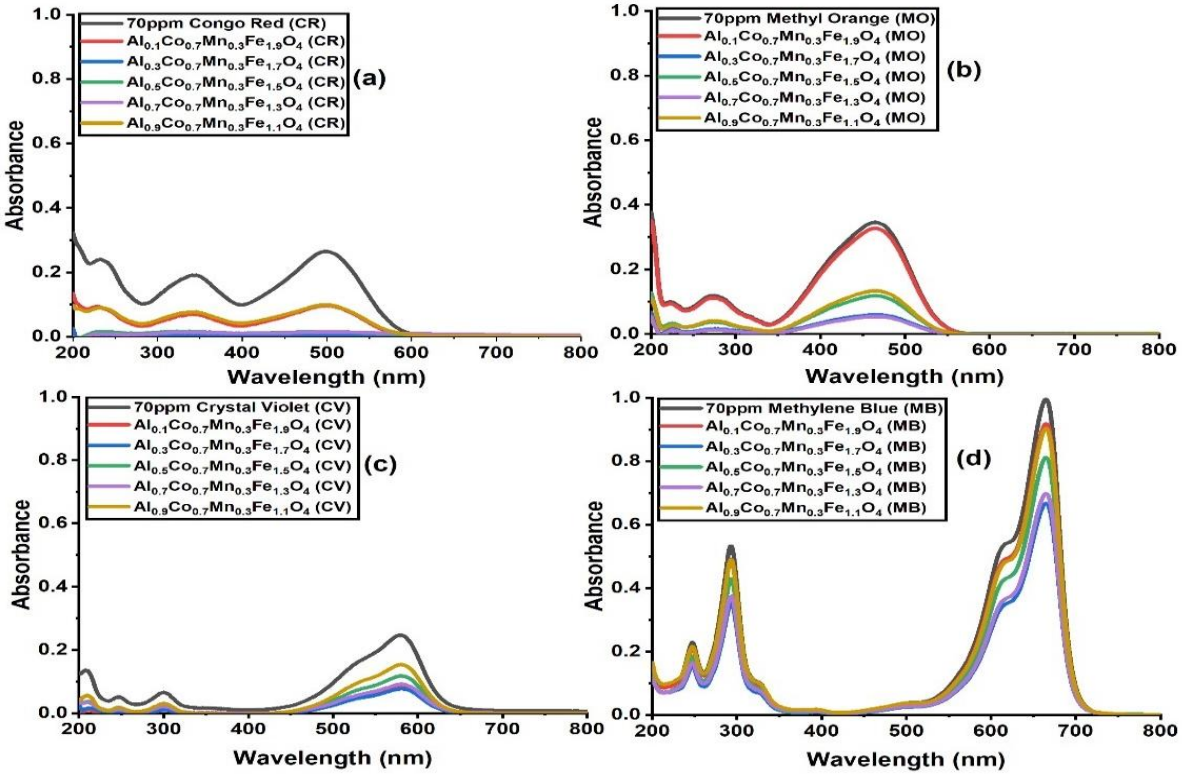

Figure 4.8: UV-visible absorption spectra for 70 ppm dyes solutions.

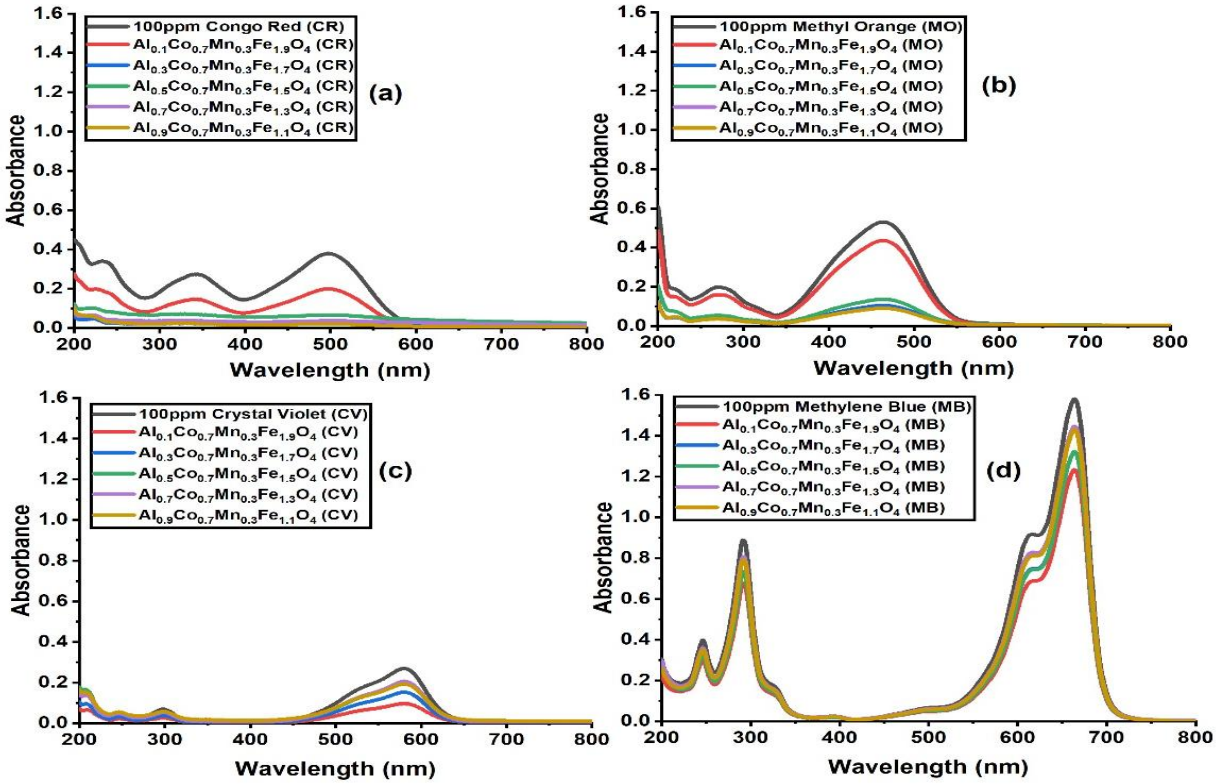

Figure 4.9: UV-visible absorption spectra for 100 ppm dyes solutions.

Table 4.3: Percentage removal of various dye concentrations using Al-doped Co-Mn ferrites.

CONGO RED (CR)				
Adsorbent	**% removal of CR (30ppm)**	**% removal of CR (50ppm)**	**% removal of CR (70ppm)**	**% removal of CR (100ppm)**
$Al_{0.1}Co_{0.7}Mn_{0.3}Fe_{1.9}O_4$	94.75	84.30	68.58	45.42
$Al_{0.3}Co_{0.7}Mn_{0.3}Fe_{1.7}O_4$	98.48	95.28	96.57	96.77
$Al_{0.5}Co_{0.7}Mn_{0.3}Fe_{1.5}O_4$	95.27	94.69	93.69	88.42
$Al_{0.7}Co_{0.7}Mn_{0.3}Fe_{1.3}O_4$	98.83	98.23	96.83	92.87
$Al_{0.9}Co_{0.7}Mn_{0.3}Fe_{1.1}O_4$	99.06	98.74	98.45	96.75
CRYSTAL VIOLET(CV)				
Adsorbent	**% removal of CV 30PPM**	**% removal of CV 50PPM**	**% removal of CV 70PPM**	**% removal of CV 100PPM**
$Al_{0.1}Co_{0.7}Mn_{0.3}Fe_{1.9}O_4$	91.06	76.76	76.95	77.98
$Al_{0.3}Co_{0.7}Mn_{0.3}Fe_{1.7}O_4$	51.57	49.26	40.31	37.53
$Al_{0.5}Co_{0.7}Mn_{0.3}Fe_{1.5}O_4$	57.54	56.26	51.71	58.00
$Al_{0.7}Co_{0.7}Mn_{0.3}Fe_{1.3}O_4$	50.06	47.94	44.98	35.44
$Al_{0.9}Co_{0.7}Mn_{0.3}Fe_{1.1}O_4$	54.46	46.34	39.56	33.87
METHYL ORANGE (MO)				

Adsorbent	% removal of MO (30ppm)	% removal of MO (50ppm)	% removal of MO (70ppm)	% removal of MO (100ppm)
$Al_{0.1}Co_{0.7}Mn_{0.3}Fe_{1.9}O_4$	14.38	4.17	0.90	11.44
$Al_{0.3}Co_{0.7}Mn_{0.3}Fe_{1.7}O_4$	47.23	70.36	73	74.52
$Al_{0.5}Co_{0.7}Mn_{0.3}Fe_{1.5}O_4$	12.02	39.53	53.6	51.06
$Al_{0.7}Co_{0.7}Mn_{0.3}Fe_{1.3}O_4$	50.15	67.65	73.21	72.57
$Al_{0.9}Co_{0.7}Mn_{0.3}Fe_{1.1}O_4$	2.076	67.65	65.52	65.66
METHYLENE BLUE (MB)				
Adsorbent	**% removal of MB 30PPM**	**% removal of MB 50PPM**	**% removal of MB 70PPM**	**% removal of MB 100PPM**
$Al_{0.1}Co_{0.7}Mn_{0.3}Fe_{1.9}O_4$	84.29	74.30	71.72	41.28
$Al_{0.3}Co_{0.7}Mn_{0.3}Fe_{1.7}O_4$	56.39	30.70	27.33	4.07
$Al_{0.5}Co_{0.7}Mn_{0.3}Fe_{1.5}O_4$	77.91	53.64	44.71	10.35
$Al_{0.7}Co_{0.7}Mn_{0.3}Fe_{1.3}O_4$	69.97	36.20	28.40	2.69
$Al_{0.9}Co_{0.7}Mn_{0.3}Fe_{1.1}O_4$	76.52	38.2	31.66	7.09

4.1.7 Study of thermodynamic parameters

To investigate the adsorption process thermodynamically, free energy change (ΔG^o), entropy change (ΔS^o), and enthalpy change (ΔH^o), for the dye adsorption process were calculated using following equations.

Equation (9) was used to calculate Gibb's free energy (ΔG^o).

$$\Delta G^o = - RT \ln K_d \qquad (9)$$

Here K_d refers to distribution equilibrium constant, and R is the universal gas constant.
The expression for the adsorption constant K_d is as follows [7].

$$K_d = C_{ad}/C_e \qquad (10)$$

C_e (in mg/l) is the equilibrium concentration of solute in solution and C_{ad} (in mg/l) is the concentration of solute adsorbed at equilibrium respectively.
The van't Hoff Equation (11) was employed to determine the ΔH^o and ΔS^o values for the adsorption process.

$$\Delta G^o = \Delta H^o - T\Delta S^o \qquad (11)$$

A linear plot between ln K_d and 1/T was used to calculate the ΔH^o and ΔS^o parameters. Table 4.4 displays various thermodynamic parameter calculated by using above given equations. With an increase in temperature, $\Delta G°$ further decreases, which is attributed to rise in temperature favoring the product formation in an endothermic reaction. This decrease in the value of $\Delta G°$ indicates that the reaction becomes more spontaneous in the forward direction. The positive $\Delta H°$ for dye adsorption indicates that higher temperatures are more favorable for this adsorption process, depicting the endothermic nature. The mobility of the dye molecules improves at high temperatures, which makes it easier for them to separate from water molecules and form bonds with the adsorbent surface. Dyes lose their hydration shells when they attach themselves to solid surfaces and become dehydrated. The process of dehydration raises entropy ($\Delta S°$). A positive change of $\Delta S°$ reveals that the system is more disordered, improving the reaction's spontaneity.

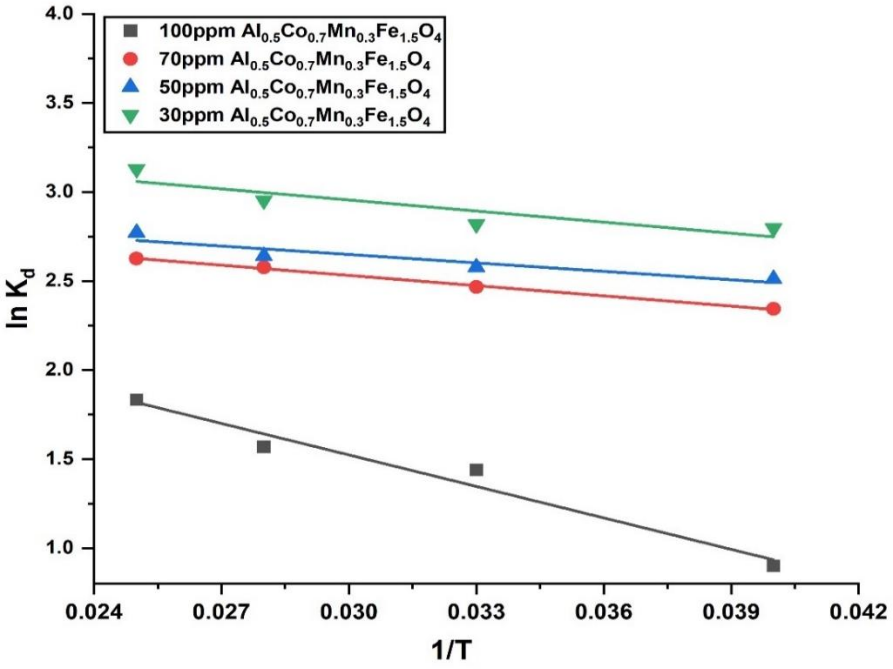

Figure 4.10: The adsorption thermodynamic parameters are calculated using a plot of ln K_d vs 1/T.

Table 4.4: The dye adsorption thermodynamic parameters for Al-doped Co-Mn mixed transition metal ferrite ($Al_{0.5}Co_{0.7}Mn_{0.3}Fe_{1.5}O_4$).

Concentration(mg/L)/ Dye	Temperature (Kelvin)	ΔG^o (kJ/mol)	ΔH^o (kJ/mol)	ΔS^o (kJ/mol.K)
30mg/L (CR)	298 303 308 318	-5.505 -5.575 -5.523 -5.407	0.057	39.22
50mg/L (CR)	298 303 308 313	-5.291 -5.363 -5.438 -5.503	0.017	23.40
70mg/L (CR)	298 303 308 313	-5.426 -5.433 -5.521 -5.607	0.011	21.15
100mg/L (CR)	298 303 308 313	-6.633 -6.557 -6.646 -6.674	0.081	42.84

4.1.8 Adsorption isotherms

To develop better understanding of adsorption processes, an adsorbent's adsorptive properties are reflected by its adsorption isotherm [8]. Modelling adsorption isotherms is crucial for understanding adsorption process. The $Al_{0.5}Co_{0.7}Mn_{0.3}Fe_{1.5}O_4$/CR dye system has been described using commonly employed adsorption isotherm models. Table 4.5 displays the parameters for various isotherm models. In these models, the adsorption capacity (q_e) and the highest adsorption capacity for complete monolayer coverage (q_{max}) are measured in mg/g. 'C_e' refers to equilibrium concentration after adsorption (in mg/L), and 'b' represents the Langmuir constant (L/mg). The constants 'n' and 'k_f' represent the nonlinearity/linearity between the adsorption rates and the solution concentration of the material. The adsorption potential is denoted by 'e', the D-R isotherm constant is represented by 'k' and the maximum binding energy (L/g) is indicated by 'A'. The Temkin constant (b_t), which reflects the heat of adsorption, is expressed in (J/mg).

Table 4.5: Graphical and general equations illustration of adsorption isotherms [9].

Adsorption isotherm	**Langmuir**	**Freundlich**	**Temkin**	**Dubinin-Raduskevich (D-R)**
Adsorption behavior	Homogenously	Heterogeneously	Adsorption heat is linear as opposed to logarithmic.	On the surface, porosity is homogeneous.
Equation	$\frac{1}{q_e} = \frac{1}{q_{max}} + \frac{1}{bq_{max}\,C_e}$	$logq_e = logk_f + \frac{1}{n}logC_e$	$q_{e=BlnA+BlnC_e}$	$lnq_e = lnq_{max} - ke^2$ e=RT ln (1+1/C_e)
Graphical representation	1/q_e vs1/C_e	log q_e vs log C_e	q_e vs ln C_e	ln q_e vs e^2

The adsorption isotherm displays the distribution connection between the adsorbent and adsorbate molecules at equilibrium. The adsorption isotherm was calculated using the Langmuir, D-R, Freundlich, and Temkin isotherm models, as demonstrated in figure 4.11. The necessary variables that were ascertained utilizing the various adsorption isotherms are shown in table 4.6. The correlation coefficient (R^2) values demonstrate how well the D-R isotherm model fits the adsorption data. This suggests that the surface of the ($Al_{0.5}Co_{0.7}Mn_{0.3}Fe_{1.5}O_4$) adsorbent experienced homogeneous adsorption of the CR dye.

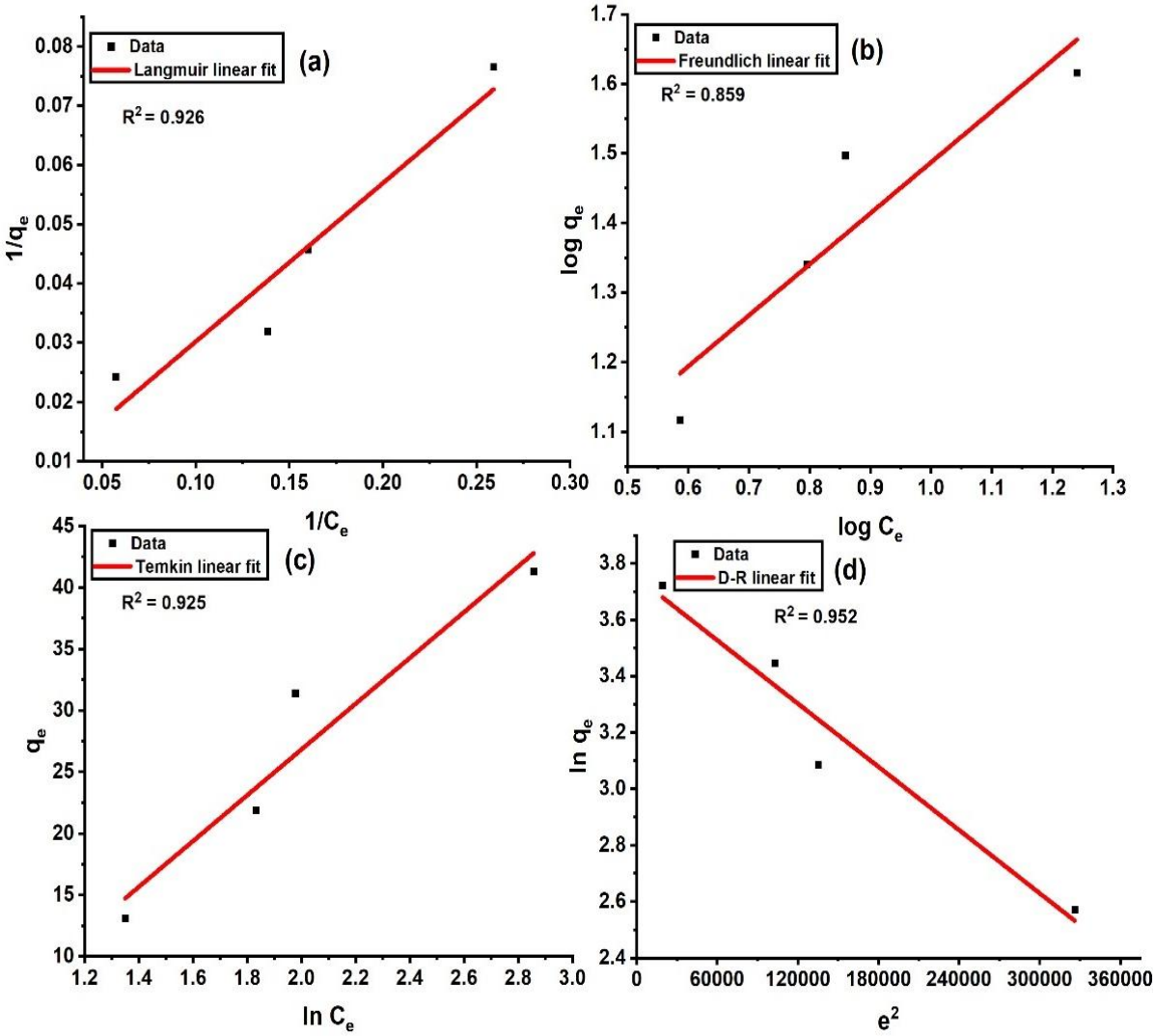

Figure 4.11: (a) Langmuir model (b) Freundlich model (c) Temkin model (d) D-R model.

Table 4.6: The parameters obtained from the isotherms-Freundlich, Temkin, Langmuir, and D-R models.

Adsorption isotherms parameters			
Langmuir model	Freundlich model	Temkin model	D-R model
$q_{max} = 285.7$	$K_f = 2.12$	B = 18.60	$q_{max} = 42.56$
$b = 1$	1/n = 0.73	A = 0.57	$K = 4$
$R^2 = 0.926$	$R^2 = 0.859$	$R^2 = 0.925$	$R^2 = 0.952$
$R_L = 0.9$	n = 1.36	$b_t = 53.09$	$E_s = 1.414$

4.1.9 Adsorption kinetics

The pseudo-first- order (PFO) and pseudo-second- order (PSO) Lagergren kinetic models were utilized to fit the experimental findings to ascertain the dye adsorption kinetics from an aqueous solution. The following formulas were used for these kinetic models [10].

$$\ln (q_e - q_t) = \ln q_e - k_1 t \qquad (12)$$

$$\frac{t}{q_t} = \frac{1}{k_2 q_e^2} + \frac{t}{q_e} \qquad (13)$$

A linear plot of ln (qe-qt) over time 't' (in minutes) yielded the slope and intercept values, which were then utilized to determine the adsorption capacity and first-order rate constants of CR dye for different initial concentrations. The PSO kinetic model was fitted well to the experimental data to provide the insight for adsorption mechanism. The kinetic constants of the second order were determined by a linear plot of t/q_t vs t (min). Linear regression analysis was used for both PFO and PSO models to get the coefficient of determination (R^2). Table 4.7 displays the R^2 values calculated from these fitting models. The R^2 values for PSO kinetics were greater than that of PFO kinetics. The adsorption system's pseudo first- and second-order kinetic modelling is demonstrated in figure 4.12. These results revealed that the PSO kinetic model effectively characterizes the CR dye adsorption onto Al-doped mixed spinel ferrite.

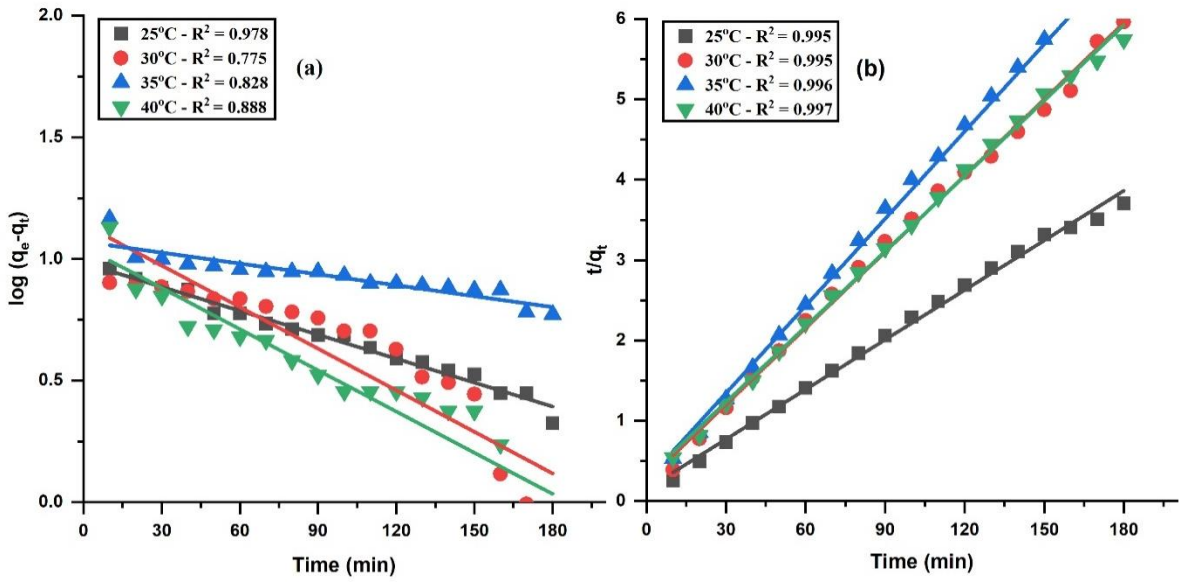

Figure 4.12: Model fitting of (a) PFO and (b) PSO for CR dye adsorption onto ($Al_{0.5}Co_{0.7}Mn_{0.3}Fe_{1.5}O_4$) surface.

Table 4.7: Adsorption kinetic model parameters for PFO and PSO analysis.

Dye/Adsorbent		**pseudo-first order**			**pseudo-second order**		
Congo Red ($Al_{0.5}Co_{0.7}Mn_{0.3}Fe_{1.5}O_4$)	Temp. (°C)	Q_e (mg/g)	$k_1 \times 10^3$ (min^{-1})	R^2	Q_e (mg/g)	$k_2 \times 10^4$ (g/mg.min)	R^2
	25	2.67	3.3	0.978	48.54	28.02	0.995
	30	3.13	5.7	0.775	33.55	28.05	0.995
	35	2.91	1.5	0.828	33.55	28.05	0.996
	40	2.85	5.6	0.888	31.94	33.37	0.997

4.2. Al-doped Ni-Mn ferrite

4.2.1 Fourier transform infrared (FTIR) analysis

FTIR spectra of Al-doped Ni-Mn mixed transition metal ferrites in the region 4000 cm^{-1}-400 cm^{-1} are shown in Figure 4.13. All spinel ferrites exhibit three primary absorption bands in their infrared spectra that represent the metal-oxygen bond. The metal-oxygen band in the 500–650 cm^{-1} range is associated with Mn^{2+}-O, indicating tetrahedral sites, while the metal-oxygen band in the 300-450 cm^{-1} range corresponds to Fe^{3+}-O and Ni^{2+}-O, which exhibits the octahedral sites [11]. However, the stretching around ~1400-1100 cm^{-1} corresponds to the Al^{3+}-O bond [2]. The mass of the metal cation and the strength of its connection with oxygen determine the frequency at which absorption occurs.

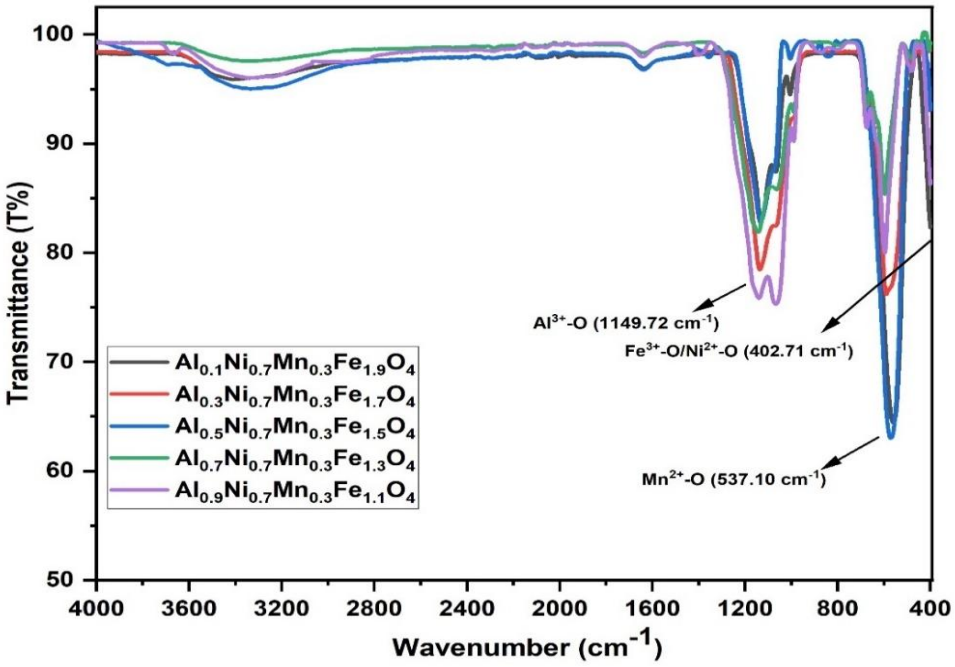

Figure 4.13: FTIR spectra of Al-doped Ni-Mn mixed transition metal ferrites.

4.2.2 X-ray powder diffraction (XRD) analysis

In Figure 4.14, the powder XRD patterns of the samples depict the single-phase features of a cubic spinel crystal structure having Fd-3m space group. The diffraction peaks at 2θ values of 25.38°, 30.0°, 33.20°, 35.7°, 43.3°, 54.0°, 57.3°, and 63.18° are corresponding to the crystal planes (200), (220), (300), (311), (400), (422), (511) and (440) respectively [11]. The crystallite size 'D' of Al-doped mixed transition metal ferrite was calculated using Debye Scherrer equation from the strongest and sharpest peak (311) of XRD pattern [3].

$$D_{(hkl)} = \frac{K\lambda}{\beta cos\theta} \qquad (1)$$

'K' is a dimensionless shape factor, '*D'* is the mean crystallite dimension (nm), 'λ' refers to the wavelength of X-ray (nm), 'β' is line broadening at half the maximum intensity (rad), and 'θ' is Bragg's diffraction angle (rad). The diffraction line broadens due to the strain and crystallite size contribution, as stated by Williamson and Hall (W-H). This methodology offers a more straightforward method that differentiates between strain- and size-induced broadening of peak by computing the width of peak against function of 2θ. The strain-induced widening brought on by distortions and crystal imperfection was calculated using following formula.

$$\varepsilon = \frac{\beta}{4tan\theta} \qquad (2)$$

Equations (1) and (2) demonstrated that strain varies as tan θ and that the width of the peak varies as $\frac{1}{cos\theta}$. At this point, the material's strain and crystallite size contributions may be multiplied to describe the total peak broadening.

$$\beta_{(hkl)} = \beta_{(D)} + \beta_{(\varepsilon)} \qquad (3)$$

where $\beta_{(\varepsilon)}$ represents strain-induced widening, $\beta_{(D)}$ represents crystallite size, and $\beta_{(hkl)}$ represents the breadth of the half-maximum intensity. Table 4.8 illustrates how the size of the crystallites and the material's internal stress/strain affect the line width of the spectra. Two useful methods for calculating these effects are the Williamson-Hall analysis and the Scherrer equation. Broader peaks are produced by smaller crystallites, and strain produces broadening those changes with diffraction angle.

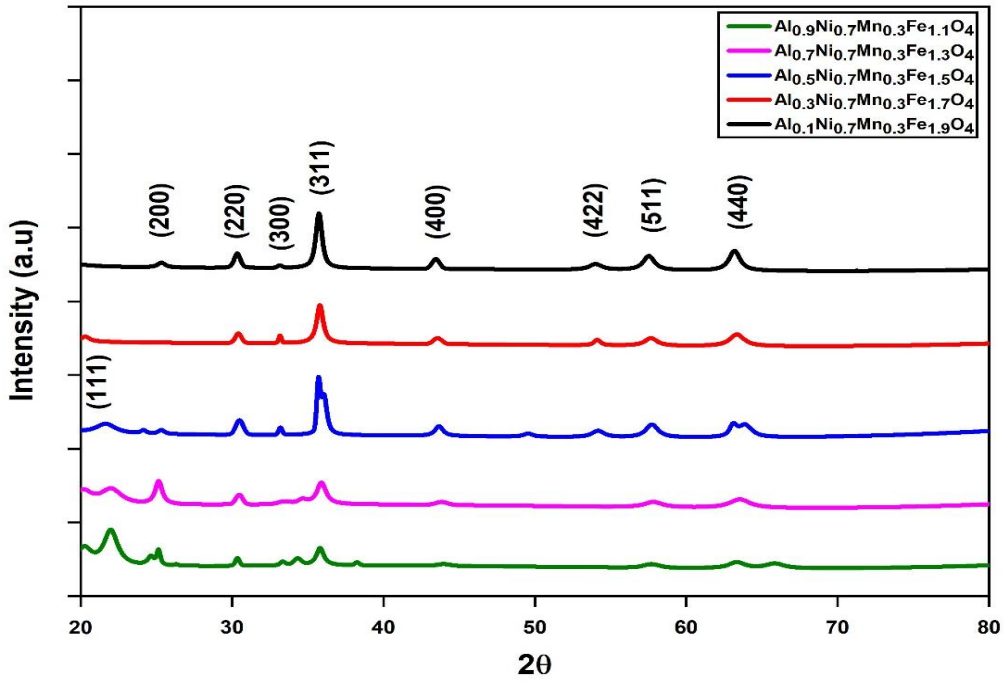

Figure 4.14: X-ray powder diffraction pattern of Al-doped Ni-Mn mixed transition metal ferrites.

Table 4.8: Crystallite size and strain of Al-doped Ni-Mn ferrite.

Ferrite ($Al_xCu_{0.7}Mn_{0.3}Fe_{2-x}O_4$)	**D (nm)**	**$\delta \times 10^{-3}$ (nm^{-2})**	**$\in \times 10^{-3}$**
X = 0.1	0.223	19987.15	457.28
X = 0.3	0.433	5310.39	235.67
X = 0.5	1.138	772.14	89.65
X = 0.7	1.429	489.20	71.19
X = 0.9	5.314	35.40	19.24

4.2.3 Field emission scanning electron microscopy (SEM) analysis

The surface morphology of Al-doped Ni-Mn ferrite was observed by using a scanning electron microscope. The nano-granular structure of the ferrite sample is displayed in Figure 4.15 (a). Figure 4.15(b) shows the EDS spectra, where the elemental proportions closely aligned with the atomic percentage and weight percentage of these elements, namely O, Fe, Ni, Al and Mn.

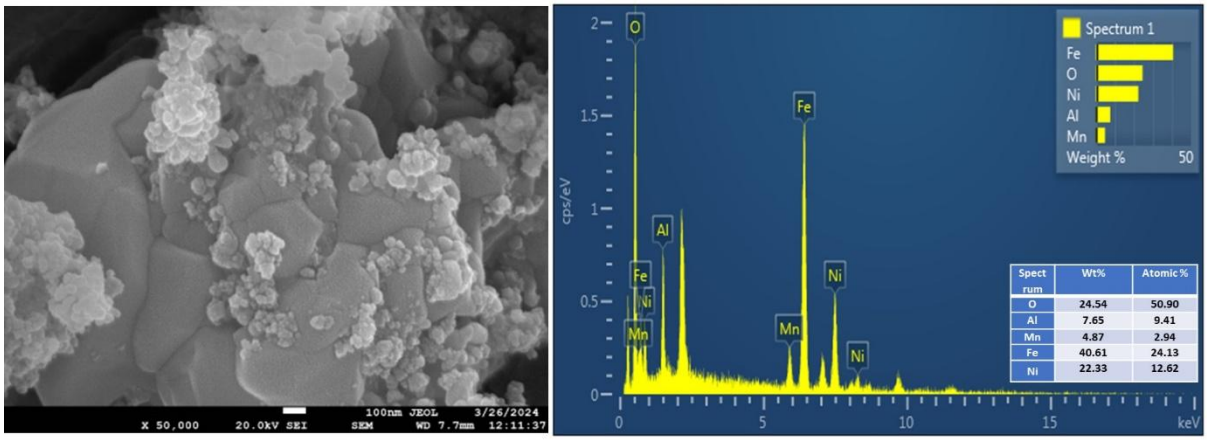

Figure 4.15 (a) SEM image (b) EDS of $Al_{0.5}Ni_{0.7}Mn_{0.3}Fe_{1.5}O_4$ ferrite.

4.2.4 Vibrating sample magnetometer (VSM) analysis

The magnetic hysteresis curve of ferrite sample, $Al_xNi_{0.7}Mn_{0.3}Fe_{2-x}O_4$, annealed at 650°C, is illustrated in Figure 4.16. The ferrite samples exhibited soft superparamagnetic behavior. The net magnetization of the spinel lattice is the main factor that determines the molecular weight and saturation magnetization of the soft ferrites. Table 4.9 reports the magnetic properties of room-temperature ferrite samples. The experimental magnetic moment (μ_B) and the anisotropy constant (K) were calculated as follows [4, 5].

$$\mu_B = \frac{MmMs}{5585} \quad (4)$$

$$H_C = \frac{0.96K}{Ms} \quad (5)$$

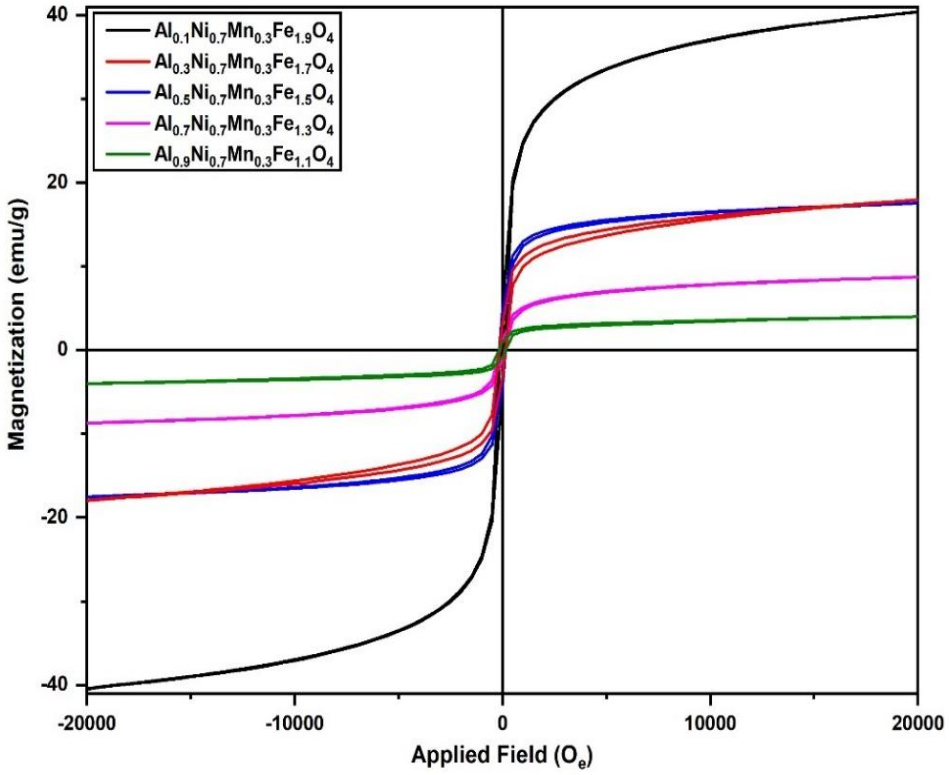

Figure 4.16: Hysteresis curves of $Al_xNi_{0.7}Mn_{0.3}Fe_{2-x}O_4$ ferrites at room temperature.

Table 4.9: Saturation magnetization (M_s), anisotropy constant (K), remanence (M_r), magnetic moment (μ_B), and coercivity (H_c) of $Al_xNi_{0.7}Mn_{0.3}Fe_{2-x}O_4$ ferrites at room temperature.

Sample ($Al_xNi_{0.7}Mn_{0.3}Fe_{2-x}O_4$)	M_S (emu.g^{-1})	M_r (emu.g^{-1})	H_c (O_e)	M_r/ M_S	μ_B	K×10^{-3} (emu.O_e g^{-1})
X = 0.1	40.39	4.69	97.09	0.11	1.66	4.08
X = 0.3	18.02	3.13	147.56	0.17	0.72	2.76
X = 0.5	17.05	4.69	164.69	0.27	0.67	2.92
X = 0.7	8.68	1.10	119.94	0.12	0.33	1.08
X = 0.9	4.02	0.85	164.69	0.21	0.14	0.71

4.2.5 Brunauer–Emmett–Teller (BET) analysis

In Figure 4.17, the as-synthesized ferrite samples' porosity and specific surface area were assessed using the nitrogen adsorption-desorption technique. The surface area, pore volume and pore radius of ferrite material is estimated as 23.331 m^2/g, 0.234 cc/g and 15.248 Å respectively. The adsorption activity of ferrite material is highly dependent on surface area.

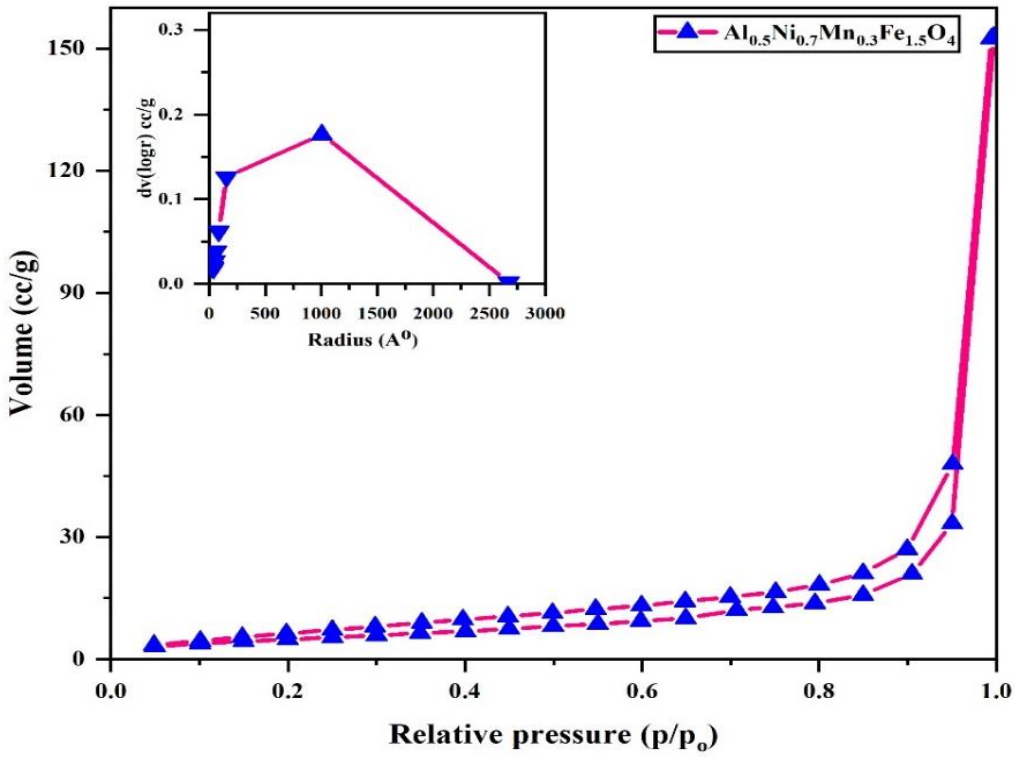

Figure 4.17: BET isotherm of $Al_{0.5}Ni_{0.7}Mn_{0.3}Fe_{1.5}O_4$ ferrite.

4.2.6 Al-doped Ni-Mn mixed ferrites for adsorption of dyes

UV-visible absorption spectroscopy was used to assess adsorption capability of the ferrite samples, $Al_xNi_{0.7}Mn_{0.3}Fe_{2-x}O_4$, for the removal of dyes from aqueous solutions, such as CR, MO, MB, and CV. For the adsorption studies, various dye concentrations (30ppm, 50ppm, 70ppm, and 100ppm) with fixed $Al_xNi_{0.7}Mn_{0.3}Fe_{2-x}O_4$ dosage (0.1g) were employed. Table 4.10 presents the percentage removal of various dye concentrations with different ferrite materials. Using equations (6) and (7), the % dye removal efficiency and the quantity of dye uptake at equilibrium (qe, mg/g) were calculated [6].

$$\text{Removal } (\%) = \frac{(C_0 - C_e)}{C_0} \times 100 \qquad (6)$$

$$q_e = \frac{(C_0 - C_e)V}{m} \qquad (7)$$

Where C_o, C_e, m, and V are the initial adsorbate concentrations (mg/L), equilibrium adsorbate concentrations (mg/L), adsorbent mass (g), and volume in litres respectively.

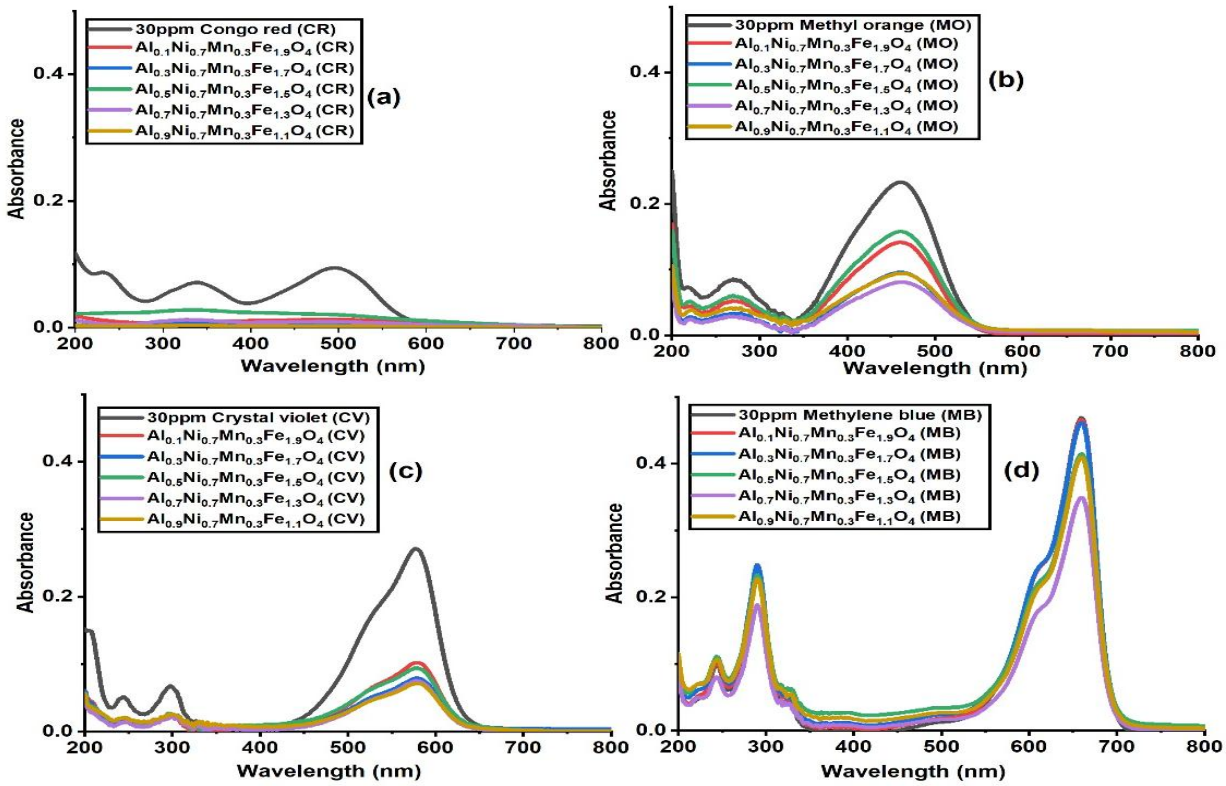

Figure 4.18: UV-visible absorption spectra of dyes solutions at 30 ppm.

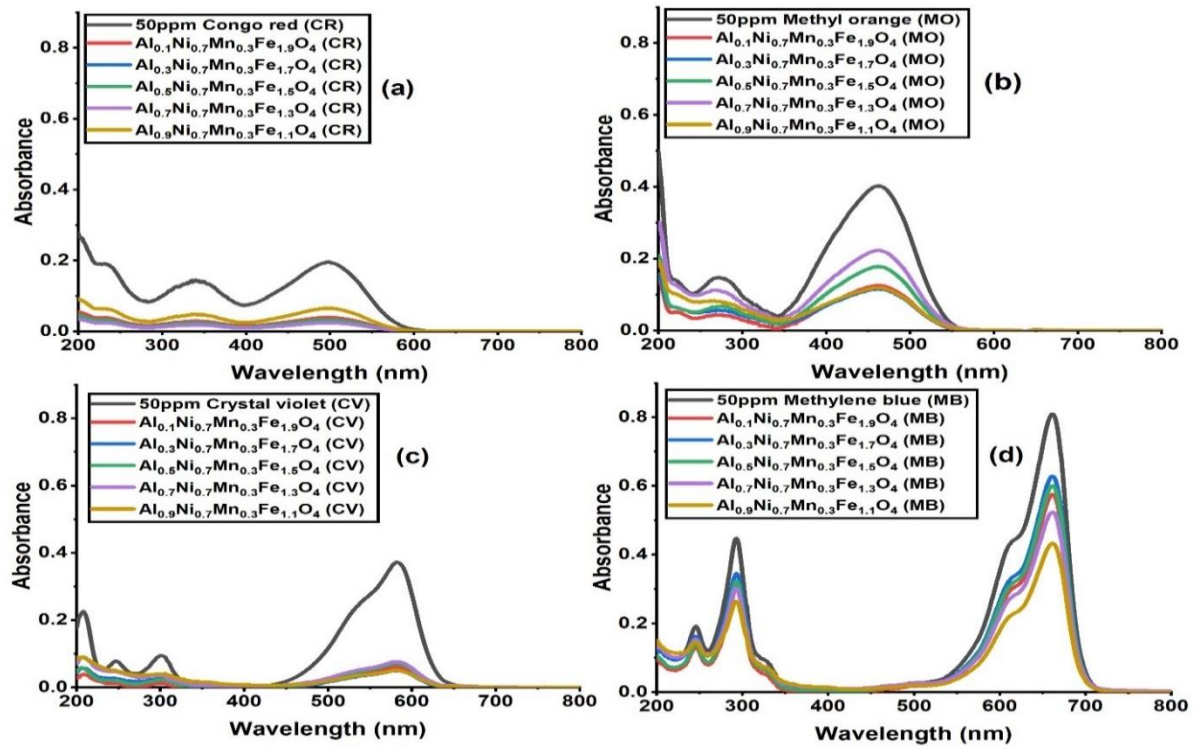

Figure 4.19: UV-visible absorption spectra of dyes solutions at 50 ppm.

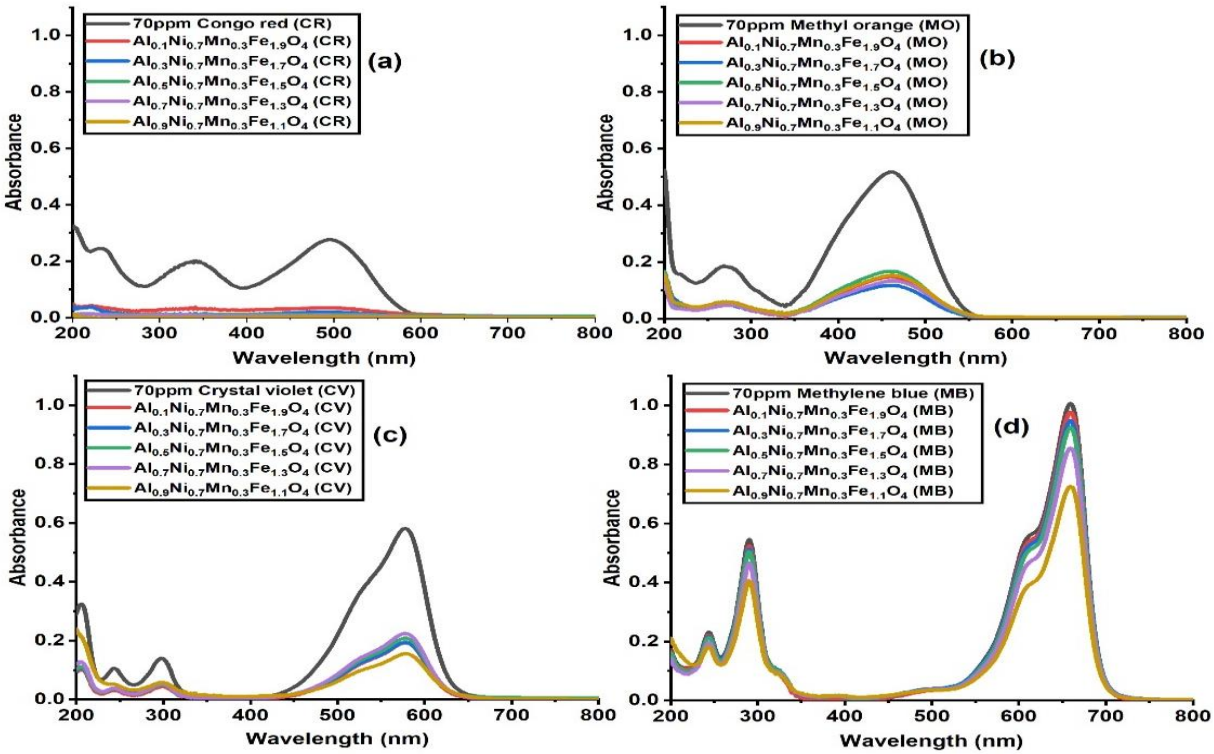

Figure 4.20: UV-visible absorption spectra of dyes solutions at 70 ppm.

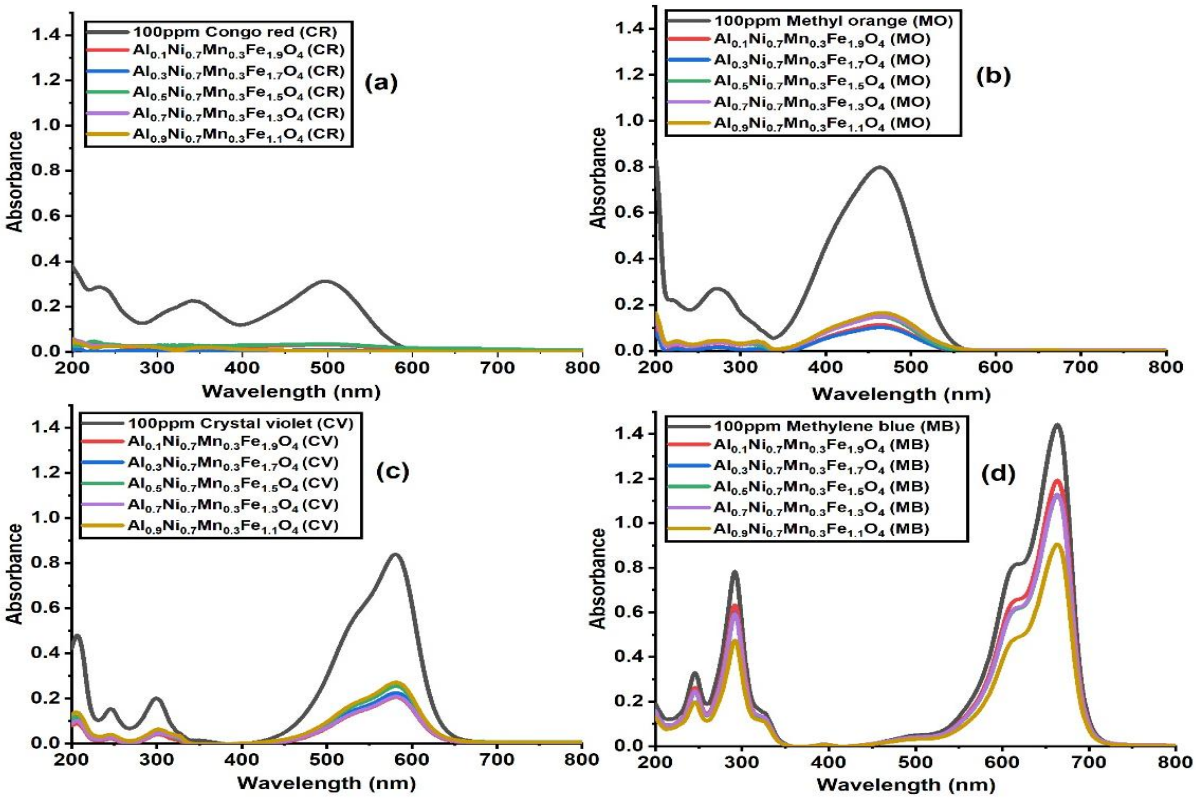

Figure 4.21: UV-visible absorption spectra of dyes solutions at 100 ppm.

Table 4.10: Percentage removal of various dye concentrations using Al-doped Ni-Mn ferrites.

CONGO RED (CR)				
Adsorbent	**% removal of CR (30ppm)**	**% removal of CR (50ppm)**	**% removal of CR (70ppm)**	**% removal of CR (100ppm)**
$Al_{0.1}Ni_{0.7}Mn_{0.3}Fe_{1.9}O_4$	86.17	90.25	87.31	89.42
$Al_{0.3}Ni_{0.7}Mn_{0.3}Fe_{1.7}O_4$	96.80	95.89	92.75	97.11
$Al_{0.5}Ni_{0.7}Mn_{0.3}Fe_{1.5}O_4$	77.65	86.15	79.34	88.78
$Al_{0.7}Ni_{0.7}Mn_{0.3}Fe_{1.3}O_4$	96.80	96.41	97.46	99.03
$Al_{0.9}Ni_{0.7}Mn_{0.3}Fe_{1.1}O_4$	96.80	96.41	99.27	98.71
METHYL ORANGE (MO)				
Adsorbent	**% removal of MO (30ppm)**	**% removal of MO (50ppm)**	**% removal of MO (70ppm)**	**% removal of MO (100ppm)**
$Al_{0.1}Ni_{0.7}Mn_{0.3}Fe_{1.9}O_4$	39.48	68.90	71.56	85.71
$Al_{0.3}Ni_{0.7}Mn_{0.3}Fe_{1.7}O_4$	58.79	71.39	77.36	87.21
$Al_{0.5}Ni_{0.7}Mn_{0.3}Fe_{1.5}O_4$	32.61	55.97	67.69	81.45
$Al_{0.7}Ni_{0.7}Mn_{0.3}Fe_{1.3}O_4$	65.23	44.52	74.27	81.20
$Al_{0.9}Ni_{0.7}Mn_{0.3}Fe_{1.1}O_4$	59.65	70.64	70.40	79.19
CRYSTAL VIOLET(CV)				
Adsorbent	**% removal of CV 30PPM**	**% removal of CV 50PPM**	**% removal of CV 70PPM**	**% removal of CV 100PPM**
$Al_{0.1}Ni_{0.7}Mn_{0.3}Fe_{1.9}O_4$	62.22	91.92	66.72	75.53
$Al_{0.3}Ni_{0.7}Mn_{0.3}Fe_{1.7}O_4$	70.74	93.27	66.55	73.15
$Al_{0.5}Ni_{0.7}Mn_{0.3}Fe_{1.5}O_4$	65.18	90.57	64.12	69.68
$Al_{0.7}Ni_{0.7}Mn_{0.3}Fe_{1.3}O_4$	72.22	89.77	61.35	75.05
$Al_{0.9}Ni_{0.7}Mn_{0.3}Fe_{1.1}O_4$	73.70	93.13	73.13	67.66
METHYLENE BLUE (MB)				
Adsorbent	**% removal of MB 30PPM**	**% removal of MB 50PPM**	**% removal of MB 70PPM**	**% removal of MB 100PPM**
$Al_{0.1}Ni_{0.7}Mn_{0.3}Fe_{1.9}O_4$	0.63	28.92	2.88	17.33
$Al_{0.3}Ni_{0.7}Mn_{0.3}Fe_{1.7}O_4$	1.49	22.37	5.76	21.84
$Al_{0.5}Ni_{0.7}Mn_{0.3}Fe_{1.5}O_4$	11.51	25.83	8.05	22.12
$Al_{0.7}Ni_{0.7}Mn_{0.3}Fe_{1.3}O_4$	25.58	35.22	15.00	21.98
$Al_{0.9}Ni_{0.7}Mn_{0.3}Fe_{1.1}O_4$	12.79	46.47	27.93	37.23

4.2.7 Thermodynamic study

From the adsorption studies of Congo red dye at various temperatures (298K, 303K, 308K, 313K), thermodynamic parameters (Table 4.11) were calculated by using equation 9-11.

$$\Delta G^o = - RT \ln K_d \quad (9)$$

$$K_d = C_{ad}/C_e \quad (10)$$

For the adsorption process, van't Hoff equation was used to estimate the entropy (S) and enthalpy (H) of the reaction.

$$\ln k_{eq} = -\frac{\Delta H^O}{RT} + \frac{\Delta S^O}{R} \quad (11)$$

From above equation - $\frac{\Delta H^O}{R}$ is the slope, and $\frac{\Delta S^O}{R}$ is the intercept of the linear fit. It is simple to determine the enthalpy and entropy by using the van't Hoff plot's slope and intercept.

$$\Delta H^o = -R \times slope$$

$$\Delta S^o = R \times intercept$$

When the ΔH^o value is positive, it signifies the heat is absorbed in the dye removal procedure. This suggests that the interactions between the adsorbate and the adsorbent surface are stronger than those between the dye molecules in the solution. A positive change of ΔS^o reveals an increase in entropy during the dye-removal process and may imply that the adsorption process promotes disorder or randomness. For instance, the dye molecules may adhere to the surface of the adsorbent material, allowing them more freedom compared to when they were in solution. The positive change of ΔH^o implies that this adsorption process is endothermic and the negative change of ΔG^o denotes the spontaneous nature of the process. With an increase in temperature ΔG^o values further decrease, which indicate that high temperature favors this adsorption process.

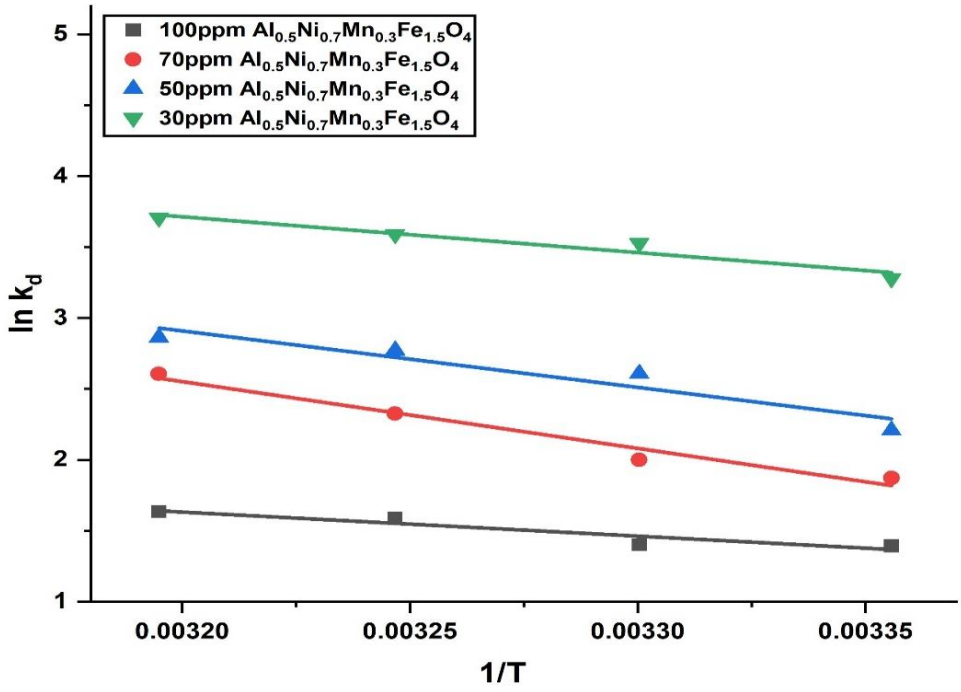

Fig 4.22: Adsorption thermodynamic parameters derived from the linear connection between 1/T (Kelvin temperature inverse) and ln K_d.

Table 4.11: The dye adsorption thermodynamic parameters for Al-doped Ni-Mn mixed transition metal ferrite ($Al_{0.5}Ni_{0.7}Mn_{0.3}Fe_{1.5}O_4$).

Concentration(mg/L)/ Dye	Temperature (Kelvin)	ΔG^o (kJ/mol)	ΔH^o (kJ/mol)	ΔS^o (kJ/mol/K)
30mg/L (CR)	298	-8.12	21.00	0.09
	303	-8.88		
	308	-9.19		
	313	-9.64		
50mg/L (CR)	298	-5.47	33.08	0.13
	303	-6.57		
	308	-7.10		
	313	-7.44		
70mg/L (CR)	298	-4.64	39.13	0.14
	303	-5.03		
	308	-5.95		
	313	-6.78		
100mg/L (CR)	298	-3.45	14.09	0.05
	303	-3.53		
	308	-4.07		
	313	-4.25		

4.2.8 Adsorption isotherms

An adsorbent's adsorptive properties are represented by its adsorption isotherm to establish adsorption processes. Modelling adsorption isotherms is crucial for understanding the adsorbent and adsorbate interactions, which have different adsorption kinetics. The $Al_{0.5}Ni_{0.7}Mn_{0.3}Fe_{1.5}O_4$/CR dye system was described using the adsorption isotherms that are frequently employed in this context: Langmuir, Dubinin-Radushkevich, Temkin and Freundlich models. In these models, the adsorption capacity (mg/g) is denoted by (qe). On an adsorbent surface, (q_{max}) is the maximum quantity of adsorption with full monolayer coverage (mg/g), The constant of Langmuir (L/mg) is denoted by 'b' and the concentration at equilibrium (mg/L) following adsorption is denoted by (C_e). The adsorption potential is represented by 'e' and the D-R isotherm constant by 'K'. 'A' and 'b_t' refers to maximal binding energy and Temkin respectively. 'n' and 'K_f' indicate the nonlinearity/linearity between adsorption rates and the solution concentration.

When this process reaches equilibrium, the distribution connection between the adsorbent and adsorbate molecules is displayed by this isotherm. As seen in Figure 4.23, the adsorption isotherm was computed using the Langmuir, Temkin, D-R isotherms and Freundlich models. The relevant variables that were ascertained utilizing the various adsorption isotherms are shown in Table 4.12. The R^2 values demonstrate that Freundlich model provide a good fit for the adsorption isotherms. This suggests that the adsorbent's surface ($Al_{0.5}Ni_{0.7}Mn_{0.3}Fe_{1.5}O_4$) experienced heterogeneous adsorption of the CR dye. Comparative analyses demonstrate the considerable potential of the mixed transition metal ferrite employed in this investigation to eliminate CR dye.

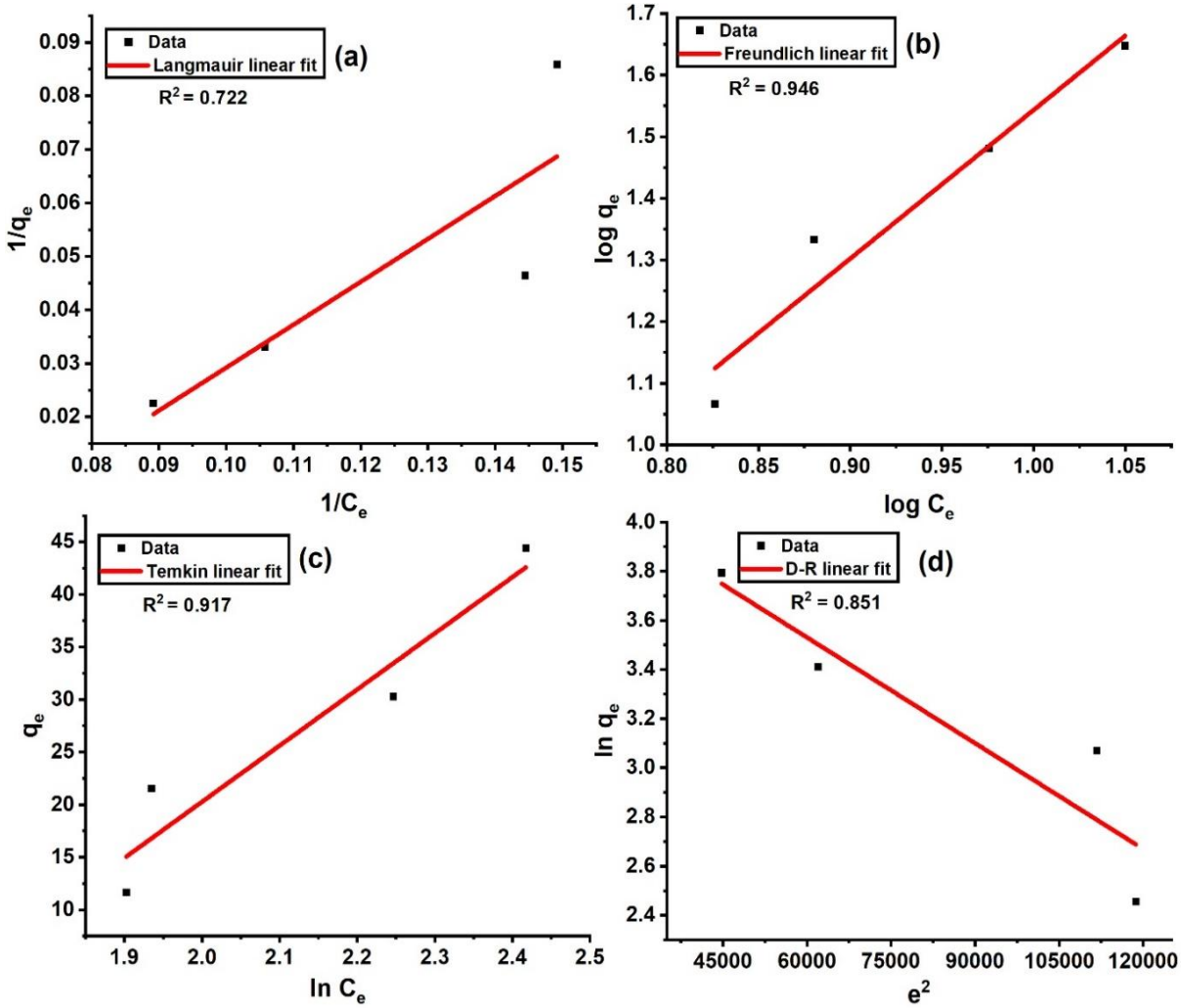

Figure 4.23: (a) Langmuir model (b) Freundlich model (c) Temkin model (d) D-R model.

Table 4.12: Adsorption isotherm parameters for Al-doped Ni-Mn mixed transition metal ferrite.

Adsorption Isotherms Parameters			
Langmuir isotherm	Freundlich isotherm	Temkin isotherm	D-R isotherm
q_{max} = -15.70	K_f = 0.13	B = 46.65	q_{max} =80.76
b = 0.02	1/n = 2.410	A = 0.15	K = 1
R^2 = 0.722	R^2 = 0.946	R^2 = 0.917	R^2 = 0.851
R_L = -0.9	n = 0.41	b_t= 53.09	E_s = 0.707

4.2.9 Adsorption kinetics

Kinetic models and parameters can be used to ascertain the kinetics and mechanism of dye adsorption. To match the experimental results, the PFO and PSO Lagergren models were employed in this work. The equations 12 and 13 were used for these PFO and PSO distinct models [10].

$$\ln (q_e - q_t) = \ln q_e - k_1 t \qquad (12)$$

$$\frac{t}{q_t} = \frac{1}{k_2 q_e^2} + \frac{t}{q_e} \qquad (13)$$

Using the intercept and slope, the adsorption capacity and first-order rate constants of CR dye at various starting concentrations were found. The linear plot of ln (q_e-q_t) over time (min) was used to calculate intercept and slope. The kinetic constants of the second-order were determined by a linear plot of t/q_t vs. t (min). Linear regression analysis was employed for PFO and PSO models to get the coefficient of determination (R^2). Table 4.13 displays the R^2 values, representing how well the model matches the adsorption system. The R^2 values for PSO kinetics were higher than that of PFO kinetics. Figure 4.24 shows the adsorption system's first- and second-order kinetic modelling. These results indicate that PSO kinetic model adequately explained dye adsorption onto Al-doped Ni-Mn mixed transition metal ferrite for CR dye.

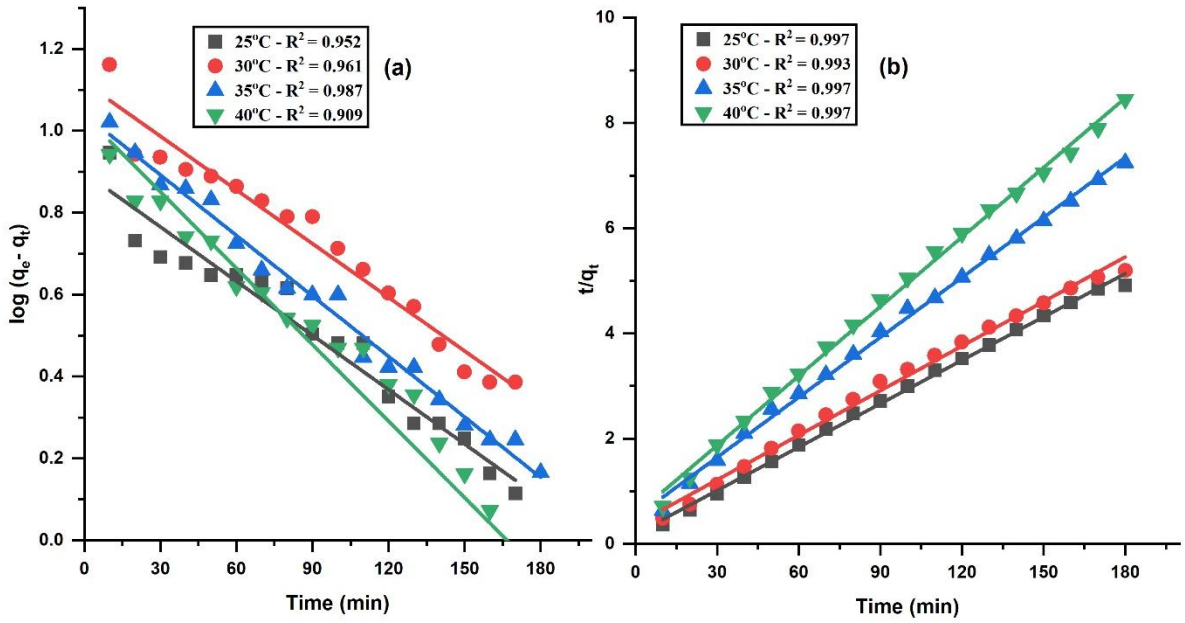

Figure 4.24: Model fitting of (a) PFO and (b) PSO for CR dye adsorption onto ($Al_{0.5}Ni_{0.7}Mn_{0.3}Fe_{1.5}O_4$) surface.

Table 4.13: Adsorption kinetic model parameters for PFO and PSO analysis.

Dye/Adsorbent		PFO			PSO		
	Temp. (°C)	Q_e (mg/g)	$k_1 \times 10^3$ (min^{-1})	R^2	Q_e (mg/g)	$k_2 \times 10^4$ (g/mg.min)	R^2
Congo Red ($Al_{0.5}Ni_{0.7}Mn_{0.3}Fe_{1.5}O_4$)	25	8.11	4.6	0.952	36.36	40.55	0.997
	30	14.28	5.0	0.961	35.33	21.85	0.993
	35	10.96	4.9	0.987	26.31	28.60	0.997
	40	10.90	6.2	0.909	22.72	35.10	0.997

4.3. Al-doped Cu-Mn ferrite

4.3.1 Fourier-transform infrared (FTIR) analysis

The FTIR spectra of mixed transition metal ferrites doped with Al are shown in Figure 4.25, within 4000 cm^{-1} to 400 cm^{-1} range. The inherent stretching vibrations of the oxygen bonded metal cations are represented by three absorption bands in the spectra of these Al-doped Cu-Mn ferrites. As per the results, the absorption bands in the 300-450 cm^{-1} range are related with the Fe^{3+}-O and Cu^{2+}-O bonds [12] (also known as M_{oct}-O), and the band in the 500–650 cm^{-1} range is related with the Mn^{2+}-O bond (M_{tet}-O) [13]. Moreover, the stretching observed around ~1400-1100 cm^{-1}, signifies the presence of the Al^{3+}-O bond [2]. This behavior of absorption is related to the metal cations and occurs at different frequencies. This is facilitated either by their masses or the strength of their bond with oxygen. The FTIR analysis of these ferrites helps to provide very important information concerning the molecular structure of these elements by detailing the bonding configurations between the cations and the oxygen, which however has limited the ability to detect some bonds within the given spectrum analysis.

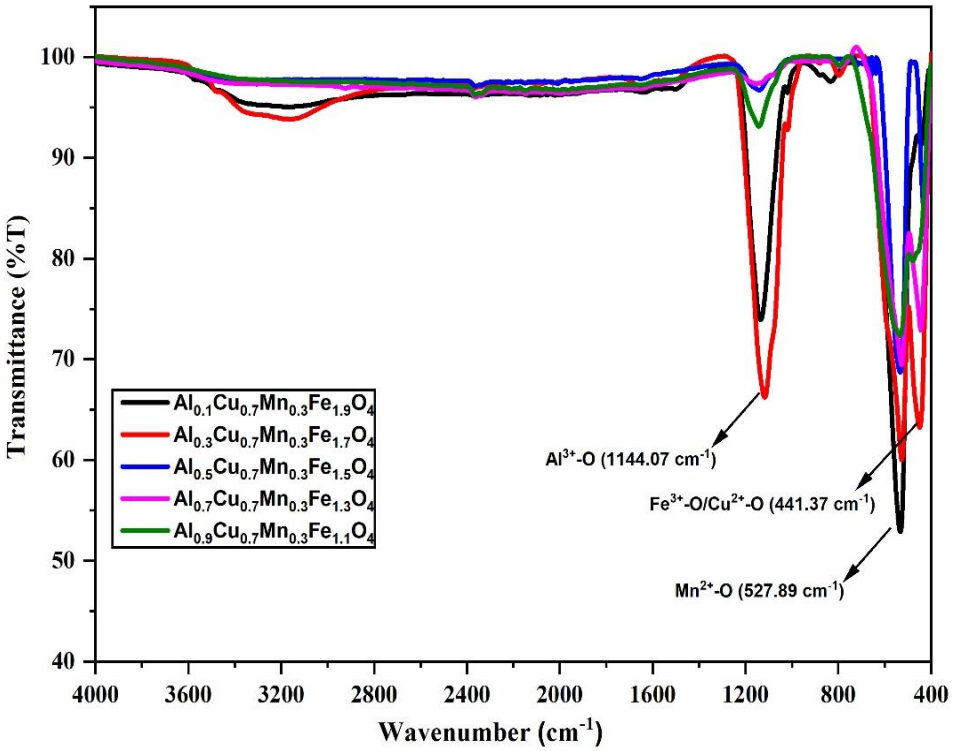

Figure 4.25: FTIR spectra of Al-doped Cu-Mn mixed transition metal ferrites.

4.3.2 X-ray powder diffraction (XRD) analysis

The XRD patterns of the samples are presented in Figure 4.26, which shows unique features suggestive of a cubic crystal structure of spinel in the Fd-3 m space group. The observed peaks, specifically at (200), (220), (300), (311), (400), (410), (422), (511), and (440), correspond to specific diffraction plane angles. These angles are measured at 25.38°, 30.0°, 33.20°, 35.7°, 43.3°, 54.0°, 57.3°, and 63.18°, respectively [12]. Table 4.14 presents the crystallite size and the strain within Al-doped Cu-Mn mixed transition metal ferrite. Two important methods for calculating these effects are the Williamson-Hall analysis and the Scherrer equation [14]. Broader peaks are produced by smaller crystallites, and strain produces broadening that changes with diffraction angle.

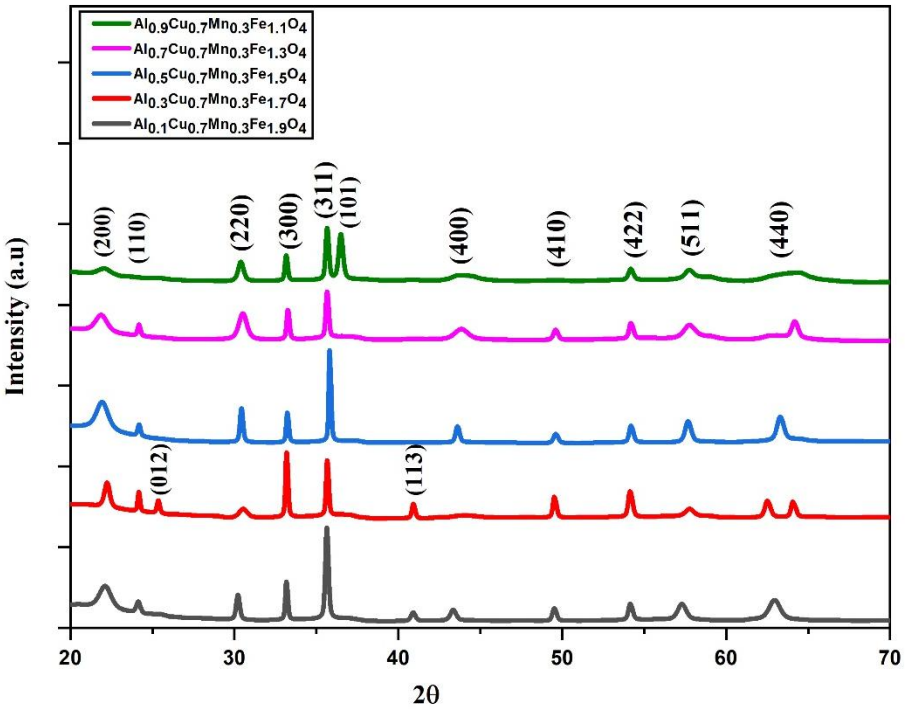

Figure 4.26: Powder XRD pattern of Al-doped Cu-Mn mixed transition metal ferrites.

Table 4.14: Crystallite size and strain of Al-doped Cu-Mn ferrite.

Ferrite ($Al_xCu_{0.7}Mn_{0.3}Fe_{2-x}O_4$)	D (nm)	$\delta \times 10^{-3}$ (nm^{-2})	$\in \times 10^{-3}$
X=0.1	1.581	399.660	64.90
X=0.3	2.860	122.212	35.89
X=0.5	4.498	49.423	22.69
X=0.7	5.690	30.880	18.04
X=0.9	8.368	14.277	12.26

4.3.3 Field emission scanning electron microscopy (FESEM) analysis

The micrographs of as-synthesized ferrite samples annealed at 650°C for 5 hours are displayed in Figure 4.27(a). The elemental proportions from the EDS spectra, which are shown in Figure 4.27(b), almost match the atomic percentage and weight percentage of each element, including O, Fe, Cu, Mn, and Al.

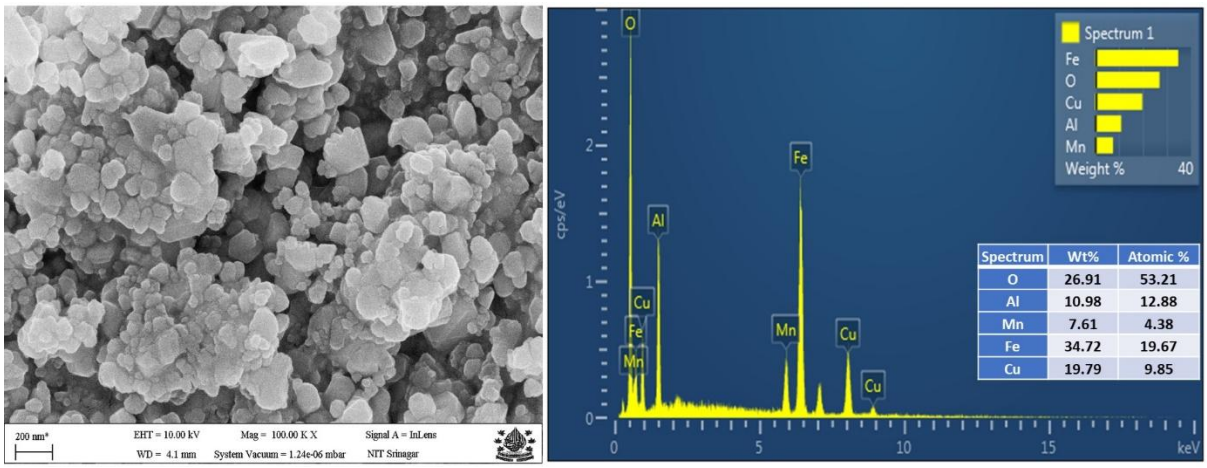

Figure 4.27: (a) SEM image (b) EDS of $Al_{0.5}Cu_{0.7}Mn_{0.3}Fe_{1.5}O_4$ ferrite.

4.3.4 Vibrating sample magnetometer (VSM) analysis

As-synthesized sample $Al_{0.5}Cu_{0.7}Mn_{0.3}Fe_{1.5}O_4$ annealed at 650°C, has a soft superparamagnetic feature in its magnetic hysteresis curve (Figure 4.28) [15, 16]. Table 4.15 shows the magnetic characteristics derived from room temperature VSM data. The M_s values of as-synthesized ferrites are 19.68, 8.03, 3.69, 3.40, and 1.62 emu/g respectively with varying values of 'x'.

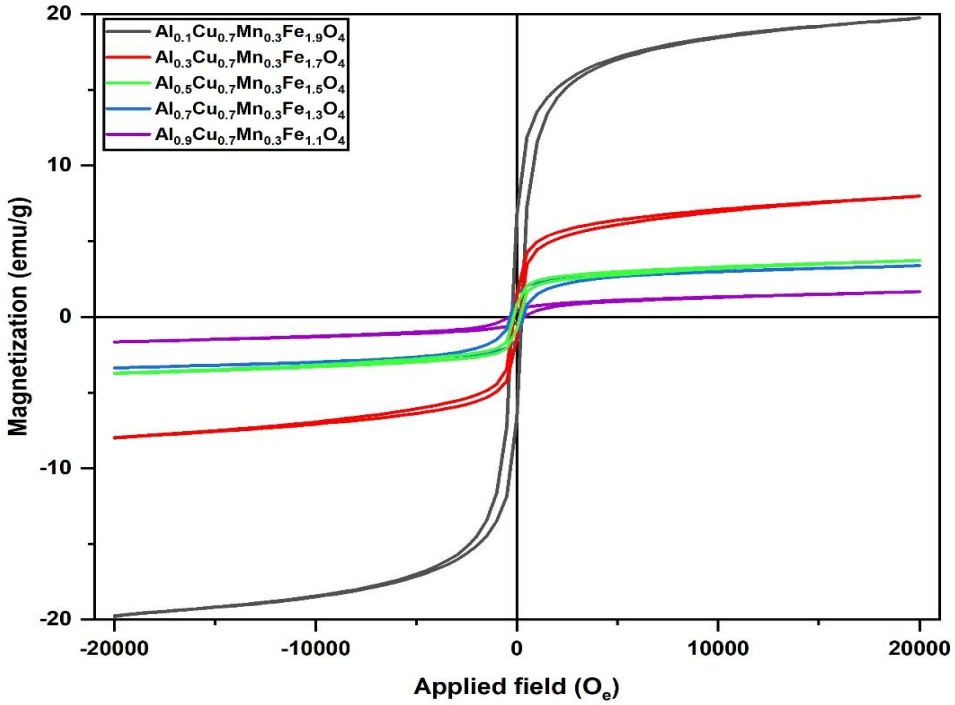

Figure 4.28: Hysteresis curves of $Al_xCu_{0.7}Mn_{0.3}Fe_{2-x}O_4$ ferrite at room temperature.

Table 4.15: Saturation magnetization (M_s), magnetic moment (μ_B), anisotropy constant (K), remanence (M_r), and coercivity (H_c) of $Al_xCu_{0.7}Mn_{0.3}Fe_{2-x}O_4$ ferrite annealed at 650°C for 5 hours.

Sample ($Al_xCu_{0.7}Mn_{0.3}Fe_{2-x}O_4$)	M_S (emu.g^{-1})	M_r (emu.g^{-1})	M_r/M_s	H_c (O_e)	μ_B	K×10^{-3} (emu.O_e g^{-1})
X = 0.1	19.68	7.09	0.36	252.19	0.823	5.169
X = 0.3	8.03	0.81	0.10	142.83	0.327	1.195
X = 0.5	3.69	1.40	0.37	163.45	0.147	0.629
X = 0.7	3.40	1.43	0.42	335.55	0.129	1.188
X = 0.9	1.62	0.38	0.23	372.30	0.061	0.631

4.3.5 Brunauer–Emmett–Teller (BET) analysis

The adsorption phenomenon is closely associated to specific surface area of the adsorbent, making it important physical qualitiy for the adsorption of adsorbate. The specific surface area of mixed spinel ferrite was determined using BET analysis, with the results shown in Figure 4.29. The BET average pore volume, surface area, and pore radius of mixed transition metal ferrite were 7.678 m^2/g, 0.1004 cc/g, and 17.001 A°, respectively.

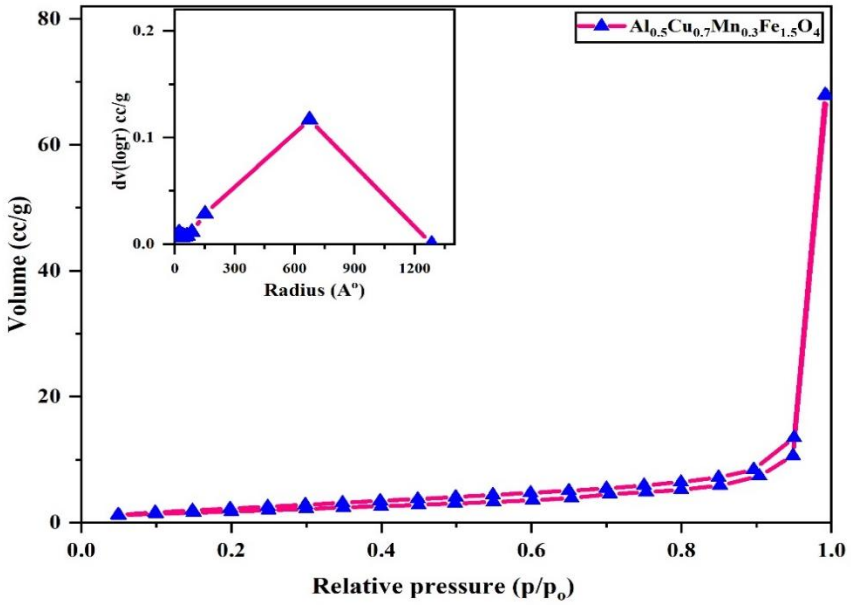

Figure 4.29: BET isotherm of $Al_{0.5}Cu_{0.7}Mn_{0.3}Fe_{1.5}O_4$ ferrite.

4.3.6 Adsorption study of dyes with Al-doped Cu-Mn ferrites

The potential of Al-doped mixed transition metal ferrite as an adsorbent for removing dyes (CV, CR, MO, and MB) from aqueous solutions is examined in this study [17, 18]. Fixed amount of ferrite (0.1g) was added to different concentrations of dye solutions for adsorption studies. Results from UV-visible spectrophotometic analysis are shown in figures 4.30-4.33 and related adsorption parameters displayed in table 4.16.

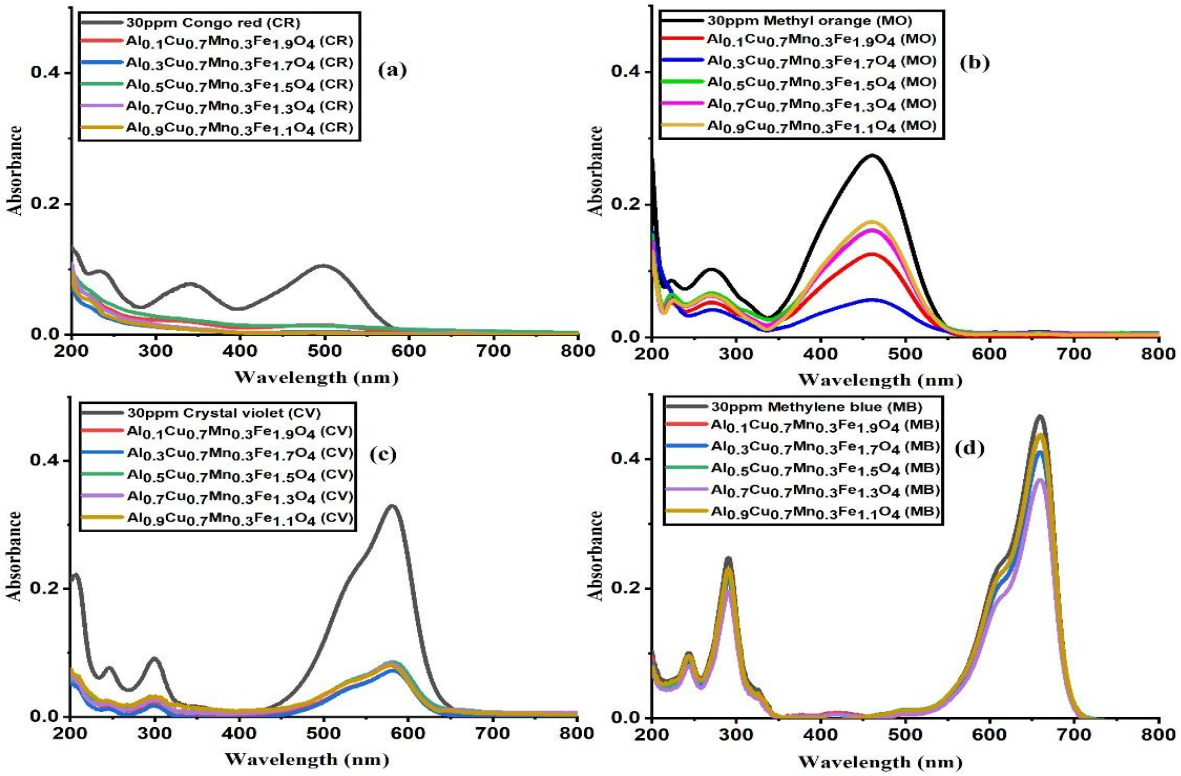

Figure 4.30: Spectra of UV-visible absorption of dyes solutions at 30 ppm.

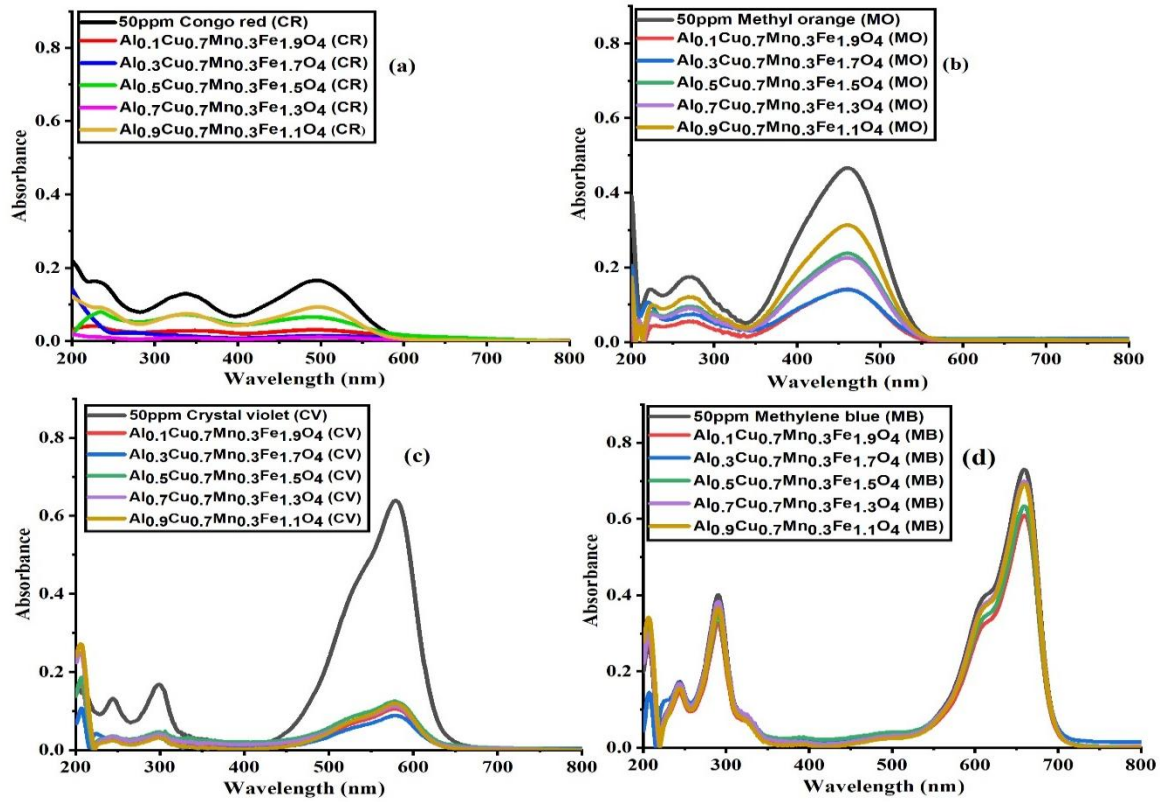

Figure 4.31: Spectra of UV-visible absorption of dyes solutions at 50 ppm.

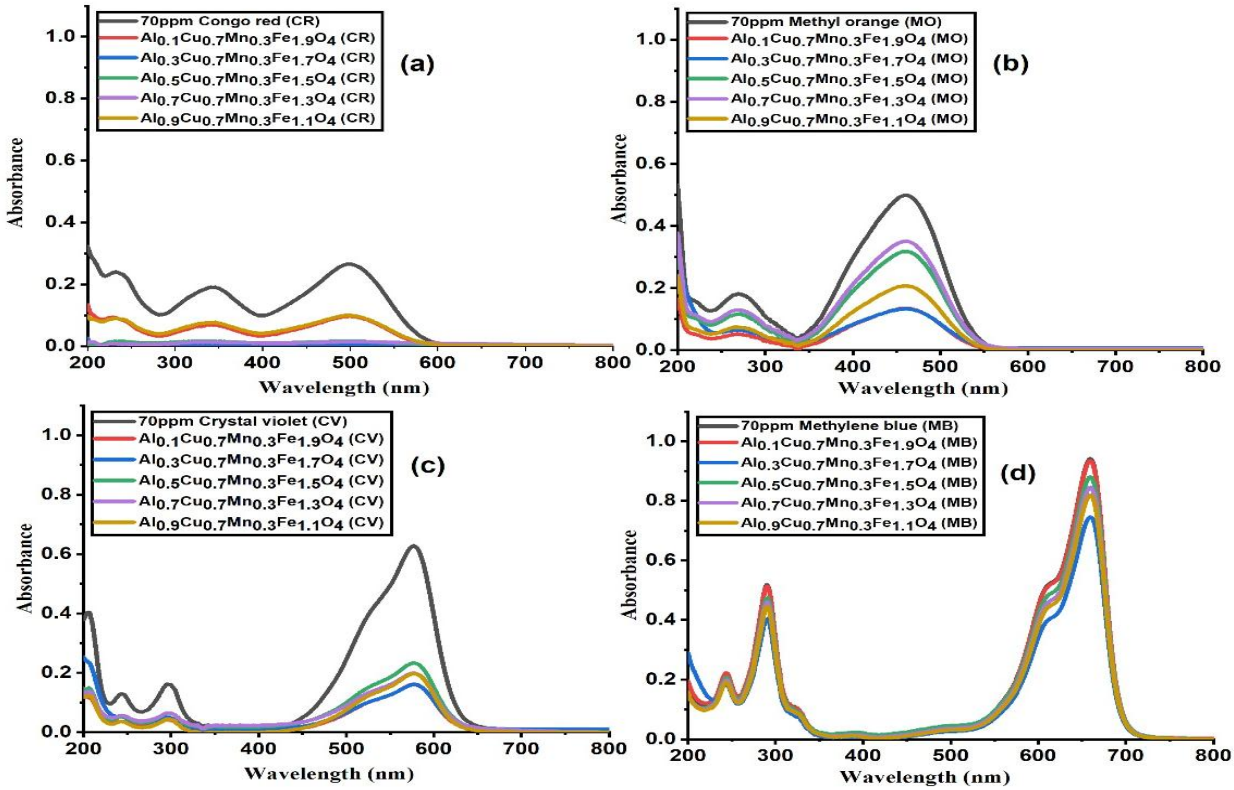

Figure 4.32: Spectra of UV-visible absorption of dyes solutions at 70 ppm.

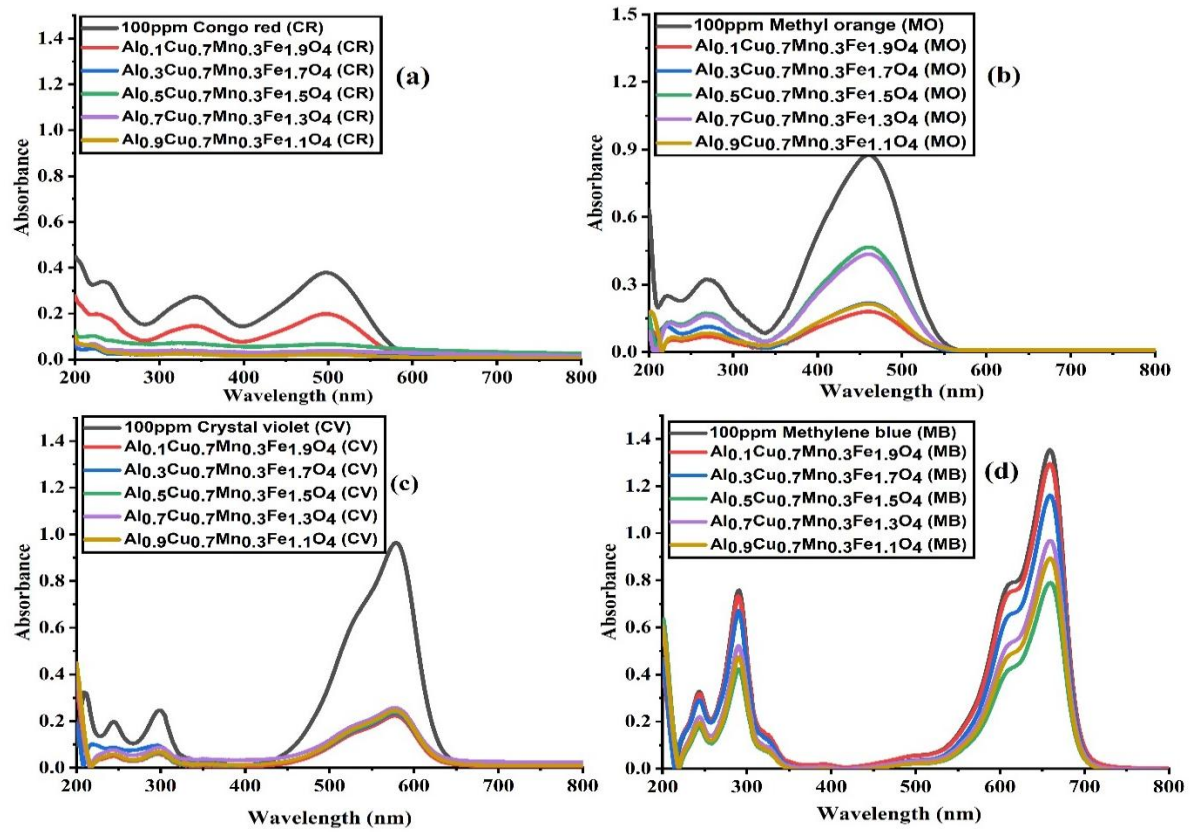

Figure 4.33: Spectra of UV-visible absorption of dyes solutions at 100 ppm.

Table 4.16: Percentage removal of different dye concentrations using Al-doped Cu-Mn ferrites

CONGO RED (CR)				
Adsorbent	**% removal of CR (30ppm)**	**% removal of CR (50ppm)**	**% removal of CR (70ppm)**	**% removal of CR (100ppm)**
$Al_{0.1}Cu_{0.7}Mn_{0.3}Fe_{1.9}O_4$	88.29	81.32	77.97	51.07
$Al_{0.3}Cu_{0.7}Mn_{0.3}Fe_{1.7}O_4$	98.93	90.96	89.53	82.76
$Al_{0.5}Cu_{0.7}Mn_{0.3}Fe_{1.5}O_4$	65.95	60.24	48.37	37.23
$Al_{0.7}Cu_{0.7}Mn_{0.3}Fe_{1.3}O_4$	51.06	43.37	53.42	29.53
$Al_{0.9}Cu_{0.7}Mn_{0.3}Fe_{1.1}O_4$	65.95	63.25	82.31	54.15
METHYL ORANGE (MO)				
Adsorbent	**% removal of MO (30ppm)**	**% removal of MO (50ppm)**	**% removal of MO (70ppm)**	**% removal of MO (100ppm)**
$Al_{0.1}Cu_{0.7}Mn_{0.3}Fe_{1.9}O_4$	54.37	69.67	72.94	85.58
$Al_{0.3}Cu_{0.7}Mn_{0.3}Fe_{1.7}O_4$	79.56	69.89	73.14	82.54
$Al_{0.5}Cu_{0.7}Mn_{0.3}Fe_{1.5}O_4$	40.87	49.03	36.27	62.67
$Al_{0.7}Cu_{0.7}Mn_{0.3}Fe_{1.3}O_4$	41.24	51.61	29.65	65.24
$Al_{0.9}Cu_{0.7}Mn_{0.3}Fe_{1.1}O_4$	36.49	32.68	58.51	82.86
CRYSTAL VIOLET (CV)				
Adsorbent	**% removal of CV (30ppm)**	**% removal of CV (50ppm)**	**% removal of CV (70ppm)**	**% removal of CV (100ppm)**
$Al_{0.1}Cu_{0.7}Mn_{0.3}Fe_{1.9}O_4$	74.27	83.56	74.15	76.86
$Al_{0.3}Cu_{0.7}Mn_{0.3}Fe_{1.7}O_4$	74.27	86.22	74.31	75.72
$Al_{0.5}Cu_{0.7}Mn_{0.3}Fe_{1.5}O_4$	67.63	80.59	62.76	75.10
$Al_{0.7}Cu_{0.7}Mn_{0.3}Fe_{1.3}O_4$	66.80	82.62	68.21	73.34
$Al_{0.9}Cu_{0.7}Mn_{0.3}Fe_{1.1}O_4$	68.46	81.37	68.37	74.68
METHYLENE BLUE (MB)				
Adsorbent	**% removal of MB 30PPM**	**% removal of MB 50PPM**	**% removal of MB 70PPM**	**% removal of MB 100PPM**
$Al_{0.1}Cu_{0.7}Mn_{0.3}Fe_{1.9}O_4$	26.50	16.57	0.74	4.36
$Al_{0.3}Cu_{0.7}Mn_{0.3}Fe_{1.7}O_4$	34.36	13.28	20.82	14.26
$Al_{0.5}Cu_{0.7}Mn_{0.3}Fe_{1.5}O_4$	26.91	13.15	6.48	41.68
$Al_{0.7}Cu_{0.7}Mn_{0.3}Fe_{1.3}O_4$	32.50	4.24	10.20	28.45
$Al_{0.9}Cu_{0.7}Mn_{0.3}Fe_{1.1}O_4$	18.63	5.20	13.07	33.99

4.3.7 Thermodynamic study

Standard enthalpy change (ΔH^o), standard Gibb's free energy change (ΔG^o) and standard entropy change (ΔS^o), for the dye adsorption process were calculated using the relevant equations. Variation of K_d with 1/T is shown in figure 4.34 and thermodynamic results are presented in table 4.17 A positive change for ΔH^o shows the endothermic nature of this process.

The positive change of ΔS^o indicates a rise in entropy during the dye adsorption process. The negative value for ΔG^o indicates spontaneity of the process, which further decreases with an increase in temperature. Increase in temperature favors this endothermic reaction. Positive change in enthalpy is attributed to the requirement of energy for breaking of bonds between dye molecules and water and diffusion of dye molecules through medium towards ferrite surface. Overall positive change in entropy is attributed to loss of hydration shell around dye molecules, which increases the entropy as compared to decrease in entropy due to adsorption of dye molecules on ferrite surface.

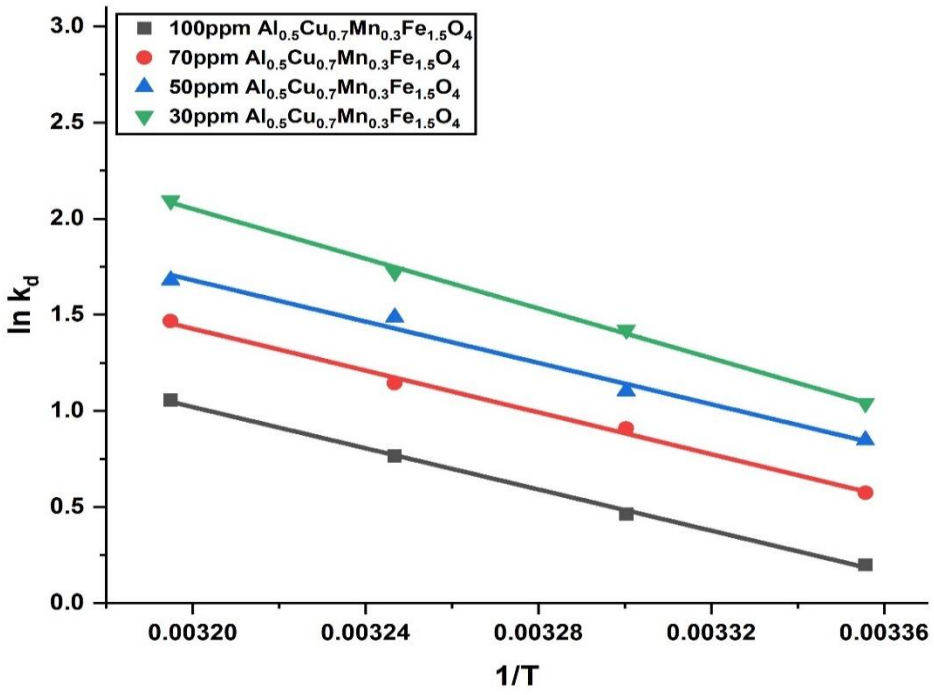

Figure 4.34: Adsorption thermodynamic parameters obtained from the linear connection between 1/T (inverse of Kelvin temperature) and ln K_d.

Table 4.17: Thermodynamic parameters for dye adsorption on Al-doped Cu-Mn ferrite.

Concentration(mg/L)/ Dye	Temperature (Kelvin)	ΔG^o (kJ/mol)	ΔH^o (kJ/mol)	ΔS^o (kJ/mol.K)
30mg/L (CR)	298	-2.573	53.78	0.189
	303	-3.581		
	308	-4.410		
	313	-5.449		
50mg/L (CR)	298	-2.101	44.71	0.157
	303	-2.777		
	308	-3.808		

	313	-4.372		
70mg/L (CR)	298 303 308 313	-1.418 -2.288 -2.927 -3.815	45.21	0.156
100mg/L (CR)	298 303 308 313	-0.493 -1.168 -1.958 -2.749	44.55	0.151

4.3.8 Adsorption isotherms

An adsorption isotherm describes the adsorptive capacity of an adsorbent that proves to be fundamental in designing an adsorption process [8]. The ferrite adsorption isotherms must be modelled to explain the interactions between the dyes and ferrites with distinct adsorption kinetics. In this study, Langmuir, Temkin, Freundlich, and Dubinin-Radushkevich isotherm models have been used for fitting of experimental data.

Figure 4.35 shows various adsorption isotherms for Al-doped Cu-Mn transition metal ferrite. The important parameters determined from these isotherms are given in Table 4.18. The Freundlich model provide a good match for dye adsorption, as demonstrated by the R^2 values. The fit of this model highlights non-ideal and heterogeneous surface adsorption, which is attributed to variation in adsorption capacity due to different energy sites. The value of empirical constant ‘n’ in the Freundlich isotherm was larger than unity, indicating favorable adsorption process. The comparison studies indicate that the mixed transition metal ferrites used in this study have good potential to remove the dyes. The results suggest that ferrite material might be a suitable alternative for removing CR dye [19].

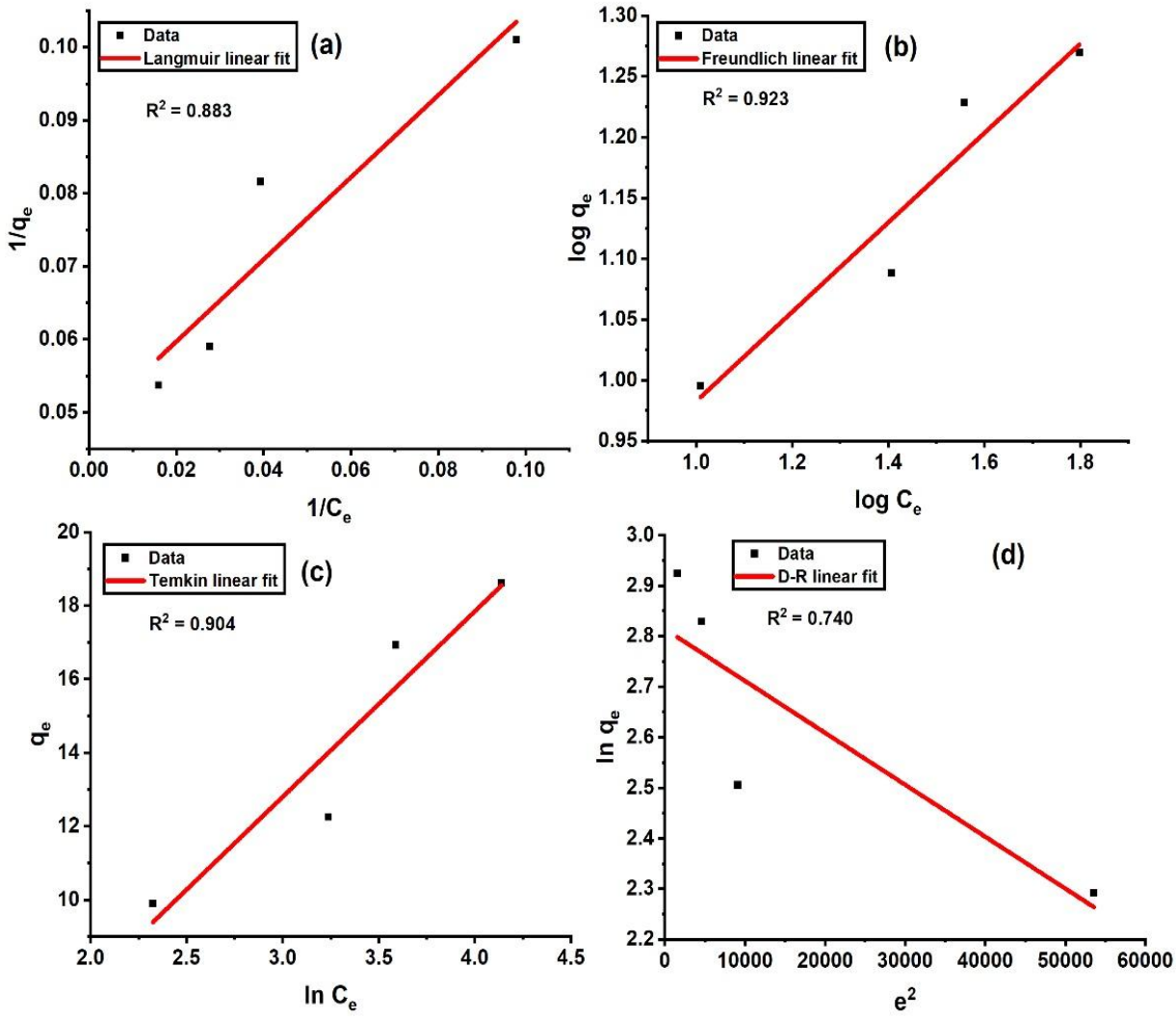

Figure 4.35: (a) Langmuir model (b) Freundlich model (c) Temkin model (d) D-R model.

Table 4.18: Adsorption isotherm parameters for Al-doped Cu-Mn mixed transition metal ferrite.

Adsorption isotherms parameters			
Langmuir model	Freundlich model	Temkin model	D-R model
q_{max} = 20.644	K_f = 4.118	B = 5.048	q_{max} =16.82
b = 0.00234	1/n = 0.367	A = 0.628	K =1.026
R^2 = 0.883	R^2 = 0.923	R^2 = 0.904	R^2 = 0.740
R_L =1	n= 2.717	b_t = 490.773	E_s = 0.698

4.3.9 Adsorption kinetics

Kinetic models and parameters are used to identify the nature of dye adsorption process from an aqueous solution. The PFO and the PSO Lagergren models were employed to fit the experimental results by using equations 12 and 13 [10].

$$\ln (q_e - q_t) = \ln q_e - k_1 t \qquad (12)$$

$$\frac{t}{q_t} = \frac{1}{k_2 q_e^2} + \frac{t}{q_e} \qquad (13)$$

The intercept and slope were used to calculate CR dye's adsorption capacity and first-order rate constants at various initial concentrations. Based on the linear plot of ln (q_e-q_t) against time (min), the values of the slope and intercept were calculated. Additionally, the adsorption process was given a kinetic explanation by fitting the PSO model to the experimental data. The second-order kinetic constants were determined by producing a linear plot of t/q_t vs. t (min). To find the coefficient of determination (R^2), PFO and PSO models were used to perform linear regression analysis. The values of R^2, indicating how well the model fits the adsorption system, are shown in Table 4.19. For the adsorption of dye pollutants in an aqueous solution, the R^2 for PSO kinetics was higher than that of PFO kinetics. Figure 4.36 shows the PFO and PSO kinetic modelling for the adsorption system. This data indicated that a PSO kinetic model effectively defined the adsorption of dye pollutants onto mixed spinel ferrite for CR dye.

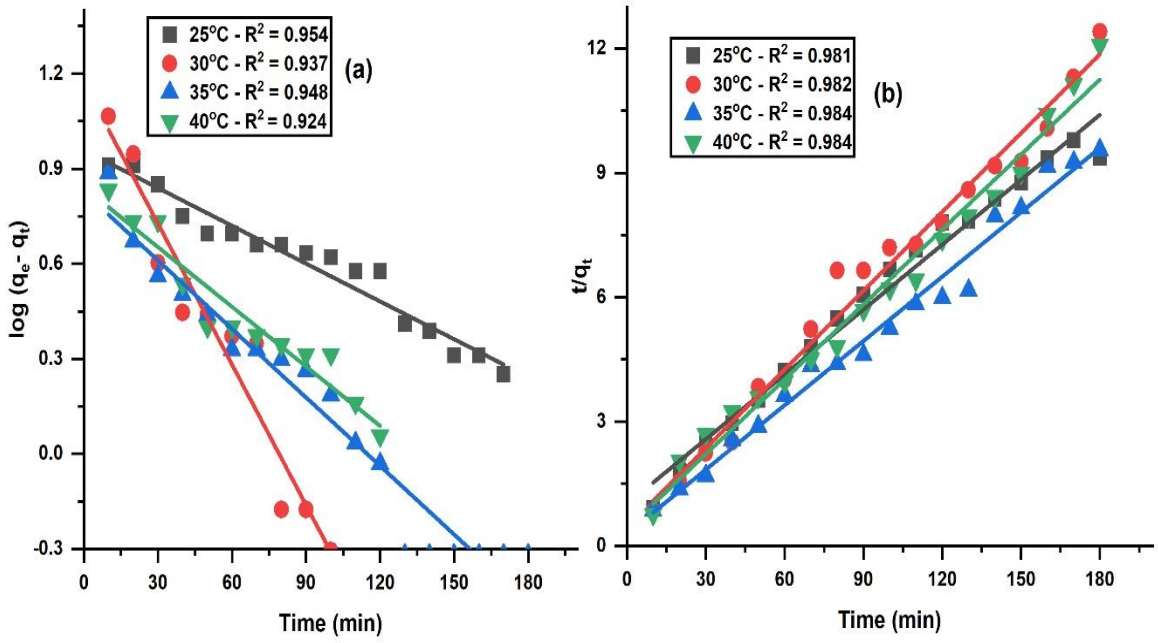

Figure 4.36: Model fitting of (a) PFO and (b) PSO for CR dye adsorption onto ($Al_{0.5}Cu_{0.7}Mn_{0.3}Fe_{1.5}O_4$) surface.

Table 4.19: Kinetic parameters of PFO and PSO adsorption kinetic models.

Dye/Adsorbent		**PFO**			**PSO**		
Congo Red ($Al_{0.5}Cu_{0.7}Mn_{0.3}Fe_{1.5}O_4$)	Temp. (°C)	Q_e (mg/g)	$k_1 \times 10^3$ (min^{-1})	R^2	Q_e (mg/g)	$k_2 \times 10^4$ (g/mg.min)	R^2
	25	2.67	4.4	0.954	19.23	26.93	0.981
	30	3.22	14.8	0.937	15.87	87.62	0.982
	35	2.28	7.2	0.948	19.30	94.15	0.984
	40	2.15	5.1	0.924	16.66	93.3	0.984

4.4 Al-doped Zn-Mn ferrite

4.4.1 Fourier transform infrared (FTIR) spectroscopy

Figure 4.37 illustrates the FTIR spectra of various Al-doped mixed transition metal ferrites, within 4000 cm^{-1} to 400 cm^{-1} range. The different absorption bands in the FTIR spectra of spinel ferrites show that the oxygen bonds are intrinsically stretched and vibrated with the metal cations. The metal-oxygen bond in the 300-450 cm^{-1} range, representing Fe^{3+}-O and Zn^{2+}-O bonds (M_{oct}-O) [20, 21], while the 500-650 cm^{-1} range, corresponding to the Mn^{2+}-O bond (M_{tet}-O) [22]. However, the stretching vibration occurring at approximately ~1400-1100 cm^{-1}, which is indicative of the Al^{3+}-O bond, is observable [2]. The observed absorption depends on the mass of the metal cation and the strength of the bonding between the oxygen and metal cation.

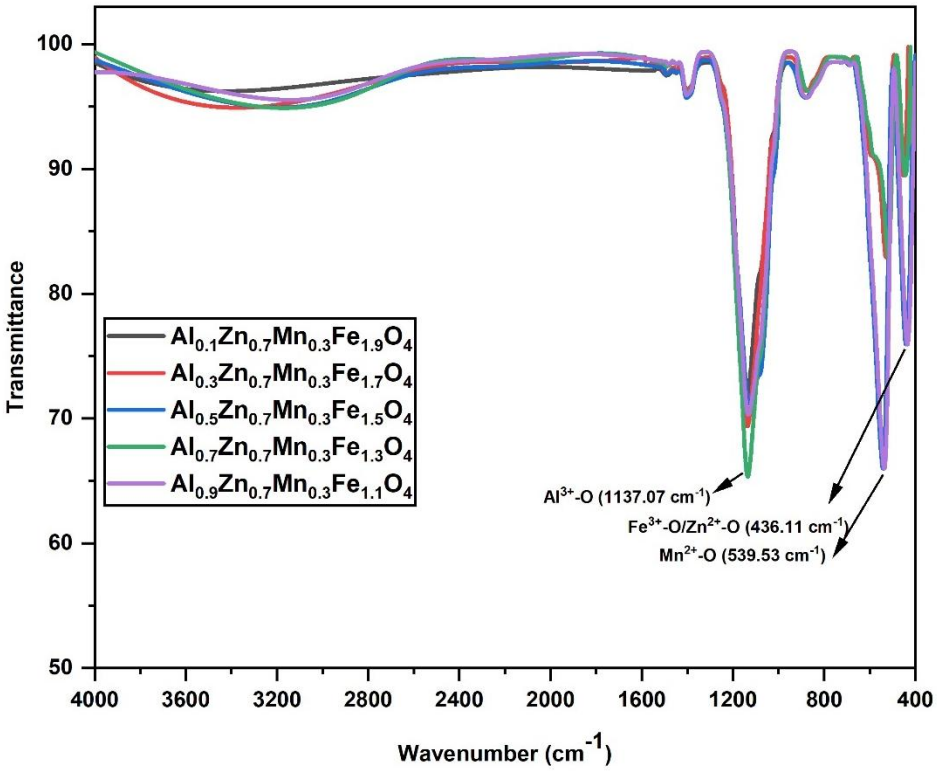

Figure 4.37: FTIR spectra of Al-doped Zn-Mn mixed transition metal ferrites.

4.4.2 X-ray powder diffraction (XRD) analysis

Figure 4.38 displays the XRD diffraction patterns of the mixed transition metal ferrite doped with aluminium. All the diffraction peaks confirmed the formation of a single spinel phase with a space group of Fd-3m. Diffraction peaks at 2θ of 25.57º, 31.06º, 33.2º, 35.6º, 40.6º 42.8º, 49.9º, 54.6º, 56.6º, 59.2º, 62.1º and 65.2º are in close agreement with the crystalline planes of 111, 200, 220, 300, 311, 400, 331, 422, 511, 333, 440 and 531 [20, 22] from the cubic system of material. The crystallite size of doped transition metal ferrites was calculated using Scherrer's equation.

$$D_{(hkl)} = \frac{K\lambda}{\beta cos\theta} \qquad (1)$$

Williamson and Hall (W-H) determined that the diffraction line broadens due to the crystallite size and strain contribution [23]. The following equation was used to calculate the strain-induced widening in powders due to distortion and defective crystals.

$$\varepsilon = \frac{\beta}{4tan\theta} \qquad (2)$$

These equations demonstrated that strain varies as tan θ and that the width of peak varies as 1/cosθ. At this point, the material's strain and crystallite size contributions may be multiplied to describe the total peak broadening.

$$\beta_{(hkl)} = \beta_{(D)} + \beta_{(\varepsilon)} \qquad (3)$$

The crystallite size and the stress/strain inside the material impact the X-ray spectra's line width are illustrated in Table 4.20. The Williamson-Hall analysis and the Scherrer equation are two key tools for calculating these effects. Smaller crystallites produce broader peaks, and strain produces broadening that changes with diffraction angle.

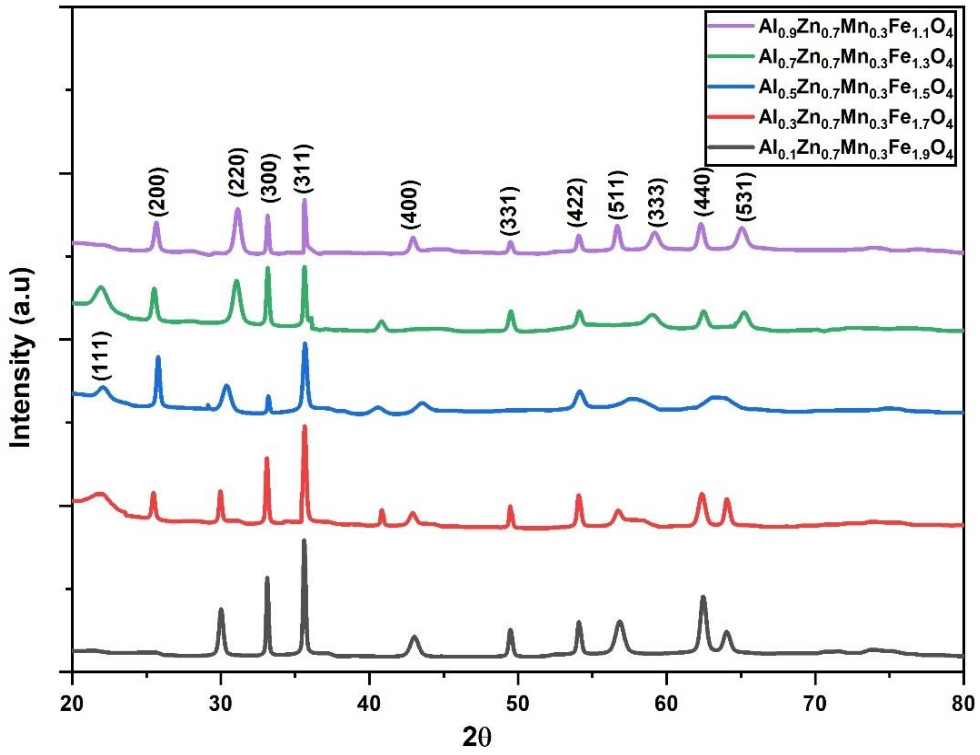

Figure 4.38: Powder XRD pattern of Al-doped Zn-Mn mixed transition metal ferrites.

Table 4.20: Al-doped ($Al_xZn_{0.7}Mn_{0.3}Fe_{2-x}O_4$) ferrites crystalline size and strain.

Ferrite ($Al_xZn_{0.7}Mn_{0.3}Fe_{2-x}O_4$)	**D(nm)**	**$\delta \times 10^{-3}$ (nm^{-2})**	**$\in \times 10^{-3}$**
X = 0.1	0.46	4696.68	222.68
X = 0.3	0.45	4895.54	226.81
X = 0.5	1.20	683.94	84.77
X = 0.7	2.14	218.09	46.31
X = 0.9	12.24	6.67	8.39

4.4.3 Field emission scanning electron microscopy (FESEM) analysis

FESEM is a technique used to examine the morphology of Al-doped mixed transition metal ferrite. Figures 4.39(a) and (b) represent the FESEM micrographs and EDS spectra of as-synthesized material. The FESEM images show the development of a spherical grain shape, while the EDS spectra show the elemental proportion closely aligned with the weight percentage and atomic percentage of all elements (Al, Zn, Mn, Fe, and O) according to stoichiometry.

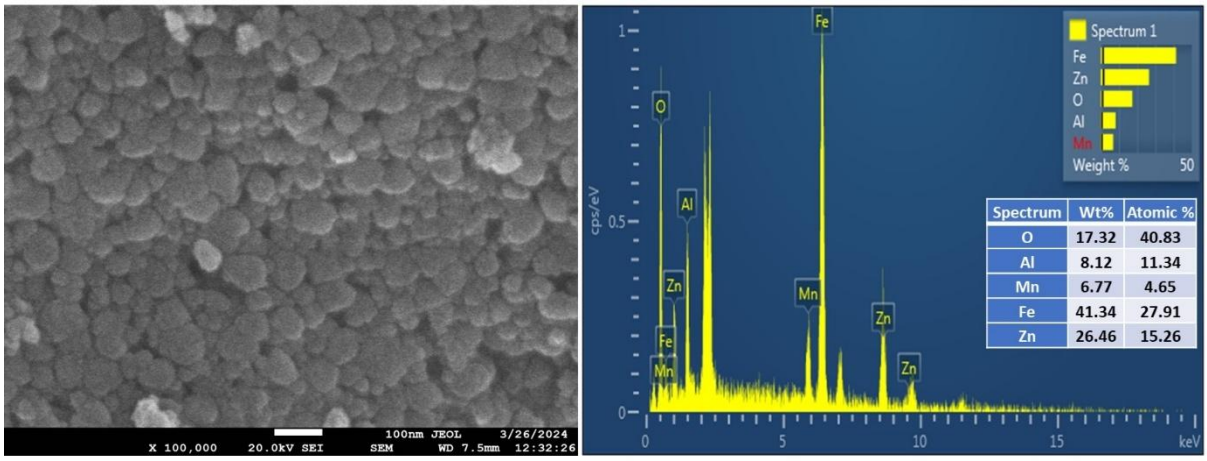

Figure 4.39: (a) SEM image (b) EDS of $Al_{0.5}Zn_{0.7}Mn_{0.3}Fe_{1.5}O_4$ ferrite.

4.4.4 Vibrating sample magnetometer (VSM) analysis

The magnetic property of the Al-doped Zn-Mn ferrite was specified by a VSM with the highest applied field of $\pm$20 kO_e at room temperature. Figure 4.40 displays the magnetization curves of Al-doped mixed transition metal ferrite. The results showed that the as-synthesized samples demonstrated superparamagnetic properties. The saturation magnetization values (M_s) of the as-synthesized ferrites were 17.95, 6.07, 5.13, 3.75, and 3.62 emu/g respectively. The anisotropy constant (K) and the experimental magnetic moment (μ_B) were calculated by using the following equation [4, 5].

$$\mu_B = \frac{MmMs}{5585} \quad (4)$$

$$H_C = \frac{0.96K}{Ms} \quad (5)$$

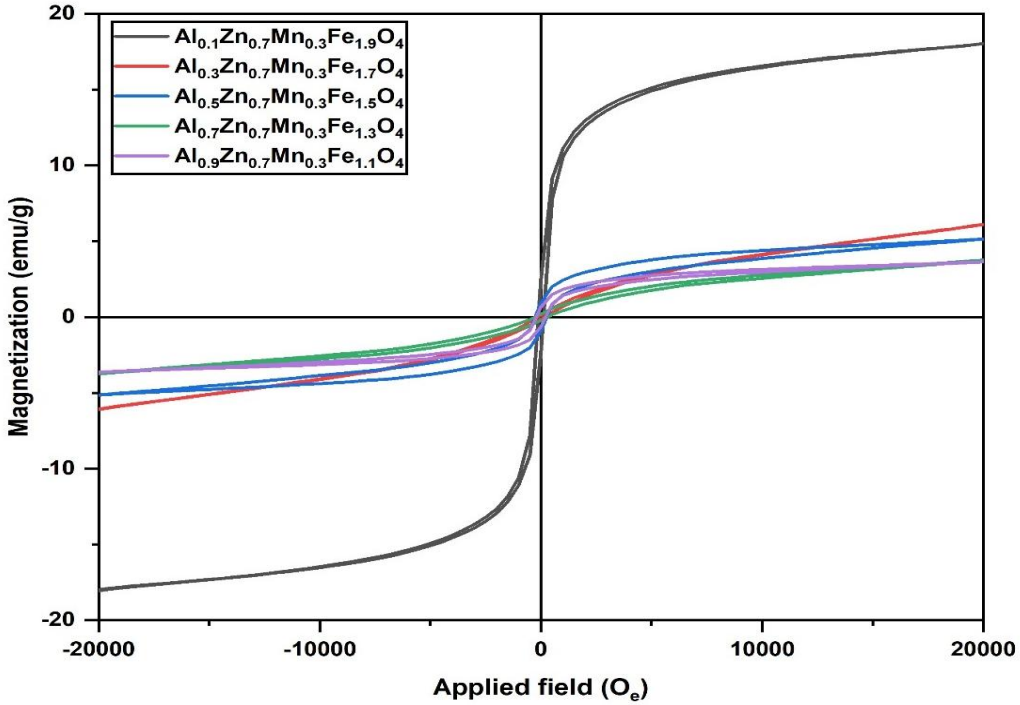

Figure 4.40: $Al_xZn_{0.7}Mn_{0.3}Fe_{2-x}O_4$ ferrite hysteresis curves at room temperature.

Table 4.21: $Al_xZn_{0.7}Mn_{0.3}Fe_{2-x}O_4$ ferrite's magnetic moment (μ_B), saturation magnetization (M_s), anisotropy constant (K), coercivity (H_c) and remanence (M_r) annealed at 650°C for 5 hours.

Sample ($Al_xZn_{0.7}Mn_{0.3}Fe_{2-x}O_4$)	M_S (emu.g^{-1})	M_r (emu.g^{-1})	M_r/M_s	H_c (O_e)	μ_B	K×10^{-3} (emu.O_e g^{-1})
X=0.1	17.95	2.41	0.13	116.5	0.75	2.17
X=0.3	6.07	0.14	0.02	166.6	0.24	1.05
X=0.5	5.13	0.91	0.17	265.0	0.20	1.41
X=0.7	3.75	0.21	0.05	270.5	0.14	1.05
X=0.9	3.62	0.64	0.17	210.3	0.13	0.79

4.4.5 Brunauer–Emmett–Teller (BET) analysis

Figure 4.41 displays the N_2 adsorption-desorption isotherm parameters from BET analysis. The sample's pore size distribution (average pore volume and pore radius) was assessed using the BJH plot which was found to be 0.157 cc/g, and 19.087 A° and the specific surface area determined by the BET technique was found to be 21.522 m^2/g.

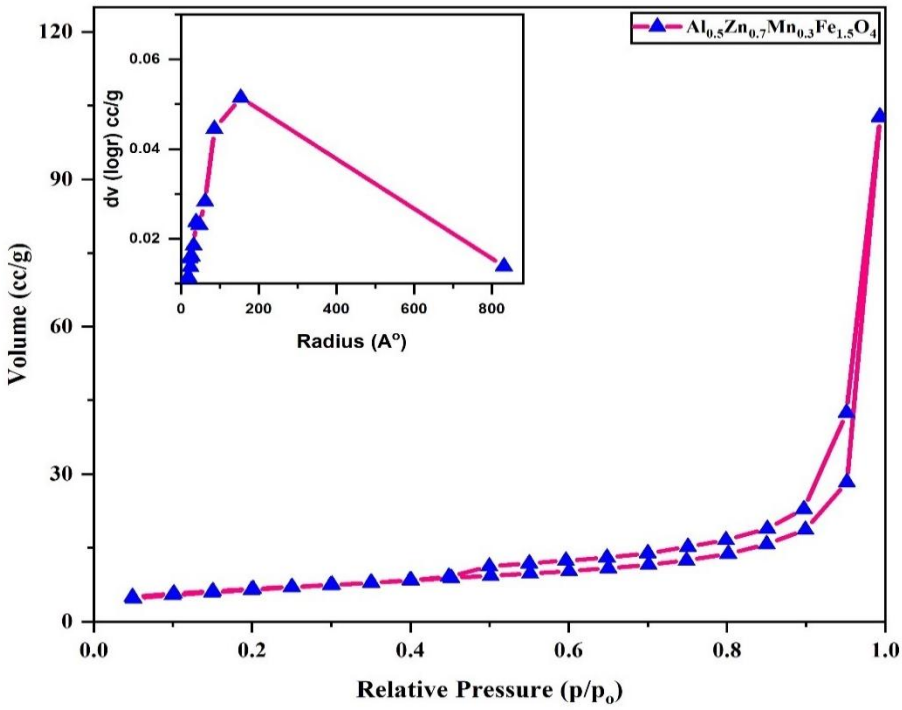

Figure 4.41: BET isotherm of $Al_{0.5}Zn_{0.7}Mn_{0.3}Fe_{1.5}O_4$ ferrite.

4.4.6 Adsorption study of dyes with Al-doped Zn-Mn ferrite

The effectiveness of the adsorbents in removing cationic and anionic dyes from an aqueous solution was determined through batch adsorption experiments. These experiments were carried out by taking different concentrations of dyes and fixed amount of adsorbent. After adsorption, the ferrite was separated from dye solution using a bar magnet, and then UV-visible spectrophotometer was employed to measure the residual concentration of dyes. The following equations were used to represent the adsorption parameters that characterize the rate of dye adsorption: (q_e) capacity of adsorption, (q_t) adsorption capacity at any time (t), and removal efficiency (sometimes referred to as percent dye removal) [24].

$$\text{Removal } (\%) = \frac{(C_0 - C_e)}{C_0} \times 100 \quad (6)$$

$$q_e = \frac{(C_0 - C_e)V}{m} \quad (7)$$

$$q_t = \frac{(C_0 - C_t)V}{m} \quad (8)$$

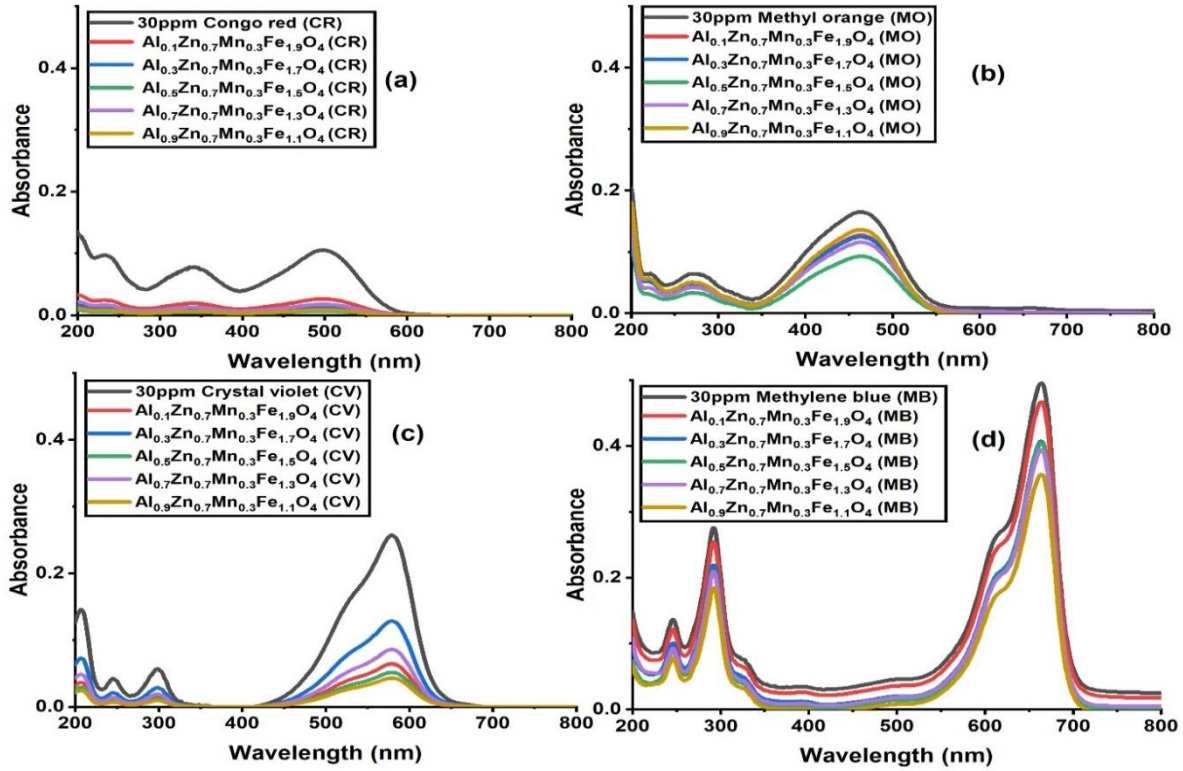

Figure 4.42: Spectra of UV-visible absorption of dyes solutions at 30 ppm.

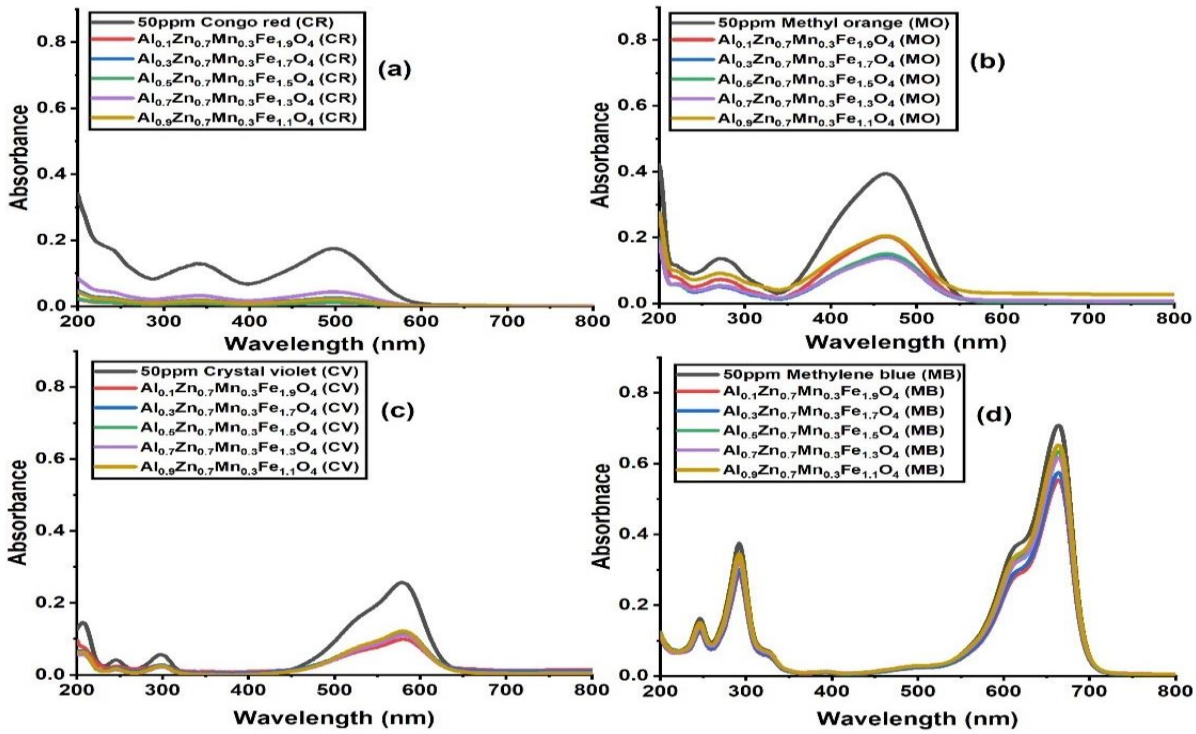

Figure 4.43: Spectra of UV-visible absorption of dyes solutions at 50 ppm.

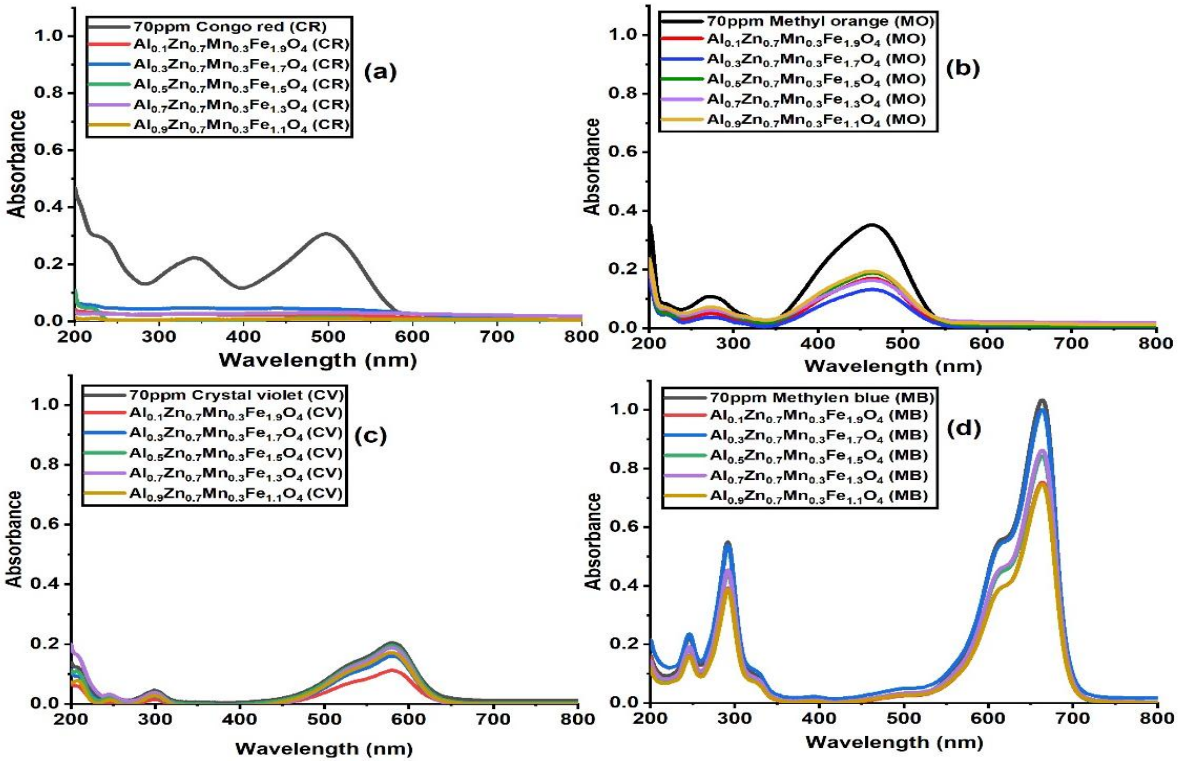

Figure 4.44: Spectra of UV-visible absorption of dyes solutions at 70 ppm.

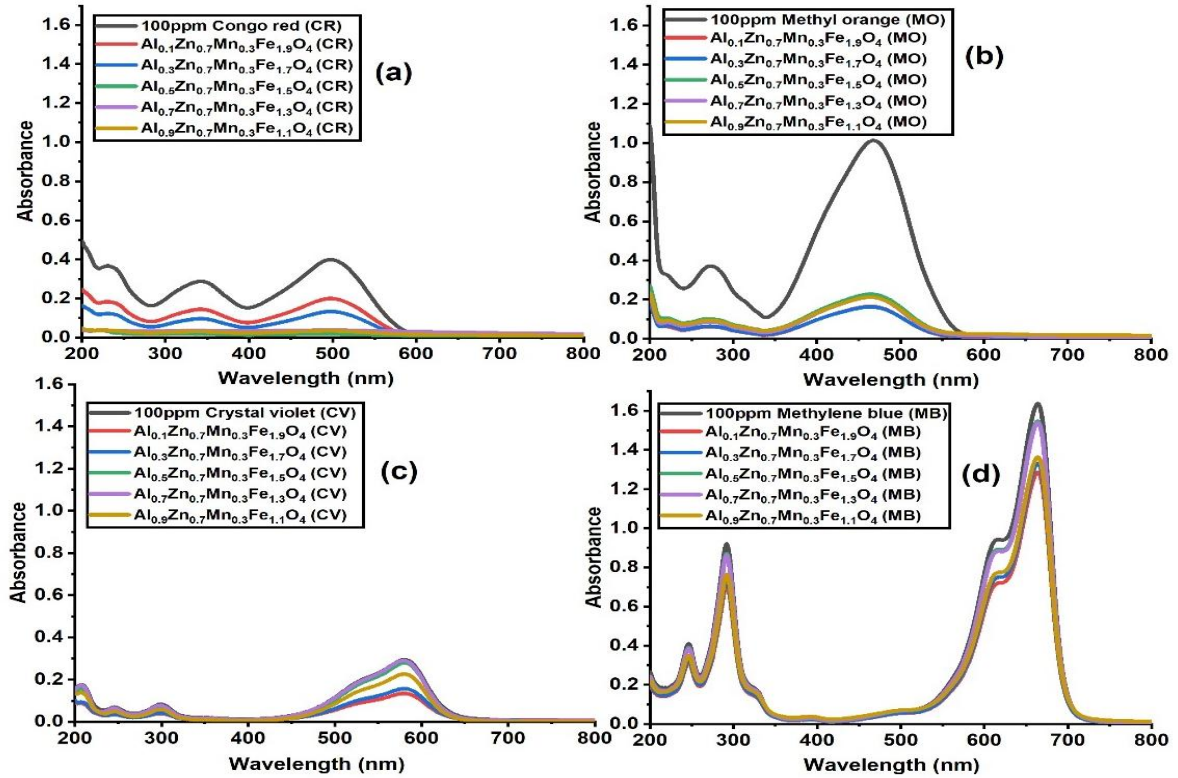

Figure 4.45: Spectra of UV-visible absorption of dyes solutions at 100 ppm.

Table 4.22: Percentage removal of various dye concentrations using Al-doped Zn-Mn mixed transition metal ferrites.

CONGO RED (CR)				
Adsorbent	**% removal of CR (30ppm)**	**% removal of CR (50ppm)**	**% removal of CR (70ppm)**	**% removal of CR (100ppm)**
$Al_{0.1}Zn_{0.7}Mn_{0.3}Fe_{1.9}O_4$	20.95	68.57	68.95	43.96
$Al_{0.3}Zn_{0.7}Mn_{0.3}Fe_{1.7}O_4$	50.47	89.54	78.75	33.41
$Al_{0.5}Zn_{0.7}Mn_{0.3}Fe_{1.5}O_4$	93.33	94.8	95.42	95.97
$Al_{0.7}Zn_{0.7}Mn_{0.3}Fe_{1.3}O_4$	68.57	82.85	80.06	53.26
$Al_{0.9}Zn_{0.7}Mn_{0.3}Fe_{1.1}O_4$	76.19	96.57	87.90	74.62
CRYSTAL VIOLET (CV)				
Adsorbent	**% removal of CV (30ppm)**	**% removal of CV (50ppm)**	**% removal of CV (70ppm)**	**% removal of CV (100ppm)**
$Al_{0.1}Zn_{0.7}Mn_{0.3}Fe_{1.9}O_4$	3.57	61.47	45.09	54.42
$Al_{0.3}Zn_{0.7}Mn_{0.3}Fe_{1.7}O_4$	16.07	52.91	21.56	46.59
$Al_{0.5}Zn_{0.7}Mn_{0.3}Fe_{1.5}O_4$	1.78	53.69	4.41	5.10
$Al_{0.7}Zn_{0.7}Mn_{0.3}Fe_{1.3}O_4$	58.92	57.19	7.84	1.36
$Al_{0.9}Zn_{0.7}Mn_{0.3}Fe_{1.1}O_4$	21.42	52.52	16.17	22.78
METHYL ORANGE (MO)				
Adsorbent	**% removal of MO (30ppm)**	**% removal of MO (50ppm)**	**% removal of MO (70ppm)**	**% removal of MO (100ppm)**
$Al_{0.1}Zn_{0.7}Mn_{0.3}Fe_{1.9}O_4$	23.03	48.47	51.70	83.71
$Al_{0.3}Zn_{0.7}Mn_{0.3}Fe_{1.7}O_4$	24.24	64.46	62.5	83.90
$Al_{0.5}Zn_{0.7}Mn_{0.3}Fe_{1.5}O_4$	43.63	61.67	46.59	77.49
$Al_{0.7}Zn_{0.7}Mn_{0.3}Fe_{1.3}O_4$	29.69	64.97	53.69	79.07
$Al_{0.9}Zn_{0.7}Mn_{0.3}Fe_{1.1}O_4$	17.57	47.96	44.88	79.07
METHYLENE BLUE (MB)				
Adsorbent	**% removal of MB (30ppm)**	**% removal of MB (50ppm)**	**% removal of MB (70ppm)**	**% removal of MB (100ppm)**
$Al_{0.1}Zn_{0.7}Mn_{0.3}Fe_{1.9}O_4$	5.84	21.86	27.14	21.48
$Al_{0.3}Zn_{0.7}Mn_{0.3}Fe_{1.7}O_4$	17.94	18.89	3.18	18.68
$Al_{0.5}Zn_{0.7}Mn_{0.3}Fe_{1.5}O_4$	18.54	10.43	18.55	5.49
$Al_{0.7}Zn_{0.7}Mn_{0.3}Fe_{1.3}O_4$	20.56	12.97	16.61	6.04
$Al_{0.9}Zn_{0.7}Mn_{0.3}Fe_{1.1}O_4$	28.02	7.89	27.82	16.72

4.4.7 Thermodynamic study

The nature of adsorption process was derived from the thermodynamic variables of adsorption by calculating change is Gibb's free energy, entropy and enthalpy. Figure 4.46 displays plot of K_d vs 1/T, which was used further to determine different thermodynamic parameters. Table 4.23 displays the results for thermodynamic parameters. With increase in temperature, the value

of ΔG^o further decreased, revealing that high temperatures were suitable for the adsorption process. When ΔH^o is positive, it means that heat is absorbed during the dye adsorption procedure. This suggests that in the dye removal condition, the interactions between the dye molecules and the surface of the ferrite are stronger. A positive change of ΔS^o reveals an increase in entropy throughout the dye-removal process, representing that the adsorption process promotes disorder or randomness. To understand thermodynamics of this adsorption process, adsorption of dye was carried out at different temperatures (298K, 303K, 308K, and 313K). The positive value of ΔH^o is attributed to breaking of bonds between water and dye molecules, and this required energy is absorbed from surroundings. Moreover, diffusion of dye molecules through medium towards the ferrite surface also requires energy.

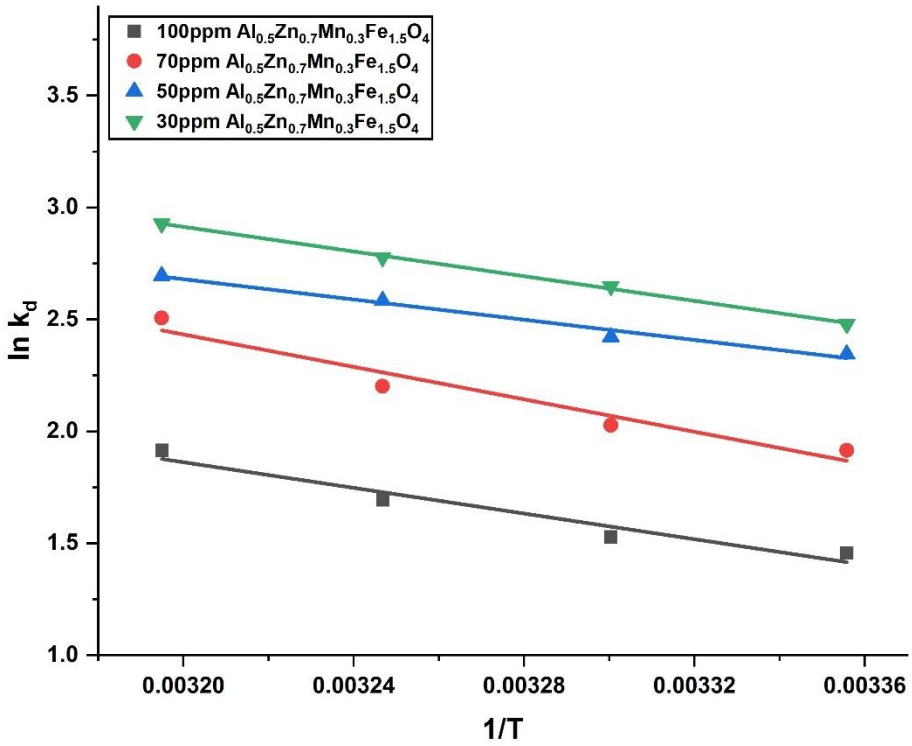

Figure 4.46: Plotting ln K_d vs 1/T determines the adsorption thermodynamic parameters.

Table 4.23: Thermodynamic parameters for dye adsorption on Al-doped Zn-Mn mixed transition metal ferrite ($Al_{0.5}Zn_{0.7}Mn_{0.3}Fe_{1.5}O_4$).

Concentration(mg/L)/ Dye	Temperature (Kelvin)	ΔG^o (KJ/mol)	ΔH^o (KJ/mol)	ΔS^o (KJ/mol/K)

30mg/L (CR)	298 303 308 313	-3.61 -3.74 -4.33 -4.98	22.92	0.09
50mg/L (CR)	298 303 308 313	-4.74 -5.10 -5.63 -6.52	18.80	0.08
70mg/L (CR)	298 303 308 313	-5.80 -6.10 -6.61 -7.01	30.12	0.11
100mg/L (CR)	298 303 308 313	-6.95 -7.21 -7.45 -7.75	23.82	0.09

4.4.8 Adsorption isotherms

An adsorbent's adsorptive capabilities are represented by its adsorption isotherm, which is essential for designing the adsorption process. Modelling adsorption isotherms is essential for explaining the interactions between the adsorbate and the adsorbent. To obtain a comprehensive understanding different isotherm models were employed to describe the $Al_{0.5}Zn_{0.7}Mn_{0.3}Fe_{1.5}O_4$/ CR dye system. To assess the credibility of related equations, $1/q_e$ vs$1/C_e$, q_e vs ln C_e, ln q_e vs e^2 and log q_e vs log C_e, a straight line is obtained in figure 4.45 (a, b, c and d). The relevant fitting results from different adsorption isotherms are presented in Table 4.24. The adsorption isotherms are well-fitted for the Freundlich isotherm, as evidenced by the R^2 (correlation coefficient) values, suggesting that the adsorbent's surface ($Al_{0.5}Zn_{0.7}Mn_{0.3}Fe_{1.5}O_4$) experienced heterogeneous adsorption of the CR dye. If $1/n = 0$, the process of adsorption is irreversible; otherwise, the method is beneficial if $0 < 1/n < 1$ [26]. When 1/n is found to be less than 1, effective adsorption is suggested. Al-doped transition metal ferrites have heterogeneous surface properties due to their crystalline structure, surface defects, and doping-induced changes. The fit of this model underscores the complexity of adsorption processes, highlighting non-ideal and heterogeneous surface adsorption resulting from variation in adsorption capacity due to different energy sites. Comparative analyses demonstrate the considerable potential of the mixed transition metal ferrite employed in this investigation for removal of CR dye.

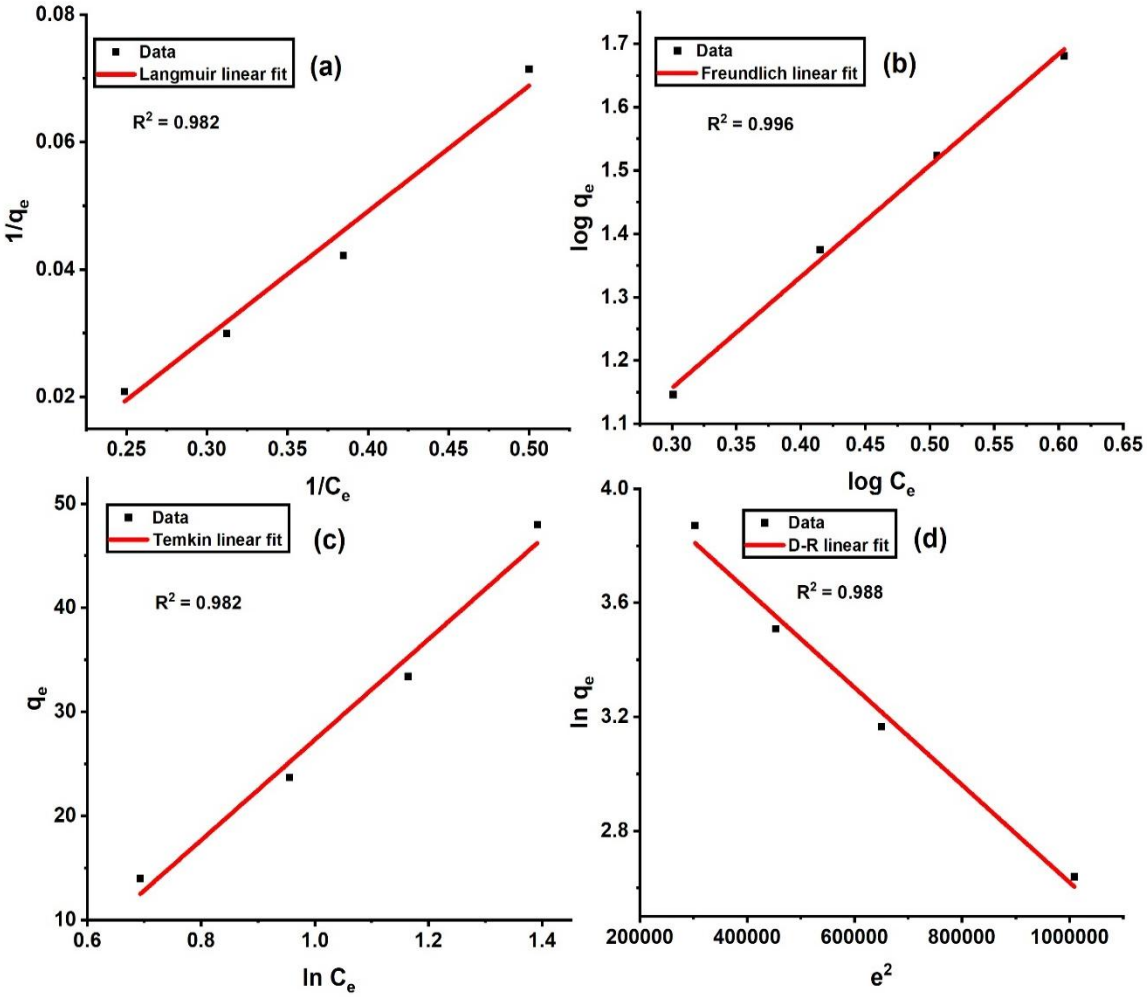

Figure 4.47: (a) Langmuir model (b) Freundlich model (c) Temkin model (d) D-R model.

Table 4.24: Adsorption isotherm parameters for Al-doped Zn-Mn mixed transition metal ferrite.

Adsorption isotherms parameters			
Langmuir model	Freundlich model	Temkin model	D-R model
q_{max} = 3.11	K_f = 4.25	B = 48.29	q_{max} =75.69
b = 9.70	1/n = 1.75	A = 0.648	K = 2
R^2 = 0.983	R^2 = 0.996	R^2 = 0.982	R^2 = 0.988
R_L =1	n= 0.568	b_t= 51.305	E_s = 0.5

4.4.9 Kinetics study of dye removal

Kinetic parameters are useful for estimating the rate of adsorption, as well as providing important data for developing and modelling the process. PFO and PSO models (equations 16-17) were employed to investigate kinetics of CR adsorption on the as-synthesized ferrites to completely understand the process of adsorption and kinetics [27].

$$\ln (q_e - q_t) = \ln q_e - k_1 t \qquad (16)$$

$$\frac{t}{q_t} = \frac{1}{k_2 q_e^2} + \frac{t}{q_e} \qquad (17)$$

Here qe and qt refers to quantity of dye adsorbed at equilibrium (mg/g) and at time 't'. Furthermore, k_1 and k_2 refer to rate constants for PFO and PSO kinetics respectively. The straight-line graphs of t/qt vs. time and ln (q_e-q_t) vs time are displayed in figures 4.46 (a) and (b), corresponding to the PFO and PSO kinetic models for different initial dye concentrations. Table 4.25 represents the corresponding adsorption rate constants. The computed data is displayed together with the reliability of each model examined by the correlation coefficient (R^2). The PSO kinetic model's correlation coefficient for adsorption of dye on Al-doped mixed transition metal ferrite was greater than that of the pseudo-first-order kinetic model. This PSO kinetic model suggests strong interactions between adsorbate molecules and adsorbent, which is equivalent to chemical-like nature due to strong electrostatic force of attraction.

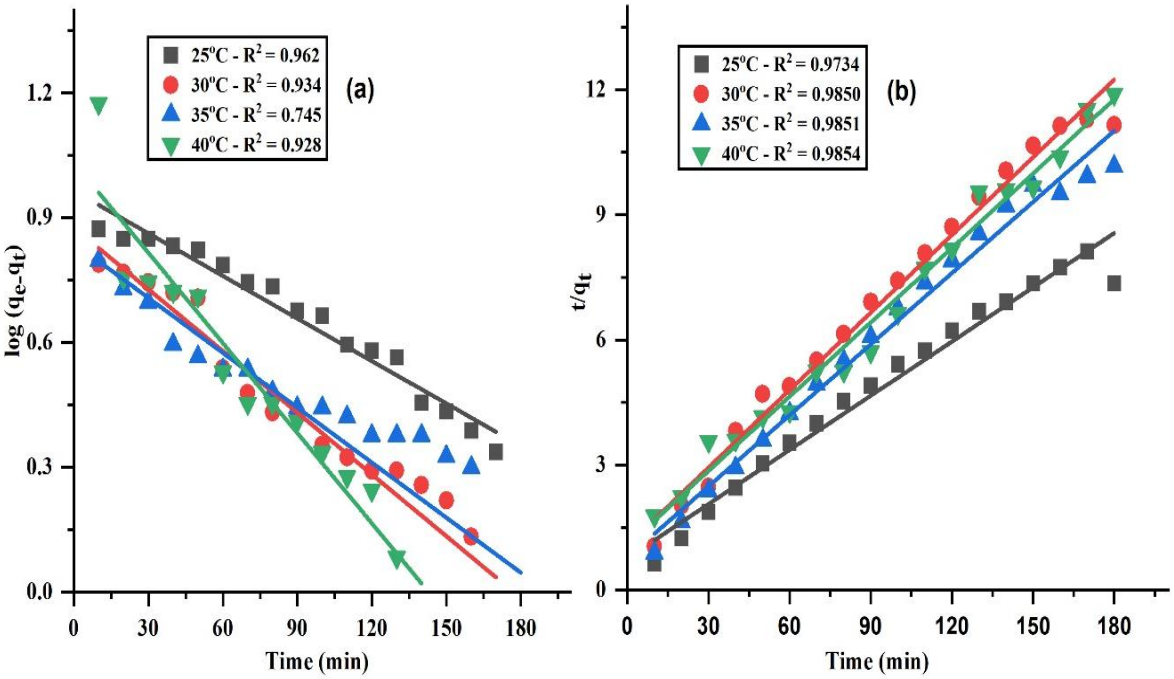

Figure 4.48: Model fitting for the adsorption of CR dye onto ($Al_{0.5}Zn_{0.7}Mn_{0.3}Fe_{1.5}O_4$) in pseudo-first order and pseudo-second order analysis.

Table 4.25: Kinetic parameters of PFO and PSO adsorption kinetic models.

Dye/Adsorbent		**PFO**			**PSO**		
Congo Red ($Al_{0.5}Zn_{0.7}Mn_{0.3}Fe_{1.5}O_4$)	Temp. (°C)	Q_e (mg/g)	$k_1\times10^3$ (min^{-1})	R^2	Q_e (mg/g)	$k_2\times10^4$ (g/mg.min)	R^2
	25	2.729	4.0	0.962	23.09	24.69	0.973
	30	2.401	4.8	0.934	16.12	35.72	0.9851
	35	2.228	3.8	0.745	17.57	41.40	0.9852
	40	2.646	6.2	0.928	16.83	32.86	0.9855

4.5 Adsorption mechanism of dyes with Al-doped mixed transition metal ferrite

In the current investigation, the significance of Al-doped mixed transition metal ferrite in adsorbing cationic and anionic dyes from aqueous solutions is presented. Thus, it becomes crucial to fully understand the adsorption mechanism employed by Al-doped mixed transition metal ferrites [28]. Figure 4.4.13 provides an overview of the comprehensive mechanism involving Al-doped mixed transition metal ferrite and their adsorption behavior towards different types of dyes in aqueous solutions. The transition metals are doped with aluminium ions that contain a variety of active sites including metal cations and oxygen vacancies on the surface of the Al-doped mixed transition metal ferrites. Metal cations (M^{2+} or M^{3+}) are positively charged ions, such as (Al^{3+}, Fe^{3+}, Ni^{2+}, Cu^{2+}, Co^{2+}, Zn^{2+} and Mn^{2+}), present on the ferrite material's surface. These metal cations can act as binding sites for dye molecules due to their positive charge, and oxygen vacancies at surface can create defects in the crystal structure, which may provide additional binding sites for molecules. These active sites on the surface of the Al-doped mixed transition metal ferrite play a crucial role in adsorption. When dye molecules are introduced into a solution containing the ferrite material, they can interact with these active sites through various mechanisms, including electrostatic interactions, chemical bonding, and surface complexation [29]. By providing more binding sites, these active sites enhance the adsorption capacity of the ferrite material for dye molecules. This increases the effectiveness of dye removal from aqueous solutions in treatments like dye remediation and wastewater treatment.

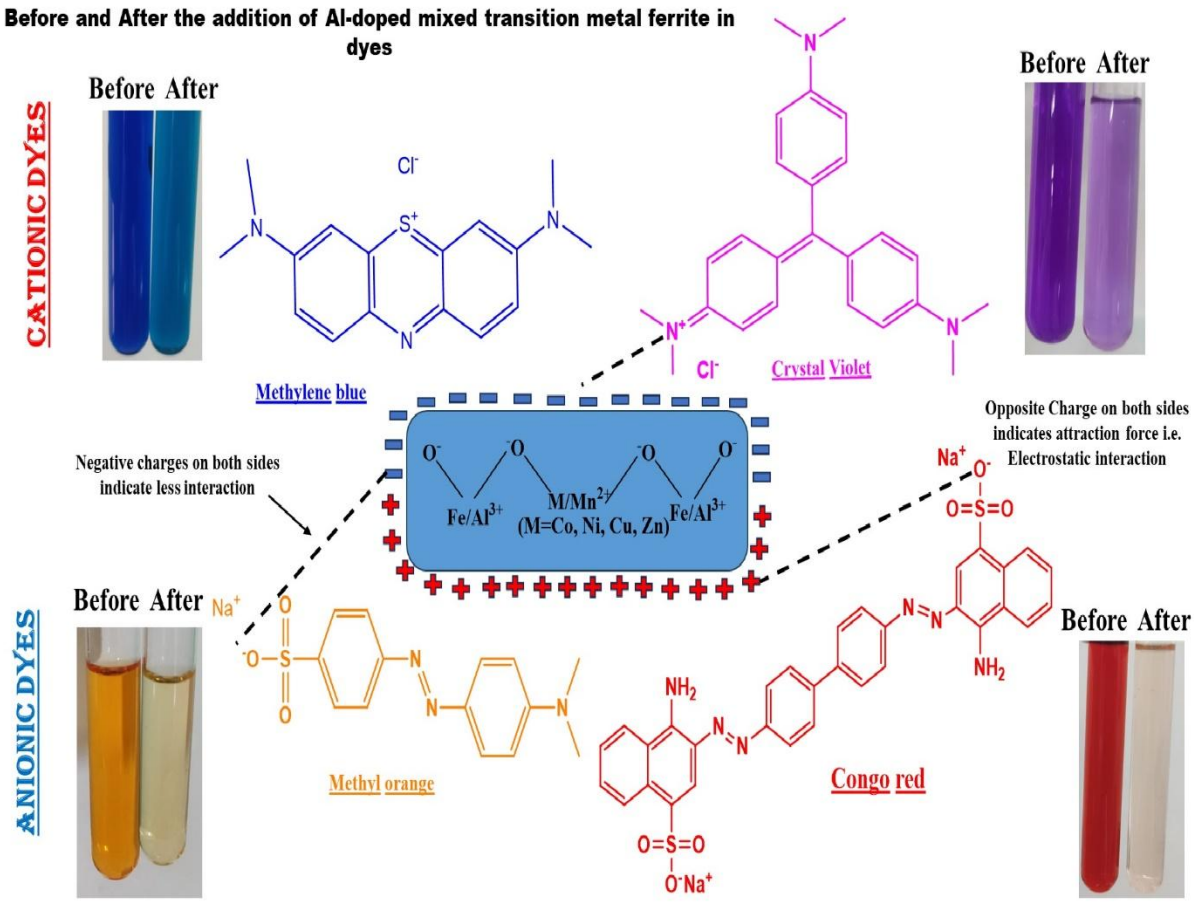

Figure 4.49: Adsorption mechanism of different dyes on the surface of Al-doped mixed transition metal ferrites.

References

1. Sarala E., Vinuth M., Madhukara Naik M. and Rami Reddy V.Y., Green synthesis of nickel ferrite nanoparticles using Terminalia catappa: Structural, magnetic and anticancer studies against MCF-7 cell lines, J. Hazard. Mat. Adv. 8, **2022**, 100150
2. Kadarisman K., Sriyono S., Abidin A., Lestari E., Marlina M., Saptiama I. and Setiawan H., Synthesis of nano-α-Al_2O_3 for ^{99}Mo adsorbent, At. Indon., 44(1), **2018,** 17-21.
3. Mozaffari M., Amighian J. and Darsheshdar E., Magnetic and structural studies of nickel-substituted cobalt ferrite nanoparticles, synthesized by the sol–gel method, J. Magn. Magn. Mater., 350, **2014,** 19-22.
4. Gayathri Manju B. and Raji P., Green Synthesis of Nickel–Copper Mixed Ferrite Nanoparticles: Structural, Optical, Magnetic, Electrochemical and Antibacterial Studies, J. Elect. Mater., 48(12), **2019,** 7710-7720.
5. Yadav R.S., Kuritika I., Vilcakova J., Urbanak P., Machovsky M., Masar M. and Holek M., Structural, magnetic, optical, dielectric, electrical, and modulus spectroscopic characteristics of $ZnFe_2O_4$ spinel ferrite nanoparticles synthesized via honey-mediated sol-gel combustion method, J. Phy. Chem. Solids, 110, **2017**, 87-99.
6. Noreen S., Mustafa G., Ibrahim S.M., Naz S., Iqbal M., Yaseen M., Javed T. and Nisar J., Iron oxide (Fe_2O_3) prepared via green route and adsorption efficiency evaluation for an anionic dye: kinetics, isotherms and thermodynamics studies, J. Mater. Res. Technol., 9(3), **2020**, 4206-4217.
7. Salman M., Athar M. and Farooq U., Biosorption of heavy metals from aqueous solutions using indigenous and modified lignocellulosic materials, Rev. Environ. Sci. Biotechnol., 14(2), **2015**, 211-228.
8. Divya J.M., Palak K. and Vairavel P., Optimization, kinetics, equilibrium isotherms, and thermodynamics studies of coomassie violet dye adsorption using azadirachta indica (Neem) leaf adsorbent, Desalination Water Treat., 190, **2020**, 353-382.
9. Shouman M.A., Khedr S.A.A., Removal of cationic dye from aqueous solutions modified acid-treated pomegranate peels (Punica Granatum) equilibrium and kinetic studies Asian J. Appl. Sci., 3(4), **2015**, 574-587.
10. Nistor M.A., Muntean S.G., Ianoș R., Racoviceanu R., Ianași C. and Cseh L., Adsorption of anionic dyes from wastewater onto magnetic nanocomposite powders synthesized by combustion method, Appl. Sci., 11(19), **2021**, 9236.

11. Bazhan Z., Ghodsi F.E. and Mazloom J., Surface morphology, optical, and electrochromic properties of nanostructured nickel ferrite ($NiFe_2O_4$) prepared by sol–gel method: effects of Ni/Fe molar ratios, Appl. Phys. A., 122, **2016**, 551.
12. Ahmed M.A., Ahmed M.A. and Mohamed A.A., Synthesis, characterization and application of chitosan/graphene oxide/copper ferrite nanocomposite for the adsorptive removal of anionic and cationic dyes from wastewater, RSC Adv., 13, **2023**, 5337-5352.
13. Deepty M., Srinivas C., Kumar E.R., Mohan N.K., Prajapat C.L., Rao T.V.C., Meena S.S., Verma A.K. and Sastry D.L., XRD, EDX, FTIR and ESR spectroscopic studies of co-precipitated Mn–substituted Zn–ferrite nanoparticles, Ceram. Int., 45(6), **2019**, 8037-8044.
14. Udhaya P.A., Ahmad A., Meena M., Queen M.A.J., Aravind M., Velusamy P., Almutairi T.M., Mohammed A.A.A. and Ali S., Copper ferrite nanoparticles synthesised using a novel green synthesis route: Structural development and photocatalytic activity, J. Mol. Struct., 1277, **2023**, 134807.
15. Vedrtnam A., Kalauni K., Dubey S. and Kumar A., A comprehensive study on structure, properties, synthesis and characterization of ferrites, AIMS Mat. Sci., 7(6), **2020**, 800-835.
16. Mahmoud M.H., Elshahawy A.M., Makhlouf S.A. and Hamdeh H.H., Mossbauer and magnetization studies of nickel ferrite nanoparticles synthesized by the microwave-combustion method, J. Mag Mag. Mater., 343, **2013**, 21-26.
17. Nizam T., Thomas M., Gerorge M. and Joseph A., Adsorption efficiency of sol–gel derived nano metal ferrites, MFe_2O_4 (M = Ni, Zn, Cu) on the removal of Cr (VI) ions from aqueous solution, J. Sol-gel Sci. Technol., 101, **2022**, 618-629.
18. Rápó E. and Tonk S., Factors Affecting Synthetic Dye Adsorption; Desorption Studies: A Review of Results from the Last Five Years (2017–2021), Molecules. 26(17), **2021**, 5419.
19. Ayoub M. and Dosanjh H.S., Synthesis and characterization of $Al_xCu_{0.7}Mn_{0.3}Fe_{2-x}O_4$ ferrite and its application in adsorption of dyes, J. Mol. Struct., 1321, **2024**, 140015.

20. Rameshbabu R., Ramesh R., Kanagesan S., Karthigeyan A. and Ponnusamy S. Synthesis and study of structural, morphological and magnetic properties of ZnFe2O4 nanoparticles, J. Supercond. Nov. Magn., 27(6), **2014**, 1499-1502.
21. Rameshbabu R., Ramesh R., Kanagesan S., Karthigeyan A. and Ponnusamy S., Synthesis and study of structural, morphological and magnetic properties of $ZnFe_2O_4$ nanoparticles, J. Supercond. Novel Magn., 27, **2014**, 1499-1502.
22. Gupta M., Tyagi S. and Kumari N., Electrochemical evaluation of highly stable Mn ferrite/PEDOT/rGO ternary nanocomposite for supercapacitor electrodes. J. Mater. Sci.: Mater. Electron., 33(10), **2022**, 7838-7852.
23. Bindu P. and Thomas S., Estimation of lattice strain in ZnO nanoparticles: X-ray peak profile analysis, J. Theor. Appl. Phys., 8(4), **2014**, 123-134.
24. Li P., Yang C., Wang Y., Su W., Wei Y. and Wu W., Adsorption Studies on the Removal of Anionic and Cationic Dyes from Aqueous Solutions Using Discarded Masks and Lignin, Molecules, 28(8), **2023**, 3349.
25. Din M.I., Hussain Z., Mirza M.L., Shah A.T. and Athar M.M., Adsorption optimization of Lead (II) using saccharum bengalense as a non-conventional low-cost biosorbent: isotherm and thermodynamics modeling, Int. J. Phytoremediation, 16(9), **2014**, 889-908.
26. Hamadeen H.M., Elkhatib E.A. and Moharem M.L., Optimization and mechanisms of rapid adsorptive removal of chromium (VI) from wastewater using industrial waste-derived nanoparticles, Sci. Rep., 12, **2022**, 1-12.
27. Niu Z., Feng W., Huang H., Wang B., Chen L., Miao Y. and Su S., Green synthesis of a novel Mn–Zn ferrite/biochar composite from waste batteries and pine sawdust for Pb^{2+} removal, Chemosphere, 252, **2020**, 126529.
28. Gao H.J, Wang S.F., Fang L.M., Sun G.A, Chen X.P., Tang S.N., Yang H., Sun G.Z. and Li D.F., Nanostructured spinel-type M (M = Mg, Co, Zn)Cr_2O_4 oxides: novel adsorbents for aqueous Congo red removal, Mater. Today Chem. 22, **2021**, 100593.
29. Wang S., Liu H., Li M., Han M., Gao H., Yang H., Fang L., Zhang H., Jagadeesha A.V., Manjunatha S.O., Cai C. and Li D., Various carbon-based $MgAl_2O_4$ adsorbents and their removal efficiency of CR dye and antibiotics in aqueous media: High selective adsorption capacity, performance prediction and mechanism insight, Ceram. Int, 49(16), **2023,** 26734-26746.

Chapter 5:

SUMMARY AND CONCLUSION

The present research work involves the preparation of Al-doped mixed transition metal ferrites ($Al_xM_{0.7}Mn_{0.3}Fe_{2-x}O_4$, where M = Co, Ni, Cu and Zn and x = 0.1, 0.3, 0.5, 0.7 and 0.9) through solution combustion method and their potential use as adsorbents for removing various dyes (congo red, methyl orange, crystal violet, and methylene blue) from aqueous solutions. Various physiochemical techniques, including Fourier transform infrared spectroscopy (FTIR), X-ray powder diffractometer (XRD), scanning electron microscopy with energy dispersive spectra (SEM-EDS) analysis, vibrating sample magnetometer (VSM), and Brunauer-Emmett-Teller (BET), were used to study the functional groups, crystallite size, surface morphology, magnetic properties, and surface area of as-synthesised ferrite respectively. The significant conclusions of this study are given below.

- FTIR spectra of as-synthesized ferrites containing three absorption bands characterize intrinsic stretching vibrations of the oxygen bonds with different metal cations. The absorption bands in the range of 300-450 cm^{-1} are due to metal-oxygen bonds at octahedral sites, while the absorption bands in the range 500-650 cm^{-1} are due to metal-oxygen bonds at tetrahedral sites. Absorption bands at higher wavenumber (tetrahedral sites) and lower wavenumber (octahedral sites) are attributed to metal-oxygen bond length and bond strength in spinel structure. Shorter and stronger bonds vibrate at high-energy vibrations, thus corresponding to the absorption at higher wavenumber. Moreover, another absorption band is observed around ~1400–1100 cm^{-1}, which is attributed to the presence of the Al^{3+}-O bond. The occurrence of all these absorption bands in FTIR spectra confirmed the presence of Al-doped mixed transition metal ferrites.
- XRD analysis has been carried out to determine crystallite size, purity, and lattice parameters for Al-doped mixed transition metal ferrites. The crystallite size of different Al-doped mixed transition metal ferrites from the Scherrer equation were found to be in nanoscale range as Co-Mn ferrite (1.58 nm to 8.36 nm), Ni-Mn ferrite (0.22 to 5.31 nm), Cu-Mn ferrite (1.50 to 8.39 nm) and Zn-Mn ferrite (0.46 to 12.24 nm) respectively. From the results, it was observed that with increase in the concentration of aluminium the crystallite size increases, but the strain of as-synthesized ferrites decreases. The increase in crystallite size with higher concentrations of Al-doping in ferrites can be attributed to bond strength, cation distribution, and lattice distortion reduction. When Al^{3+} replaces Fe^{3+} in the lattice, it can reduce lattice strain and distortion. This decrease in strain can promote better crystal growth, leading to larger crystallites. Al^{3+} may also

alter the cation distribution between tetrahedral and octahedral sites. This redistribution enhances structural stability, which facilitates the growth of larger crystallites. Smaller crystallite size generally leads to a larger surface area, Since, adsorption typically occurs on the material's surface. The large surface area provides more active sites for adsorption, enhancing the material's capacity. A larger strain value typically causes greater broadening of the diffraction peaks in a doped ferrite system. Strain broadening is due to lattice distortions, which separate the contributions of strain and crystallite size to peak broadening. When a material is under strain (e.g., due to dislocations, defects, or stress), the d-spacing of the crystal planes varies locally.

- FESEM-EDS analysis provides detailed information about surface morphology, grain size, and microstructures of ferrites. It shows the development of a spherical and irregular shape of Al-doped mixed transition metal ferrites. EDS spectra confirmed the elemental proportions closely aligned with weight percentage (wt.%) and atomic percentage (at. %) of all elements (Al, Co, Ni, Cu, Zn, Mn, Fe, and O) according to stoichiometry.
- BET analysis was used to analyze porosity and specific surface area in Al-doped mixed transition metal ferrites. From the results, the surface area values of as-synthesized ferrite (Co-Mn, Ni-Mn, Cu-Mn and Zn-Mn) are 12.779 m^2/g, 23.331 m^2/g**,** 7.678 m^2/g, and 21.522 m^2/g respectively, and the pore volumes are observed as 0.291 cc/g, 0.234 cc/g, 0.1004 cc/g, and 0.157 cc/g respectively. In addition to that the pore radius from the BET results were noted as 15.425 A°, 15.248 A°, 17.001 A°, and 19.087 A° respectively. From these results, it was observed that Al-doped Ni-Mn ferrites show high surface to volume ratio in comparison to other Al-doped mixed transition metal ferrites. As adsorbent's surface area is crucial physical characteristic for the adsorption process, a larger surface area generally corresponds to higher adsorption. The surface areas of these ferrites follow the order Ni-Mn > Zn-Mn > Co-Mn > Cu-Mn, which are in agreement with adsorption capacities of these ferrite materials.
- VSM analysis has been carried out to study and quantify the magnetic properties of these materials, such as saturation magnetization (M_s), coercivity (H_c), magnetic moment (μ_B), anisotropy constant (K), and remanent magnetization (M_r). The saturation magnetization values obtained from VSM analysis revealed important information about the magnetic content and particle size distribution. The decrease in saturation magnetization (M_s) with increase in Al doping in ferrites can be attributed to

the structural and magnetic effects introduced by the substitution of Al^{3+} ions for Fe^{3+} ions in the spinel lattice. When Al^{3+} ions replace Fe^{3+} ions, it reduces the overall magnetic contribution from the lattice. In spinel ferrites, the magnetic properties arise from the super exchange interactions between Fe^{3+} ions at tetrahedral and octahedral sites, and the magnetic moment at these sites. The overall magnetic moment per formula unit decreases with increasing Al content due to the progressive replacement of magnetic Fe^{3+} ions by non-magnetic Al^{3+} ions. A higher saturation magnetization may indicate the presence of more magnetic domains and larger particles, which may lower the available surface area for adsorption. Coercivity results revealed the soft magnetic behaviour of Al-doped mixed transition metal ferrites. Magnetic nature of synthesized ferrites aid in easy removal of these materials from aqueous solutions after adsorption process.

5.1 Adsorption of dyes using Al-doped mixed transition metal ferrites

- In the present study, Al-doped mixed transition metal ferrites were employed as such for the removal of dyes (CR, MO, CV and MB) from aqueous solutions. Al-doped Ni-Mn ferrites have shown high percentage removal efficiency (up to 98 percent) towards dyes in comparison to other ferrite materials. This higher efficiency is attributed to more magnitude of interactions between adsorbate and adsorbent, owing to high surface to volume ration of Al-doped Ni-Mn ferrite. All these ferrite materials have shown higher adsorption capacity for CR dye in comparison to other dyes, which is attributed to greater electrostatic interactions between positive charges at ferrite surface and negative charge on CR anionic dye.
- To understand thermodynamics of this adsorption process, adsorption of dye was carried out at different temperatures (298K, 303K, 308K, and 313K). Positive values of ΔH^o indicated the endothermic nature of this adsorption process. The positive value of ΔH^o is attributed to following factors:
  (i) Adsorption of dye molecules on ferrite surface proceed by breaking of bonds between dye molecules and water, which requires energy, and this energy is absorbed from the surroundings.
  (ii) Diffusion of dye molecules through medium towards the ferrite surface also requires energy.
  (iii) With increase in temperature adsorption process became more favorable, indicating endothermic nature of the process. At high temperature, the mobility

of dye molecules increases, facilitating their detachment from the water molecule and bonding with the adsorbent's surface.

Positive value of ΔS^o results from overall increase in degree of randomness in the system. Although, adsorption of dye molecules from the solution to ferrite surface decreases entropy, however, when the dye molecules are in dissolved state, they are surrounded by water molecules in the form of hydration shell. During adsorption on to the ferrite surface, these dye molecules lose hydration shell resulting in increased entropy. The magnitude of increase in entropy in losing hydration shell is more as compared to decrease in entropy due to adsorption onto the ferrite surface, that is why there is overall increase in entropy for this adsorption process.

The negative values of ΔG^o indicated the spontaneity of dye adsorption process. With increase in temperature change in Gibb's free energy further decreases, which revealed that this adsorption process is more favored at higher temperatures.

- Various adsorption isotherm models such as Dubinin-Radushkevich (D-R), Freundlich, Temkin, and Langmuir isotherms were used to fit experimental data for CR dye adsorption. In this study, among different isotherm models, R^2 (correlation coefficient) values demonstrate how well the D-R isotherm model fits the adsorption data for Al-doped Co-Mn ferrite. The D-R model accounts for surface homogeneity and the potential energy of adsorption sites, making it ideal for describing adsorption on Al-doped transition metal ferrites. Aluminium doping in Co-Mn ferrite introduces new active sites at the surface, which modifies the energy landscape of the ferrite's surface, leading to a broader range of interaction energies that the D-R model captures effectively. Whereas Al-doped Ni-Mn, Cu-Mn and Zn-Mn ferrites R^2 values demonstrate that Freundlich isotherm model provides a good fit for the adsorption data. Al-doped transition metal ferrites have heterogeneous surface properties due to their crystalline structure, surface defects, and doping-induced changes. The fit of this model underscores the complexity of adsorption processes, highlighting non-ideal and heterogeneous surface adsorption resulting from variation in adsorption capacity due to different energy sites. The value of empirical constant 'n' in the Freundlich isotherm was larger than unity, which indicates that adsorption process is favorable.
- Adsorption kinetics studies provide insights into the adsorption process and help in determining the mechanisms and rates at which dyes are adsorbed onto a surface. Experimental data is typically analyzed using standard kinetic models to identify the

best fit. In this study, the Lagergren PFO and the PSO models was used to fit the experimental results. The computed data is displayed together with the reliability of each model examined by the correlation coefficient (R^2). For the adsorption of dye pollutants in an aqueous solution, the R^2 values for pseudo-second-order kinetics were higher than those of pseudo-first-order kinetics. The pseudo-second-order model assumes that the adsorption process is primarily chemical-like in nature. This involves strong interactions between the adsorbate (dye molecules) and the adsorbent (Al-doped ferrite) surface. This is highly relevant for Al-doped mixed transition metal ferrite, as their surfaces often have active sites that interact strongly with dye molecules through electrostatic forces.

The present study is also focused on the synthesis of Al-doped mixed transition metal ferrites through solution combustion method. Oxalyldihydrazide was used a fuel for this combustion process. Combustion method has many advantages over other conventional methods. Single phase ferrites can be synthesized at lower temperature and in shorter time. Doping ferrites with aluminium offers several advantages which includes, physical and chemical characteristics of the ferrite structure, increase in ferrite's surface area and porosity. These enhanced factors are critical for effective dye adsorption. These structural changes create more active sites on the material's surface, allowing for better interaction with dye molecules in aqueous solutions. In this study, the maximum adsorption capacity was observed for Al-doped Ni-Mn ferrites as compared to the others, which is attributed to its pore structure, high surface to volume ratio, adsorption behavior, and greater interactions with the dyes.

5.2 Future scope

The adsorption of dyes is a crucial area of research, particularly for wastewater treatment and environmental remediation. The field has significant scope for development in materials, techniques, and applications. The future scope for the adsorption of dyes focuses significantly on enhancing regeneration capabilities and adapting adsorbents for large-scale industrial wastewater treatment (textile, printing, and paper industries). Ongoing research will aim to increase the understanding of multi-component adsorption systems. This includes studying the interactions between different dye molecules and the adsorbents, which can lead to improved strategies for dye removal in industrial wastewater. Future research is expected to focus on developing advanced adsorbents that not only have a high adsorption capacity but also maintain their efficacy after multiple cycles of use. Innovations in regeneration methods can improve the cost-effectiveness and environmental impact of dye-loaded adsorbent recovery. Employing

low-energy and resource-efficient regeneration processes will be critical in making these technologies sustainable and viable for large-scale use. Adapting adsorbents for large-scale industrial applications involves optimizing material properties to handle high dye concentrations and complex wastewater compositions effectively. Developing adsorbents with high surface area, superior mechanical durability, and enhanced selectivity will be essential. Furthermore, integrating adsorption systems into existing industrial processes will be crucial, ensuring compatibility with high-flow conditions and large volumes. This integration must accommodate high-flow conditions and large volumes typical in industrial settings, ensuring that systems are both efficient and practical. Research could also be focused on designing materials for selective adsorption based on molecular recognition and improving the understanding of multi-component systems to enhance the removal of dyes in real-world wastewater.

List of Publications

1. **Ayoub M**., Dosanjh H.S. (**2025**). Investigating the Influence of Aluminum Doping on the Structural, Kinetic, Thermodynamics, and Isothermal Properties of $Al_xZn_{0.7}Mn_{0.3}Fe_{2-x}O_4$ Soft Ferrite for the Removal of Dyes from Wastewater. Topics in Catalysis. https://doi.org/10.1007/s11244-025-02153-5
2. **Ayoub M.,** Dosanjh H.S. (**2025**). Synthesis and characterization of $Al_xCu_{0.7}Mn_{0.3}Fe_{2x}O_4$ ferrite and its application in adsorption of dyes. Journal of Molecular Structure. DOI:10.1016/j.mol.struc. 2024.140015.
3. **Ayoub M.,** Dosanjh H.S. (**2024**). Al-doped Mixed Transition Metal Ferrites Synthesis and Application in Adsorption of Dyes. ChemistrySelect, 9:e202403132. DOI:10.1002/slct.202403132.
4. Beri I., **Ayoub M**., Fatma N., Dosanjh H.S. (**2024**). Mn-Zn spinel ferrite synthesis by solution combustion method and applications in adsorption of dyes. https://doi.org/10.1051/bioconf/20248601004
5. Sharma R., Kumar H., Yadav D., Saini C., Kumari R., Kumar G., Kajjam A. B., Pandit, V., **Ayoub M**., Saloni Deswal Y., Sharma A. K. (**2024**). Synergistic advancements in nanocomposite design: Harnessing the potential of mixed metal oxide/reduced graphene oxide nanocomposites for multifunctional applications. Journal of Energy Storage, 93, 112317. https://doi.org/10.1016/J.EST.2024.112317
6. Malik A.Q., Sena S., Mir T.G., Kumar D., **Wani M.,** Rashid A. (**2024**). Assessment of photocatalytic efficiency and antifungal activity of zinc-doped copper sulfide composite embedded with graphene oxide nanosheets. Journal of Molecular Liquids, 395. DOI:10.1016/J.MOLLIQ.2023.123925.
7. Dr. Manohar Rajendra, Dr. Muhammad Idzdihar Bin Idris, **Mehnaz Ayoub** & P.L.V.N. Saichandra, (**2024**). Futuristic Trends in Chemical Material Sciences & Nano Technology. IIP Series, Volume 3, Book 9.
8. Malik A. Q., Mir T. ul G., Kumar D., Mir I. A., Rashid A., **Ayoub M**., Shukla S. (**2023**). A review on the green synthesis of nanoparticles, their biological applications, and photocatalytic efficiency against environmental toxins. Environmental Science and Pollution Research, 30(27), 69796–69823. https://doi.org/10.1007/S11356-023-27437-9.

9. Qayoom A., Ashraf I., Jan S, Rashid A.**, Ayoub M.,** Kumar D. (**2022**) Synthesis and Characterization of NiS and Zn-doped NiS Quantum Dots and their application in methylene blue degradation in aqueous solution.

List of Conferences/Workshops

1. Recent Advances in Fundamental and Applied Science (**RAFAS 2023**) Organized by school of Chemical Engineering and Physical Sciences, Lovely Faculty of Technology and Sciences, Lovely Professional University Punjab.
2. International Conference on Futuristic Materials in Science and Technology (**ICFMST-2022**) organized by the Department of Chemistry, Bannari Amman Institute of Technology, Sathyamangalam Tamil Nadu.
3. International Association of Advanced Materials, IAAM Sweden. Advanced Materials World Congress **2022** in Stockholm, Sweden.
4. Water Resources Management & Fluvial Hydraulics in Steep Mountain Streams," organized by the Department of Civil Engineering, Dr. B R Ambedkar National Institute of Technology, Jalandhar, Punjab, **2024**.